

The efficient cause of science

Citation for published version (APA):

Bhat, S. (2023). *The efficient cause of science: Computational methods for mapping the visual cortex*. [Doctoral Thesis, Maastricht University]. Maastricht University. <https://doi.org/10.26481/dis.20230502sb>

Document status and date:

Published: 01/01/2023

DOI:

[10.26481/dis.20230502sb](https://doi.org/10.26481/dis.20230502sb)

Document Version:

Publisher's PDF, also known as Version of record

Please check the document version of this publication:

- A submitted manuscript is the version of the article upon submission and before peer-review. There can be important differences between the submitted version and the official published version of record. People interested in the research are advised to contact the author for the final version of the publication, or visit the DOI to the publisher's website.
- The final author version and the galley proof are versions of the publication after peer review.
- The final published version features the final layout of the paper including the volume, issue and page numbers.

[Link to publication](#)

General rights

Copyright and moral rights for the publications made accessible in the public portal are retained by the authors and/or other copyright owners and it is a condition of accessing publications that users recognise and abide by the legal requirements associated with these rights.

- Users may download and print one copy of any publication from the public portal for the purpose of private study or research.
- You may not further distribute the material or use it for any profit-making activity or commercial gain
- You may freely distribute the URL identifying the publication in the public portal.

If the publication is distributed under the terms of Article 25fa of the Dutch Copyright Act, indicated by the "Taverne" license above, please follow below link for the End User Agreement:

www.umlib.nl/taverne-license

Take down policy

If you believe that this document breaches copyright please contact us at:

repository@maastrichtuniversity.nl

providing details and we will investigate your claim.

DOCTORAL THESIS

THE EFFICIENT CAUSE OF SCIENCE:
COMPUTATIONAL METHODS FOR
MAPPING THE VISUAL CORTEX

❧ *Salil Bhat* ❧

2023

© Salil Bhat, Maastricht 2023

This work is licensed under a Creative Commons Attribution 4.0 International License (CC BY 4.0). You are free to share and adapt the material for any purpose, even commercially, under the following terms: Attribution — You must give appropriate credit, provide a link to the license, and indicate if changes were made. You may do so in any reasonable manner, but not in any way that suggests the licensor endorses you or your use. No additional restrictions — You may not apply legal terms or technological measures that legally restrict others from doing anything the license permits. This is a human-readable summary of (and not a substitute for) the license. For the full license text, see: <https://creativecommons.org/licenses/by/4.0/legalcode>

Cover	Alexander Waga , 2023
Formatting	Salil Bhat, 2023[template]
Production	ProefschriftMaken 2023, www.proefschriftmaken.nl
ISBN	978-94-6469-352-2

THE EFFICIENT CAUSE OF SCIENCE:
COMPUTATIONAL METHODS FOR
MAPPING THE VISUAL CORTEX

Dissertation

To obtain the degree of Doctor at Maastricht University,
on the authority of Rector Magnificus, Prof. Dr. Pamela Habibović,
in accordance with the decision of the Board of Deans
to be defended in public
on **Tuesday, 2nd of May 2023 at 13:00 hours** .

by

❧ *Salil Bhat* ❧

PROMOTER:

Prof. Dr. Rainer Goebel

CO-PROMOTOR:

Dr. Mario Senden

ASSESSMENT COMMITTEE:

Prof. Dr. Federico De Martino (Chair)

Prof. Dr. F.W. (Frans) Cornelissen, *UMCG*

Prof. Dr. Serge Dumoulin, *Spinoza Centre for Neuroimaging*

Dr. Judith Peters

Ode aon Mestreech ...

ARISTOTLE'S FOUR CAUSES OF SCIENCE *

*“There are four causes in terms of which a thing or event would be satisfactorily explained – material, efficient, formal and final. Take a statue. It is made of marble (**material cause**); it is made by the sculptor using certain tools (**efficient cause**); it is in the shape of a horse (**formal cause** which guides the sculptor as he chips away at the marble); it is to commemorate the fabulous exploits of Bucephalus, the horse of Alexander the Great (**final cause**). Also to understand why something is what it is, it is necessary to understand it in terms of the four causes.”*

* This example of Aristotle's four causes of science is taken from the book *The natural and the artefactual: The implications of deep science and deep technology for environmental philosophy* (Lee, 1999)

TABLE OF CONTENTS

1. General Introduction	1
1.1. Vision and Wars	2
1.1.1. Localization Wars	2
1.1.2. Russo-Japanese War	4
1.2. Retinotopy in the time of fMRI	7
1.2.1. functional Magnetic Resonance Imaging (fMRI)	7
1.2.2. Retinotopy	7
1.2.3. Population Receptive fields (pRF) mapping	8
1.3. Need for Speed	9
1.4. The 19 th Problem in Systems Neuroscience	10
1.5. The Efficient Cause of Science	12
2. Fast & Furious pRF Mapping for Real-Time Applications	15
2.1. Introduction	17
2.2. Methods	18
2.2.1. Fast Mapping Procedure (f-pRF)	18
2.2.2. Online Gradient Descent (f-pRF _{gd})	21
2.2.3. Fast pRF Parameter Estimation	22
2.2.4. Grid Search (GS-pRF)	22
2.2.5. Data	23
2.2.6. Real-time Processing	25
2.3. Results	25
2.3.1. Fast Mapping Procedure	26
2.3.2. Online Gradient Descent (f-pRF _{gd})	33
2.3.3. Poorly estimated receptive field size	36
2.4. Discussion	42
3. Connective Field Modelling using (algebraic) Dynamic Mode Decomposition with Control	45
3.1. Introduction	47

3.2. Methods	48
3.2.1. Dynamic Mode Decomposition and its variants	48
3.2.2. Connective Field Modelling using aDMDC	51
3.2.3. Simulated Data	52
3.2.4. Empirical Data	53
3.3. Results	53
3.3.1. Simulated Data	53
3.3.2. Empirical Data	59
3.4. Discussion	61
4. An Investigation into Perception and Mental Imagery through DMD	
Lenses	63
4.1. Introduction	65
4.2. Methods	66
4.2.1. Dynamic Mode Decomposition	66
4.2.2. Spatio-Temporal Dynamics	66
4.2.3. Data	67
4.3. Results	67
4.3.1. Connective Fields	67
4.3.2. Spatio-Temporal Dynamics	68
4.4. Discussion	71
5. General Discussion	73
5.1. Synopsis	74
5.2. The Motive	74
5.3. Methods and their Validations	75
5.4. Future Considerations and Recommendations	77
Bibliography	79
A. Appendix to Chapter 2	91
A.1. Hyperparameter sharing between gradient descent and ridge regression	91
A.2. Effect of hyperparameters on mapping procedure	91
A.3. Supplementary Figures and Tables	93
Impact	99
Acknowledgements	101
Curriculum Vitae	103

 1

GENERAL INTRODUCTION

* 1.1. VISION AND WARS

The brain is the only organ that named itself. This is a popular statement that appears here and there, often on the internet, as a riddle, trivia, fun fact, shower thought, or even a scientific statement. Often subjected to philosophical and (less so) scientific discussions, this statement is not entirely true. It was not one brain that named itself. The formation of words and languages is a collective process. The current English word “brain” comes from (ignoring the proto languages) the old English word “brægn”. Over the past, us humans, collectively agreed to name this organ in our own languages. We might have agreed over the name, but we haven’t, and still don’t, fully agree about the functional organization of the brain. Our current understanding of the brain, especially the vision, has been significantly shaped by scientific and non-scientific wars. This section is a summary of historical events that led up to our current understanding of vision as a function of the brain.

1.1.1. Localization Wars

“The quarrel is very acrimonious; indeed the subject of localization of functions in the brain seems to have a peculiar effect on the temper of those who cultivate it experimentally.”

- William James, *The Principles of Psychology*

The Cerebral cortex is the outer layer (sheet) of the largest part of the brain, the cerebrum. For the longest time in human history, the cerebral cortex was considered to be a homogeneous structure and different parts of the cortex were considered largely equivalent. Only a few isolated cases advocated for the different functions of the cerebral cortex (Gross, 1999). One of the earliest signs of the cortex not being uniform and featureless was discovered by a 24-year-old medical student at the University of Parma, named Francesco Gennari (1752–1797). He observed a white line that divides the grey matter and runs parallel to the cortex. He reported this observation in his monograph titled *De Peculiaribus Structura Cerebri* (1782). We now know that this white strip known as *Stria of Gennari*, marks the primary visual cortex in primates. However, Gennari, at the time, didn’t know the significance of his own finding (Glickstein and Rizzolatti, 1984).

Attack on Phrenology

Franz Joseph Gall (1758-1828) is widely considered to be the starting point of cortical (functional) localization (Gross, 1999). While Gennari had no idea of that what he discovered was the primary location of visual processing, Gall had a firm (but wrong) idea

of functional locations of the cortex. He was one of the founders of the field of Phrenology, which today is rendered as a pseudoscience (Webb et al., 2022). He identified 35 psychological traits, or the *faculties* of the brain, and their associated locations based on the size of cranial (skull) bumps. Phrenologists believed that a person's capacity for a given trait could be predicted by the size of the cranial bump that is associated with it (Jones et al., 2018).

Gall's work was met with a lot of political, religious and scientific criticism, with Pierre Flourens (1794–1867) being his strongest scientific critic. Flourens conducted behavioural and lesion studies on animals and observed that lesions in particular (localized) regions of brain resulted in a mixture of cognitive effects (Glickstein, 1988). While he did conclude that the cerebral cortex was the seat of intelligence, sensation and volition, he denied their localizations (Simpson, 2005). However, his lesions were indiscriminate and ignored anatomical boundaries, which rendered his methods largely inadequate and inappropriate (Zola-Morgan, 1995). In his work *Examen de la phrénologie* (1842, English translation by de Lucena Meigs (Flourens, 1846)), holistic statements such as “It has been shown by my late experiments, that we may cut away, either in front, or behind, or above, or on one side, a very considerable slice of the hemisphere of the brain, without destroying the intelligence” can be found.

Gall's ludicrous observations were not entirely a failure and ultimately, he would be proven right but for the wrong reasons (Folzenlogen and Ormond, 2019). He observed that his more verbal friends and colleagues had protruding eyes. He attributed this to their enlarged frontal lobe, which he concluded was the language area (Jerison, 1977). In an interesting turn of events, Paul Broca (1824-1880) did confirm this and, in a sense, vindicated Gall (Gross, 1999). Today, the region associated with speech production, known as Broca's area, was discovered by Gall some years before Broca was born (Jerison, 1977).

The Battle of Vision

Gall's legacy lived on for a while. In fact, one of his followers, Bartolomeo Panizza (1785–1867), was the first person to propose the localization of visual function of the cortex. He noticed that strokes to the occipital lobe caused partial or complete loss of vision. He also tracked degradation of the optic nerve (in dogs) back to the occipital cortex. On top of that, he also noticed that removal of one hemisphere of this region resulted in blindness in the opposite eye (Wickens, 2014). However, his work went largely unnoticed and was only realized after the work of Ferrier, Munk and Schäfer (Gross, 1999).

David Ferrier (1843-1928), strongly believed that the angular gyrus in the Parietal Lobe, was the center of vision. He concluded that after conducting a series of (electrical) stimulations and lesion experiments on monkeys. He was aware of Panizza's work but did not support it. He was unable to produce eye movements upon stimulation of

the occipital region, nor did he observe any significant visual impairment in this region when lesioned (Wickens, 2014).

On the contrary, stimulating the angular gyrus, resulted in eye movements (akin to a visual experience) and lesioning the angular gyrus caused complete blindness (Glickstein, 1985; Wickens, 2014). He conducted his experiment on three monkeys. One of the monkeys, who was very fond of tea, was unable to find the teacup placed straight in its line of sight. It turns out that in two of the monkeys, the lesions disrupted visually-guided action (such as eye movements) and not vision itself. And the third monkey, it just so happens, was already blind (Fishman, 1995b).

Hermann Munk (1839-1912), soon after Ferrier's experiments, justly reported that it was the damage to the occipital lobe, not to the parietal lobe, that caused blindness. Munk also suggested that the angular gyrus was not related to vision, but was merely responsible for tactile eye movements (Fishman, 1995a). However, Munk was not gentle in his opposition. He lambasted Ferrier with ruthless statements. In his work, Munk (1890) described Ferrier's work with words like "worthless", "gratuitous constructions" and "useless". William James, in his iconic psychology textbook (James et al., 1890), writes "Munk's absolute tone about his observations and his theoretical arrogance have led to his ruin as an authority." Ferrier's work received another big blow when Edward Albert Schäfer entered the battle. His studies reported results opposite to Ferrier's claims, thereby supporting Munk's claim that the occipital lobe, not the angular gyrus, was the seat of vision. By the turn of the 19th century, the debate of the visual area was converging towards the occipital lobe (the striate cortex) (Gross, 1999).

1.1.2. Russo-Japanese War

As the localization of the visual area of the brain was being established (in its right place), a stage was setting up for another question, and another war. But this time the war was a violent one and the question was: how is the visual cortex organized? Salomon Henschen (1847–1930) began investigating the topography of the visual cortex. With the empirical data from over 160 blind or hemianopic (from cortical lesions) subjects, he was able to correctly map the upper and lower visual fields to the lower and upper (reversed) banks of the calcarine sulcus. However, he reversed the center-periphery mapping, which could be caused by the large size and dispersions of the lesions (caused by strokes) (Glickstein, 2014).

The need for smaller and more precise lesions was, regrettably, satisfied by Mosin-Nagant Model 91, Russia's rifle of choice during the Russo-Japanese war (1904-1905). This new type of weaponry had a muzzle velocity of 620 m/s and a bullet diameter of 7.6 mm, which allowed for cleaner wounds that would enter and exit the skull without significant damage to the surrounding brain tissue (refer to Figure 1.1). Japanese soldiers who were shot in the back of their heads had some blind spots in their vision, "as

if they were wearing glasses spattered with black paint” (Kean, 2014). In order to assess the amount of pension that would justly fit the amount of damage the soldiers have suffered, Japanese authorities appointed Tatsuji Inouye (1881–1976). He took this opportunity to explore the topographical organization of the visual cortex (Tubbs et al., 2012).

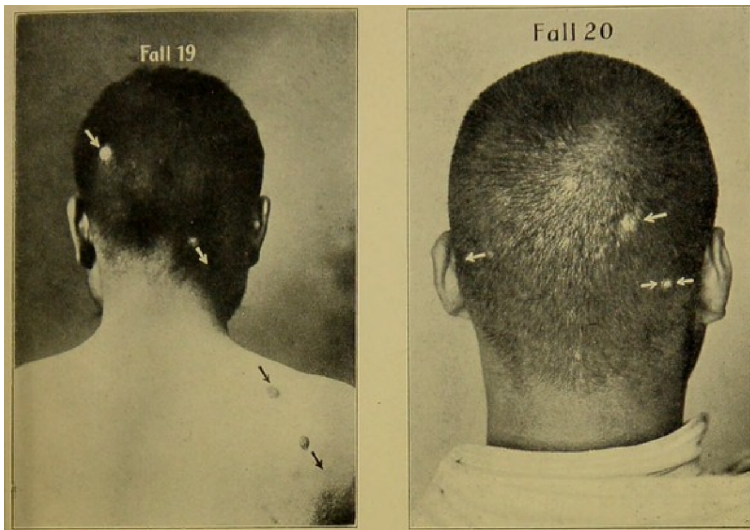


Figure 1.1.: Bullet wounds made by the Mosin rifle making a straight path through the skull and the shoulder. (Inouye, 1909)

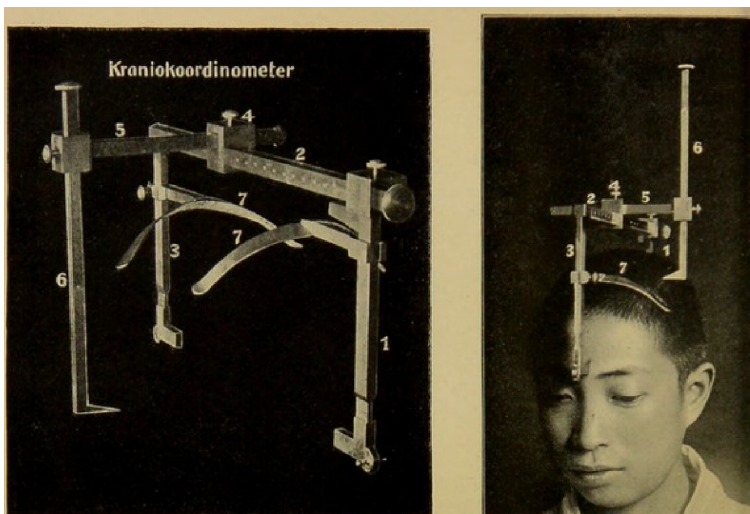


Figure 1.2.: Cranio-coordinometer (Inouye, 1909)

With the intention of precisely mapping the trajectories (straight lines) of these bullets through the brain, Inouye constructed the *cranio-coordinometer* (see Figure 1.2). This way, he was able to measure the extent of the visual cortex using a three-coordinate system. The folded visual cortex was flattened, which made visualizations easy to understand. With 29 subjects, he successfully mapped retinotopic topography on the visual cortex. He also corrected Henschen's mistake by mapping the central visual fields to the caudal part of the visual cortex, and peripheral visual fields to the anterior part. In his mapping, the central visual fields, correctly so, occupied a much larger part than the peripheral fields, thus making it clear that there is an oversampling of central visual fields (Glickstein, 2014; Jokl and Hiyama, 2007).

Later, after World War I, Gordon Holmes (1876-1965) obtained largely the same results as Inouye. Holmes, and not Inouye, has been widely credited for these discoveries. Firstly, because Holmes had the cultural advantage of being British. Secondly, he reported his studies with simpler schematics, which were easier to read, intuitive and appeared in textbooks worldwide (Kean, 2014).

Whether it is Inouye or Holmes, these historic discoveries of retinotopic organization of the visual cortex, sadly, resulted from violent wars. Fortunately, science today has advanced a lot. Researchers today, thanks to techniques like functional Magnetic Resonance Imaging (fMRI), do not need wars to understand the mapping of the human brain. And this would have deeply satisfied Inouye; as he writes in his work (Inouye, 1909; Jokl and Hiyama, 2007):

“The hardship and ferocity of the last war led me to publish these observations. The awfulness and horror of the experience, of which those who did not take part cannot have the slightest appreciation, at the same time raised the hope in me and in all other physicians that in the future, war may, if possible, be prevented. If this is not to be, then it should be carried out with all possible care, reducing as much as possible the terrible sorrow and hardships for its participants. If my work could have even the slightest influence in this direction, then it would fill me with the greatest contentment.”

- Tatsuji Inouye, 1909

❖ 1.2. RETINOTOPY IN THE TIME OF fMRI

“... At some point in his lecture, he said something paraphrased to, “...and this is brand new... we are able to use MRI to see function without any contrast agent! Here’s a movie provided to me by Ken Kwong at our center....” He showed the movie of a series of sequential grainy, low-resolution axial EPI subtraction images of a plane that included visual cortex—depicted at the bottom of the image. When a flashing checkerboard was shown to the subject, the visual cortex “lit up.” Our jaws fully dropped. Tom went on, “and we don’t really know yet what the mechanism is behind this....” My primary reaction to this was “I have a thesis project!””

- Peter A. Bandettini, (*Bandettini, 2015*)[†]

1.2.1. functional Magnetic Resonance Imaging (fMRI)

fMRI has been a breakthrough in neuroimaging. Since the 1990s, it has dominated the field of human brain mapping, largely because of its non-invasiveness, lack of radiation and spatio-temporal resolution. fMRI infers neuronal activity from the changes in blood flow in the brain. An increase in neuronal activity triggers an increase of the blood flow to these neurons. The increased blood supply provides food (glucose and oxygen) to these hungry neurons. The oversupply of oxygenated hemoglobin (diamagnetic) flushes away the de-oxygenated hemoglobin (paramagnetic). This causes an increase in the homogeneity of local magnetic field, thereby increasing the MRI signal (when compared to a non-active state). This contrast signal measured by fMRI is called as the *blood-oxygenation-level-dependent* (BOLD) signal or response (*Goebel, 2007*).

1.2.2. Retinotopy

Retinotopy is the mapping or the projection of the visual field (what we see) from the retina to the visual cortex. If we consider a film camera as an analogy to vision; the retina would be the lens, and the visual cortex would be the photographic film onto which an image (visual field) is being projected. It essentially answers the question of what point in our visual space corresponds to what point on the visual cortex. Since the visual cortex is organized retinotopically, adjacent points in the visual field are represented by the adjacent positions on the visual cortex (*Wandell and Winawer, 2011*).

[†] Part I, Chapter 2 of the book *fMRI: from nuclear spins to brain functions* (*Uludag et al., 2015*)

With the use of fMRI, retinotopy has become an essential aspect of vision research. fMRI made it possible to obtain retinotopic maps non-invasively (Sereno et al., 1995; DeYoe et al., 1996; Engel et al., 1997). The retinotopic maps obtained in the late 90s came from stimulus-referred fMRI responses using sets of ring and wedge stimuli. This approach, pioneered by (Sereno et al., 1995), is often known as the phase-encoding model (Wandell and Winawer, 2011). Figure 1.3 (Dougherty et al., 2003) depicts the retinotopic mapping in polar coordinates. The expanding ring stimulus maps eccentricity (distance from the center of the visual field/cortex) and the rotating wedge stimulus maps the polar angle. Once eccentricity and polar angle are mapped, one can, for each voxel (fMRI volume unit), map its preferred position in the visual field.

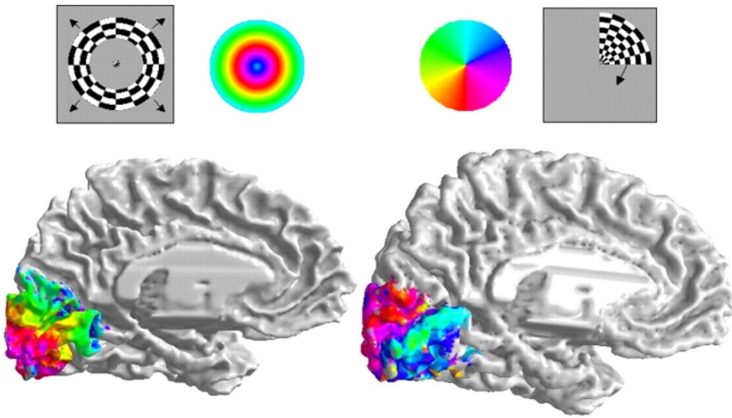


Figure 1.3.: Retinotopic maps of eccentricity and polar angle mapped using expanding ring and rotating wedge stimuli (Dougherty et al., 2003)

1.2.3. Population Receptive fields (pRF) mapping

The term *receptive field* was first coined by Sherrington (1910), who used this term to describe an assemblage of points on the skin that would elicit a reflex movement when a particular stimulus was applied. Hartline (1938), extended this concept to the retina. Hartline described the receptive field of a single nerve optic fiber as the region of the retina that needs to be illuminated in order to elicit a response in that fiber.

A *population receptive field* (pRF), extends the concept of single neuron receptive fields to a population of neurons (Victor et al., 1994). In the modern context of fMRI, a pRF would be the aggregated response of the population of neurons contained within one fMRI voxel (subject to a stimulus). If a stimulus placed (illuminated) in the top-right corner of your visual field, evokes a response in a particular population of neurons, then the pRF of that population is considered to be located at top right corner of the visual field. However, a pRF not only encodes the location of the stimulus, but also, its

size or the coverage. The size of a pRF is harder to quantify than the location because it depends on the shape of the pRF. A natural assumption to the shape of pRFs is a 2D isotropic Gaussian, with the size of pRF being 1 standard deviation of the Gaussian. However, since we do not know the ground-truth about the nature of pRF, their true shape is still being contested (Silson et al., 2018; Merkel et al., 2018; Lerma-Usabiaga et al., 2020b; Bhat et al., 2021)

More recently, the work done by Dumoulin and Wandell (2008), laid the ground for a parametric and expandable pRF computational model. Their approach still serves as the gold-standard approach for pRF mapping. The approach assumes a simple linear model between the stimulus and the acquired fMRI BOLD response. Then for each voxel, an appropriate set of pRF parameters (location and size) are chosen. The pRF parameter was chosen using a grid-search with an aim to minimize the difference between predicted and true BOLD response.

pRF mapping, since then, has become a cornerstone of computational neuroscience and has enabled researchers to understand the relationship between eccentricity and the size of receptive fields along the visual hierarchy (Dumoulin and Wandell, 2008; Amano et al., 2009; Harvey and Dumoulin, 2011; Silva et al., 2018), to investigate neural plasticity and visual development from childhood to adulthood (Dekker et al., 2019; Gomez et al., 2018) and to study the dynamic changes of receptive fields in response to attention (Klein et al., 2014; Kay et al., 2015; Vo et al., 2017; van Es et al., 2018).

pRF modelling has not only enabled researchers to understand fundamental mechanisms and organization of the brain, but also helped them study the pathology of diseases such as Alzheimer’s disease (Brewer and Barton, 2014), schizophrenia (Anderson et al., 2017), albinism (Ahmadi et al., 2019), (artificial) scotoma in patients with macular degradation (Baseler et al., 2011; Barton and Brewer, 2015; Papanikolaou et al., 2015; Linhardt et al., 2022) and in healthy populations (Binda et al., 2013; Haak et al., 2012; Hummer et al., 2018) and even blindness (Georgy et al., 2019).

Furthermore, the ability to estimate receptive field parameters is crucial for several applications. For instance, receptive fields can serve as a target for transcranial magnetic stimulation (Sack et al., 2009) or provide a spatial forward model for computational models (Peters et al., 2012). Additionally, receptive fields can be inverted to provide a decoding model for reconstructing perceived stimuli, as well as imagined, visual stimuli (Thirion et al., 2006; Senden et al., 2019).

✱ 1.3. NEED FOR SPEED

One hindrance to pRF mapping models is that they typically consume a large amount of computational time and resources. A pRF map is normally a pixel-to-voxel map. Given the humongous number of voxels recorded during an fMRI scan, the map itself consumes a lot of memory and at times becomes impossible to work with on regular

laptop/desktop (unless a very selective mask is used). Also, computing with such a large map slows down the whole procedure. The mapping procedures, such as grid-search, which searches over each voxel and parameter, adds to the computational load. This can cause researchers to spend a lot of their valuable time on pRF mapping.

In order to tackle this, we propose a novel, fast and model-free method to map receptive fields based on hashing of the stimulus (Bhat et al., 2021, described in Chapter 2). Our method is capable of reliably mapping the pRFs within seconds, when compared to other methods that take hours for the same number of voxels. At the heart of our methods lies hashing of the stimulus (Sutton and Barto, 2018). Hashing is a technique used in machine learning to reduce the dimensionality of the state space. This is done by computing the overlap between a feature and a hashing function such as a Gaussian or a Radial Basis Function. In our case, the stimulus itself is a sparse space (bar stimulus) and only few pixels are covered by the stimulus. So instead of storing the entire stimulus, we only store the overlap between stimulus and randomly generated 2D Gaussians.

Following the hash-encoding of the stimulus, we perform either ridge regression (for fast mapping) or gradient-descent (for online mapping). In order to estimate pRF parameters, we also propose a fast parameter estimation procedure, that takes advantage of the relationship between a Gaussian’s location and the mean pixel intensity to predict its size. With the fast mapping procedure, the pRFs are immediately available after the retinotopic scanning session. Alternatively, researchers can make use of an online mapping technique to estimate pRFs (and their parameters) in real-time (as the stimulus is being presented). This online mapping combined with reconstruction of perceived and mental imagery (Thirion et al., 2006; Senden et al., 2019) can pave the way for brain computer interfaces (BCIs). Some work has already been done towards such BCIs by Goebel et al. (2022). Such a BCI can be, in future, helpful for locked-in patients.

* 1.4. THE 19TH PROBLEM IN SYSTEMS NEUROSCIENCE

Van Hemmen and Sejnowski (2005), in their book *23 Problems in Systems Neuroscience*, invite 23 experts, to address problems in neuroscience at that time. The 19th problem discussed in the book proposes a new line of research to enrich the traditional way of studying the neuronal properties by supplementing the receptive fields with *projective fields*. Unlike the receptive fields, which receive the sensory stimuli to explain the neuronal activity, projective fields receive neuronal activity from other neurons. Sejnowski (2006) suggests that stimulus-inferred receptive fields explain only a part of the neuronal activity and expresses the need of a unified model that would incorporate the “projective” part of the neuronal activity.

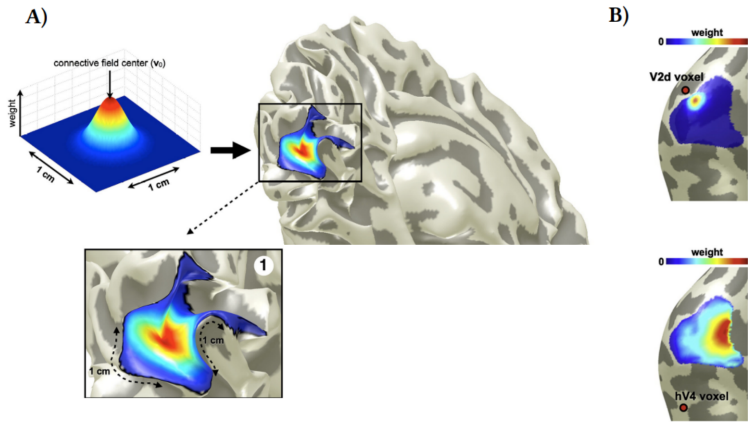


Figure 1.4.: Depiction of Connective Fields (CFs). Panel **A**) shows one such CF modelled as 2D isotropic Gaussian and projected onto the cortical surface. Panel **B**) show two more CFs projected onto a flattened cortical surface with their corresponding target voxels. This figure was adapted from [Haak et al. \(2013\)](#).

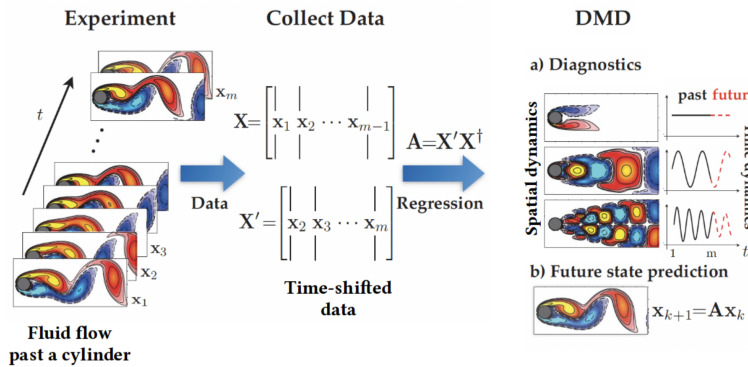


Figure 1.5.: Illustration of DMD on a dynamical system. In this case, the system is the snapshots of fluid flowing past a rigid cylinder. The DMD thus decomposes this system into its spatial and temporal dynamics. Note that the regression step here is shown to construct the full state transition matrix A . However, in actual DMD one would construct a reduced order model of the matrix A . This figure was adapted from [Brunton and Kutz \(2022\)](#)

This problem (often referred to as “Connective Fields” in the literature) has been largely unaddressed so far, with only a few exceptions such as [Heinzle et al. \(2011\)](#); [Haak et al. \(2013\)](#) and [Invernizzi et al. \(2022\)](#). In any case, none of them proposed models unify pRFs and connective fields (CFs). An illustration of CFs, as modelled by [Haak et al. \(2013\)](#) is shown in Figure 1.4. We propose here a novel, efficient and unifying connective field model based on algebraic Dynamic Mode Decomposition with stimulus as a control (aDMDc; [Fonzi et al., 2020](#)) (addressed in Chapter 3 of this work). aDMDc, is variant of regular DMD ([Tu et al., 2014](#)), which incorporates algebraic and differen-

tial terms. We model pRFs as the algebraic term (control) and CFs as the differential term, which unifies both pRF and CF modelling.

Dynamic Mode Decomposition (DMD) is a powerful data-driven tool which has gained a lot of popularity in the field of fluid dynamics. DMD constructs a reduced order model of the system, which makes it a very convenient tool for very large datasets. A typical CF map is a voxel-to-voxel map, which can be a very large matrix (even larger than pRFs). This makes DMD's reduced order model a very suitable candidate for CF modelling. Additionally, this reduced model is sufficient to capture the spatio-temporal dynamics of the system, which can be used to make predictions. Figure 1.5 depicts how DMD decomposes the spatial and temporal dynamics of a fluid-flow system.

As mentioned previously, a CF map is huge, thereby making CF modelling a computationally expensive task. The established models analyze the data one voxel at a time (grid-search is involved in Haak et al. (2013); Invernizzi et al. (2022) and Heinzle et al. (2011)) perform support vector regression per voxel), making CF modelling computationally inefficient. The method proposed in this work constructs a reduced-order model of CFs which is computationally very inexpensive, in terms of memory consumption. Which in turn makes our procedure very fast.

* 1.5. THE EFFICIENT CAUSE OF SCIENCE

In *Physics II 3* and *Metaphysics V 2*, Aristotle lays out four causes which are all “why” questions, that need to be addressed by the “student of nature” in a way that is appropriate to the science of nature (Falcon, 2006). The true understanding of these four causes is often subjected to interpretations and translations. In Aristotelian science, these four causes are indispensable tools for a successful investigation of nature or the world around us (Falcon, 2006). In the simple context of a bronze statue, its construction can be decomposed into four causes as:

- **The Material Cause:** The Material of which it is made, e.g. bronze.
- **The Formal Cause:** The form or a plan for making it, e.g. artisan's blueprints or thoughts.
- **The Efficient Cause:** Things or the forces that make it happen, e.g. artisan's tools.
- **The Final Cause:** The reason for which it is being made, e.g. commemoration of a hero.

In the context of neuroscience of vision, the *material cause* could be, for instance, the data acquired from fMRI. The *formal cause* then be simply a general linear model that

would be used to predict the fMRI time courses. The *efficient cause* would be the tools, techniques and methods to actually solve the linear model. And finally, understanding how vision works (through, for example, pRFs and CFs) would be the *final cause*.

This work is dedicated to the efficient cause of science. That is, to develop computational tools for mapping pRFs and CFs. Note that, the word *efficient* has a slightly different meaning than what Aristotle meant when he refers to the efficient cause. The etymology of the word efficient ([Oxford Dictionary, Online](#)) reveals that, originally it meant ‘accomplishing’ (from Latin *efficere*) and ‘making/causing’ from late Middle English. Which is the same meaning that Aristotle refers to in his work (for example, a tool that makes something happen). In modern sense, just ‘accomplishing’ something might not be good enough and hence, efficient today means doing something in a good way with no waste of time, money or energy. In any case, the tools and methods proposed in this work are efficient in both the modern and Aristotelian sense.

The rest of this work is organized as follows: in **Chapter 2**, we propose a fast, efficient and model-free approach for mapping population receptive fields. We show that our methods are extremely fast, without much loss of performance and can be readily used for real-time applications. In **Chapter 3**, we extend the notion of pRFs to connective field modelling. We propose a unifying approach that efficiently models CFs (and pRFs) on a variety of simulated scenarios. Furthermore, we validate our approach on empirical data by visualizing some exemplary connective fields on the cortical surface and we also show how well our model fits the data by reporting the similarity between estimated and true BOLD signal. In **Chapter 4**, we test out our model on visual tasks to see if there is any fundamental difference between perception and imagery, in terms of CFs and spatio-temporal dynamics. **Chapter 5** or the general discussion, sheds light on topics such as what are some caveats of these models, when to use which model and how our models compare to other existing models and the direction for future research.

 2

FAST & FURIOUS pRF MAPPING
FOR REAL-TIME APPLICATIONS

ABSTRACT

Population receptive field (pRF) mapping is a popular tool in computational neuroimaging that allows for the investigation of receptive field properties, their topography and interrelations in health and disease. Furthermore, the possibility to invert population receptive fields provides a decoding model for constructing stimuli from observed cortical activation patterns. This has been suggested to pave the road towards pRF-based brain-computer interface (BCI) communication systems, which would be able to directly decode internally visualized letters from topographically organized brain activity. A major stumbling block for such an application is, however, that the pRF mapping procedure is computationally heavy and time consuming. To address this, we propose a novel and fast pRF mapping procedure that is suitable for real-time applications. The method is built upon hashed-Gaussian encoding of the stimulus, which tremendously reduces computational resources. After the stimulus is encoded, mapping can be performed using either ridge regression for fast offline analyses or gradient descent for real-time applications. We validate our model-agnostic approach *in silico*, as well as on empirical fMRI data obtained from 3T and 7T MRI scanners. Our approach is capable of estimating receptive fields and their parameters for millions of voxels in mere seconds. This method thus facilitates real-time applications of population receptive field mapping.

“Livin’ off borrowed time, the clock tick faster.”

- Madvillain (MF DOOM), *Accordion*

❖ 2.1. INTRODUCTION

The retinotopic organization of the human visual cortex has intrigued neuroscientists ever since the beginning of the nineteenth century when visual field maps were first discovered in soldiers suffering from occipital wounds (Inouye, 1909; Holmes, 1918). With the advent of functional magnetic resonance imaging (fMRI) in the early 1990s (Kwong et al., 1992; Ogawa et al., 1992), it became possible to map retinotopy non-invasively (Serenó et al., 1995; DeYoe et al., 1996; Engel et al., 1997). Sereno et al. (1995) pioneered a phase encoding procedure that allowed for the systematic investigation of polar angle and eccentricity distributions. More recently, Dumoulin and Wandell (2008) spearheaded the population receptive field (pRF) mapping approach which provided an expandable, parametric, model of receptive fields. This allowed researchers to study additional properties of receptive fields and their topography as well as relationships between receptive field properties.

The pRF approach has, for instance, enabled researchers to understand the relationship between eccentricity and the size of receptive fields along the visual hierarchy (Dumoulin and Wandell, 2008; Amano et al., 2009; Harvey and Dumoulin, 2011; Silva et al., 2018), to investigate neural plasticity and visual development from childhood to adulthood (Dekker et al., 2019; Gomez et al., 2018) and to study the dynamic changes of receptive fields in response to attention (Klein et al., 2014; Kay et al., 2015; Vo et al., 2017; van Es et al., 2018). Furthermore, pRF modelling has aided researchers' investigations of pathology such as Alzheimer's disease (Brewer and Barton, 2014), schizophrenia (Anderson et al., 2017), albinism (Ahmadi et al., 2019), (artificial) scotoma in patients with macular degradation (Baseler et al., 2011; Barton and Brewer, 2015; Papanikolaou et al., 2015) and in healthy populations (Binda et al., 2013; Haak et al., 2012; Hummer et al., 2018) and even blindness (Georgy et al., 2019). Additionally, the ability to estimate receptive field parameters is crucial for a number of applications. For instance, receptive fields can serve as a target for transcranial magnetic stimulation (Sack et al., 2009) or provide a spatial forward model for computational models (Peters et al., 2012). Furthermore, receptive fields can be inverted to provide a decoding model for reconstructing perceived, as well as imagined, visual stimuli (Thirion et al., 2006; Senden et al., 2019).

The latter has been suggested to pave the road towards pRF-based brain-computer interface (BCI) communication systems able to directly decode internally visualized letters from topographically organized brain activity (Senden et al., 2019). This is hindered, however, by the method's immense consumption of computational time and resources. This issue largely remains unaddressed, although some recent work (Thielen et al., 2019) has proposed a fast deep-learning based mapping algorithm (DeepRF). The DeepRF method deploys a deep convolutional neural network (ResNet) which receives a time-series as input and predicts the corresponding pRF parameters. Once the

network is trained, pRF parameters can be estimated simply using a rapid forward pass. This method is indeed faster than standard methods such as grid-search and achieves faithful estimation of pRF parameters with an average computational time of 0.01 to 0.03 seconds per voxel. However, the procedure requires the generated simulated data (for training) and the empirical data to have the same experimental design. Hence, for empirical data with a new experimental design, the network needs to be trained again and the training of the deep neural network can take up to several hours. Moreover, fMRI data typically contains a large number of voxels. The high spatial resolution at field strengths of 3 and 7 Tesla leads to hundreds of thousands or even millions of voxels. Therefore, despite achieving low computational time per voxel, the total computational time for all voxels is on the order of several minutes. This makes the approach unfeasible for real-time analysis. With the aim to enable estimation of receptive fields in real-time, we propose here a novel model-agnostic procedure which can be used offline (using ridge regression) as well as online (using gradient descent).

The method relies on regularized linear regression whose basis set is a hashed-Gaussian encoding of the stimulus-evoked response. Specifically, the stimulus space is exhaustively partitioned as a set of features where each feature uniquely encodes the stimulus by computing the overlap between the stimulus and a set of randomly positioned Gaussians. This type of encoding considerably reduces the memory requirements and thereby accelerates calculations.

Using two previously acquired datasets from 3 Tesla and 7 Tesla MR systems, we show that the proposed approach works extremely fast. It is able to estimate receptive field shapes of millions of voxels within seconds. This allows the selection of visually responsive voxels through cross-validation and subsequent estimation of receptive field parameters within about one minute even if the data consists of more than 4 million voxels.

* 2.2. METHODS

2.2.1. Fast Mapping Procedure (f-pRF)

Tile Coding and Hashing

To reduce computation time as well as to lower memory requirements, we encode the stimulus using tile coding and hashing (Albus, 1975, 1981). Tile coding is a linear function approximation used in reinforcement learning (Sutton and Barto, 2018) to deal with large and continuous state spaces. In tile coding, the state space is exhaustively partitioned into sub-regions called tiles. Usually, the presence of an entity within a tile (in this case, the presence of a stimulus in a region of the visual field) is encoded in a binary fashion. However, it is also possible to encode features using radial basis functions

which have the additional benefit of varying smoothly. Memory requirements can be reduced further by hashing a group of individual, non-contiguous, tiles into a single tile. Figure 2.1 depicts tile-coding and hashing of sample stimuli. The presence of a stimulus is encoded as the extent of overlap between the stimulus and hashed tilings. For our purposes, we use a 2-D isotropic Gaussian as the radial basis function. Subsequently, we hash by combining five randomly selected Gaussians into a single tile leading to a total of 250 tilings. The 5 Gaussian tiles within a tiling may or may not overlap. We normalized each tile to ensure that the volume under its surface is equal to one.

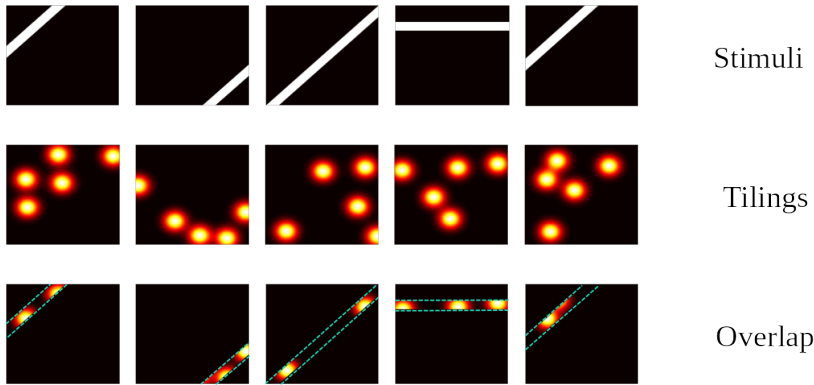


Figure 2.1.: Illustration of tile-coding and hashing. The top row shows sample stimuli. The middle row shows sample tilings, each containing 5 Gaussians which make up one tile. The bottom row shows overlap between stimuli and corresponding tiles.

Encoding Stimuli

Using hashed-Gaussians as tiles, it is possible to encode retinotopic stimuli. First, an overlap between a binary indicator function and a tiling matrix Γ (pixels-by-tiles) is computed. The binary indicator function \mathbf{S} (time-by-pixels) marks the position of the stimulus aperture at each moment in time. Subsequently, the computed overlap is convolved with a canonical two-gamma hemodynamic response function (HRF) function (h) to obtain the encoded stimulus ϕ

$$\phi = S\Gamma * h \quad (2.1)$$

Ridge Regression (f -pRF_{ridge})

We use ridge regression for fast offline pRF mapping (i.e. after all functional volumes have been acquired). Specifically, the blood-oxygen-level dependent (BOLD) response is modeled by

$$B = \phi\theta + \epsilon \quad (2.2)$$

where θ are the estimated weights and ϵ denotes the residuals. Note that, prior to computing θ , both ϕ and the BOLD data B are z -normalized. In order to estimate θ , the discrepancy between the measured and predicted BOLD response ($\phi\theta$) needs to be minimized. Therefore, we define the error or the loss as

$$E = \frac{1}{2} (B - \phi\theta)^T (B - \phi\theta) + \frac{1}{2} \lambda \|\theta\|_2^2 \quad (2.3)$$

In order to avoid over-fitting, we use L_2 regularization and λ denotes the regularization factor. The gradient of the error with respect to θ can be computed as

$$\frac{\partial E}{\partial \theta} = -\phi^T B + \phi^T \phi \theta + \lambda \theta \quad (2.4)$$

By setting $\frac{\partial E}{\partial \theta} \rightarrow 0$ and solving for optimal θ , we get

$$\theta = (\phi^T \phi + \lambda I)^{-1} \phi^T B \quad (2.5)$$

Receptive fields can now be straightforwardly obtained by multiplying the tiling matrix with the estimated θ : $W = \Gamma\theta$. These *raw* receptive fields are then subjected to post-processing as they tend to contain anomalous pixel intensities. These can be removed by first normalizing the raw receptive fields to the range $[0, 1]$ and then shrinking them by raising each entry to a power of some positive integer (shrinkage factor). This shrinks noisy pixel intensities close to 0 while leaving those close to 1 unaffected (figure 2.2), thus yielding cleaner receptive fields.

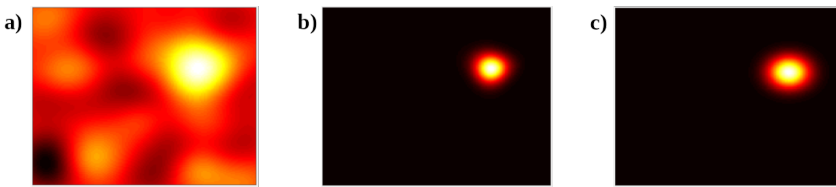


Figure 2.2.: The effect of shrinking a raw receptive field. **a**, Raw receptive field displaying undesirably large pixel intensities. **b**, The receptive field after shrinkage with a factor of 9. **c**, The corresponding ground truth receptive field.

Similarity Metric

In order to compare the receptive fields obtained from ridge regression with corresponding ground-truth/grid-search receptive fields, we use the Jaccard Index (JI; or Jaccard Similarity). The Jaccard Index is bound to $[0, 1]$ (give that the quantities that are

being compared are in the same range), with 1 indicating that receptive fields are identical. Since the Jaccard Index is a conservative metric that is highly sensitive to residual anomalous pixel intensities, we aid interpretation of our results by providing a *Null-model* generated from a re-sampling procedure. Specifically, for each estimated receptive field, we pair it with a random ground-truth/grid-search receptive field and compute the JI. The average over these pairs is the JI of one randomization. We repeat this procedure 1000 times to obtain a Null-distribution of randomized JIs. We refer to the mean of the Null-distribution as the *baseline*.

2.2.2. Online Gradient Descent (f-pRF_{gd})

For online pRF mapping we use gradient descent to iteratively update θ with each acquired volume. In this case, we define the loss function as

$$E = \frac{1}{2} (B - \phi\theta)^T (B - \phi\theta) \quad (2.6)$$

The gradient of the loss function with respect to the parameter θ is

$$\frac{\partial E}{\partial \theta} = -\phi^T B + \phi^T \phi \theta \quad (2.7)$$

At each time point, θ is updated by a factor (learning rate η) of the gradient. Note that, unlike ridge regression, a regularization term is not needed in this case, as gradient descent is effectively regularized by the learning rate (see A.1). Considering the n^{th} time point, the update can be computed as

$$\theta_n = \theta_{n-1} + \eta(\phi^T B - \phi^T \phi \theta_{n-1}) \quad (2.8)$$

Similar to the offline method, prior to tile coding and hashing, the stimulus needs to be convolved with the HRF. Furthermore, both the BOLD signal B and encoded stimulus ϕ need to be z-normalized. However, in an online setting this needs to be performed in real-time. Real-time z-normalization requires real-time estimation of the mean and variance of a signal which can be done using Welford's online algorithm (Welford, 1962). Once the current mean $\bar{x}(t)$ and variance $\sigma^2(t)$ have been estimated, the current z-score can be estimated as

$$z_n = \frac{x_n - \bar{n}_t}{\sigma_n^2} \quad (2.9)$$

Voxel Selection

Since not all measured voxels are visual, and hence may not carry significant information, a voxel selection procedure is desirable. We evaluate voxels in terms of the cross-

validated Pearson correlation coefficient (fitness) between their predicted and measured BOLD responses. To account for temporal autocorrelation in the BOLD response, we use a blocked cross-validation procedure (Roberts et al., 2017). Specifically, the data is split into p windows along the time axis. Ridge regression is performed on window 1 and the estimated θ values are used to predict the BOLD response for the remaining $p - 1$ windows. This is followed by ridge regression on windows 1 and 2 and predicting the BOLD response in the remaining $p - 2$ windows. This procedure continues until ridge regression is performed on windows 1 to $p - 1$ and the BOLD response is predicted for the p^{th} (last) window. The overall fitness for each voxel is then given by the mean of fitness values computed for each split. The data used in this paper has 304 time points. We split the data into 4 windows of equal length and retain voxels whose fitness falls within the top 1 %.

2.2.3. Fast pRF Parameter Estimation

Post-processed receptive fields obtained from our ridge regression and gradient descent methods can be readily used to estimate parameters of an isotropic Gaussian pRF model (i.e. the x-location, y-location and size) using a fast procedure. Since peak pixel intensity of a Gaussian receptive field is at its center, we estimate the x- and y-coordinate of pre-processed model-free receptive fields by finding the location of their peak pixel intensity. To estimate the size of receptive fields, our procedure utilizes the relationship between the standard deviation, eccentricity and the mean pixel intensity in an isotropic Gaussian embedded in a finite image. Specifically, given a Gaussian at a fixed location, mean pixel intensity increases as a function of its standard deviation. Furthermore, in a finite image and assuming a fixed size, mean pixel intensity decreases as the Gaussian is progressively moved toward the edge of an image. Therefore, for a given image size, we generate isotropic Gaussians with 25 different standard deviations, located at 25 eccentricities along an axis of 45° , and compute their mean pixel intensities. This can be utilized to perform a linear regression with mean pixel intensity and eccentricities predicting the receptive field size. We then use the resulting regression weights together with previously estimated locations and mean pixel intensity of our receptive fields to obtain an estimate of their size.

2.2.4. Grid Search (GS-pRF)

In order to compare our approach with a standard grid-search based approach, we use the grid-search described in (Senden et al., 2019). In order to search for pRF location, this approach splits the visual field into 100-by-100 circular grid points whose density decays exponentially with eccentricity. Close to the fovea the grid is thus denser than in the periphery, taking cortical magnification into account. Since there is a well estab-

lished linear relationship between eccentricity and the size of pRF (Freeman and Simoncelli, 2011), the grid-search explores a range of slopes (from 0.1 to 1 in steps of 0.1) of the size-eccentricity relationship rather than pRF sizes directly. This effectively allows for exploration of a greater range of receptive field sizes. The code for this approach (as well as our new method) is part of the Computational Neuroimaging Toolbox (available at https://github.com/cnmaastricht/CNI_toolbox).

2.2.5. Data

Simulated Data

We simulate fMRI data for a V1-like cortical sheet extending 55 mm along and approximately 40 mm orthogonal to the horizontal meridian in both hemispheres. Since such a sheet is akin to a flattened cortical mesh, model units are referred to as vertices rather than voxels. Each vertex in the model is a 0.5 mm isotropic patch whose receptive field center is directly related to its position on the surface in accordance with a complex-logarithmic topographic mapping (Schwartz, 1980; Balasubramanian et al., 2002) with parameter values ($\alpha = 0.7, \alpha = 0.9$; Polimeni et al., 2005). The shape of model receptive fields is given by a 2-dimensional Gaussian.

$$f(\mu_x, \mu_y, \sigma) = \exp - \frac{(x - \mu_x)^2 + (y - \mu_y)^2}{2\sigma^2} \quad (2.10)$$

with (μ_x, μ_y) being the receptive field center and σ its size. Below an eccentricity of $e = 2.38^\circ$ all model vertices have a receptive field size of $\sigma = 0.5^\circ$ whereas they exhibit a linear relationship with eccentricity ($\sigma = 0.21e$) beyond this cutoff (c.f. Freeman and Simoncelli, 2011).

A simulated fMRI signal (sampled at a rate of 0.5 Hz) for each vertex is obtained by first performing element-wise multiplication between the receptive field of a vertex and the effective stimulus presented per time point, summing the result and subsequently convolving the obtained signal with the canonical two-gamma hemodynamic response function. Two sources of distortion are added to the signal. First, a spatial smoothing kernel is applied to simulate the point-spread function of BOLD activity on the surface of the striate cortex (Shmuel et al., 2007). Second, autocorrelated noise generated by an Ornstein-Uhlenbeck process with variance $\sigma_{noise}^2 = 0.5$ is added. The smoothing kernel is independently applied to the clean signal and the noise before the two are combined. We simulate both 3T- and 7T-like signals by adjusting the full-width at half-maximum of the spatial smoothing kernel (3.5 mm and 2 mm for 3T and 7T, respectively; c.f. Shmuel et al., 2007) and the time constant of the Ornstein-Uhlenbeck process (2.25 s and 1 s for 3T and 7T, respectively).

Three Tesla Empirical Data

This dataset, previously described in (Senden et al., 2014), comprises a retinotopy run obtained from three participants (all male, age range = 27-35 years, mean age = 32 years). During this run a bar aperture (1.5° wide) revealing a flickering checkerboard pattern (10 Hz) was presented in four orientations. For each orientation, the bar covered the entire screen in 12 discrete steps (each step lasting 2 s). Within each orientation, the sequence of steps (and hence of the locations) was randomized and each orientation was presented six times. Furthermore, within each presentation four bar stimuli were replaced with mean luminance images for four consecutive steps. These data were acquired on a Siemens 3T Tim Trio scanner equipped with a 32-channel head coil (Siemens, Erlangen, Germany) using a gradient-echo echo-planar imaging sequence (31 transversal slices; TR = 2000 ms; TE = 30 ms; FA = 77° ; FoV = 216 x 216 mm²; 2 mm isotropic resolution; no slice gap; GRAPPA = 2). Preprocessing consisted of slice scan time correction, (rigid body) motion correction, linear trend removal, and temporal high-pass filtering (up to 2 cycles per run).

For visualization purposes, we also include anatomical data for subject 1. Anatomical data were collected with a T1-weighted MPRAGE imaging sequence (192 sagittal slices; TR = 2250 ms; TE = 2.17 ms; FA = 9° ; FvV = 256 x 256 mm²; 1 mm isotropic resolution; GRAPPA = 2). In the anatomical images, the grey/white matter boundary was detected and segmented using the advanced automatic segmentation tools of Brain Voyager 20 which are optimized for high-field MRI data. A region-growing approach analyzed local intensity histograms, corrected topological errors of the segmented grey/white matter border, and finally reconstructed meshes of the cortical surfaces (Kriegeskorte and Goebel, 2001; Goebel et al., 2006). The data is available at <https://doi.org/10.34894/ITWFZP>. The dataset is available at <https://doi.org/doi:10.5061/dryad.mb8h6>.

Seven Tesla Empirical Data

This dataset, previously described in (Senden et al., 2019), comprises retinotopy as well as passive viewing of letter stimuli obtained from six participants (2 female, age range = 21-49 years, mean age = 30.7 years). During the retinotopy run a bar aperture (1.33° wide) revealing a flickering checkerboard pattern (10 Hz) was presented in four orientations. For each orientation, the bar covered the entire screen in 12 discrete steps (each step lasting 3 s). Within each orientation, the sequence of steps (and hence of the locations) was randomized and each orientation was presented six times. During the passive viewing run four letters ('H', 'T', 'S' and 'C') were presented in a 8° by 8° bounding frame for a duration of 6 s and their shape was filled with a flickering checkerboard pattern (10 Hz). These data were acquired on a Siemens Magnetom 7T scanner (Siemens; Erlangen, Germany) equipped with a 32 channel head-coil (Nova Medical Inc.; Wilmington, MA, USA) using high-resolution gradient echo echo-planar imaging sequence

(82 transversal slices; TR = 3000 ms; TE = 26 ms; generalized auto-calibrating partially parallel acquisitions (GRAPPA) factor = 3; multi-band factor = 2; FA = 55°; FoV = 186 x 186 mm²; 0.8 mm isotropic resolution). In addition, this dataset includes five functional volumes acquired with opposed phase encoding directions to correct for EPI distortions that occur at higher field strengths (Andersson et al., 2003). Preprocessing further consisted of (rigid body) motion correction, linear trend removal, and temporal high-pass filtering (up to 3 cycles per run).

For visualization purposes, we also include anatomical data for subject 3. Anatomical data was acquired with a T1-weighted magnetization prepared rapid acquisition gradient echo (Marques et al., 2010) sequence [240 sagittal slices, matrix = 320 x 320 mm, voxel size = 0.7 mm isotropic, first inversion time TI1 = 900 ms, second inversion time TI2 = 2750 ms, echo time (TE) = 2.46 ms repetition time (TR) = 5000 ms, first nominal flip angle = 5°, and second nominal flip angle = 3°. Anatomical images were interpolated to a nominal resolution of 0.8 mm isotropic to match the resolution of functional images. In the anatomical images, the grey/white matter boundary was detected and segmented using the advanced automatic segmentation tools of BrainVoyager 20 which are optimized for high-field MRI data. A region-growing approach analyzed local intensity histograms, corrected topological errors of the segmented grey/white matter border, and finally reconstructed meshes of the cortical surfaces (Kriegeskorte and Goebel, 2001; Goebel et al., 2006). The data is available at <https://doi.org/10.34894/ITWFZP>

2.2.6. Real-time Processing

To mimic a real-time scenario, we limited the preprocessing of functional data to trilinear 3D rigid body motion correction which was applied in a simulated real-time setup using Turbo-BrainVoyager (TBV; v4.0b1, Brain Innovation B.V., Maastricht, The Netherlands). The data was accessed directly from TBV using a network interface providing fast transfer speed suitable for real-time applications. The receiver was implemented in MATLAB™(version 2019a, The Mathworks .inc, Natick, MA, USA) using JAVA based TCP/IP interfaces.

* 2.3. RESULTS

All experiments were performed using MATLAB™(version 2019a, The Mathworks .inc, Natick, MA, USA) running on an HP® Z440 workstation with an Intel® Xeon® Processor (E5-1650 v4, 32GB RAM) and an Ubuntu 20.04 operating system. The set of hyperparameters (learning rate $\eta = 0.1$, shrinkage factor = 6 and $FWHM = 0.15$) remain the same for all experiments, except for reconstruction of perceived letter shapes where a shrinkage factor of 9 was used. This set of hyperparameters was chosen

using Bayesian Optimization performed on a simulated dataset with Jaccard Distance as loss function. All the figures generated using MATLABTM(including the parts of Figures 2.1 and 2.2) were generated using *export_fig* (Altman, 2020). Our methods are available as part of the Computational Neuroimaging Toolbox (https://github.com/ccnmaastricht/CNI_toolbox). Example scripts for using our approach are available at https://github.com/ccnmaastricht/real_time_pRF.

2.3.1. Fast Mapping Procedure

Simulated Data

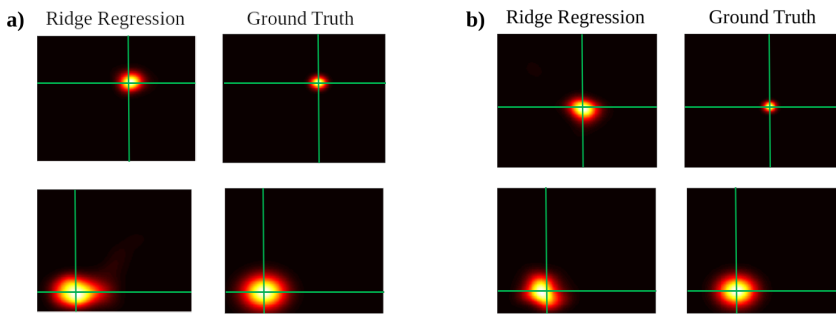


Figure 2.3.: Comparison of ridge-estimated and ground-truth receptive fields. **a)** Small (top) and large (bottom) estimated and ground-truth receptive fields for simulated 3T data ($TR = 2000ms$). **b)** Small (top) and large (bottom) estimated and ground-truth receptive fields for simulated 7T data ($TR = 3000ms$).

The fast, ridge-based, mapping procedure ($f\text{-pRF}_{\text{ridge}}$) was first tested on simulated data to investigate whether it faithfully recovers known population receptive field shapes and their parameters. Overall, the mean Jaccard Similarity (JS) between the estimated and ground-truth receptive field shapes was 0.3452 (95 % CI [0.3409, 0.3495]) and 0.3920 (95 % CI [0.3877, 0.3963]), for simulated 3T and 7T data, respectively. For comparison, corresponding Null-model (Table 2.2) JS values were 0.0418 and 0.0410, respectively. There is thus good correspondence between estimated and ground-truth receptive field shapes which is also apparent from the sample receptive fields shown in figure 2.3. Next, we examined the correspondence between receptive field parameters obtained with the two methods. While receptive fields mapped using the $f\text{-pRF}_{\text{ridge}}$ are not exactly Gaussian, estimated parameters nevertheless show an excellent correspondence with ground truth parameters for both simulated 3T and 7T data (see figures 2.4 and A.3 respectively as well as table 2.1). Please note that despite the high correlation, the receptive field size tends to be slightly overestimated by our method. Figure ?? shows that the size estimations can be improved by using a different shrinkage factor (in

this case, a higher one). The shrinkage factor we obtained from Bayesian optimization maximized fidelity of the receptive field shape rather than pRF parameters. In the case of this dataset, a larger shrinkage would result in better pRF size estimates at the cost of somewhat worse estimates of receptive field shapes. This indicates that there is slight trade-off between these two goals but appropriate choices of the shrinkage parameter allow for faithful estimates of either.

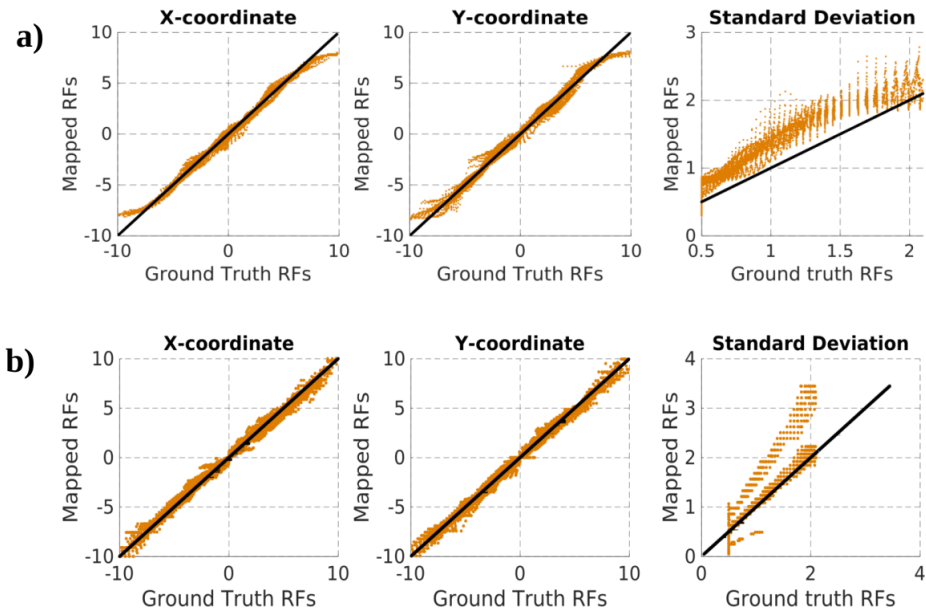


Figure 2.4.: Estimated vs ground-truth pRF parameters for **a)** $f\text{-pRF}_{\text{ridge}}$ and **b)** GS-pRF. A line with a slope of 1 is included as a reference. Voxels whose receptive fields lie outside the field of view were ignored for estimating pRF parameters. Results are from simulated 3T data. Results for simulated 7T data are comparable (see supplementary figure A.3).

	X-coordinate	Y-coordinate	size (σ)
3T	0.9913(95 % CI[0.9909, 0.9916])	0.9871 (95 % CI [0.9865, 0.9876])	0.9674 (95 % CI [0.9660, 9686])
7T	0.9958 (95 % CI [0.9957, 9960])	0.9949 (95 % CI [0.9946, 0.9951])	0.9681(95 % CI[0.9668, 0.9693])

Table 2.1.: Correlations between estimated and ground-truth pRF parameters

Next, we evaluated the $f\text{-pRF}_{\text{ridge}}$ approach in terms of its computational performance. To that end we measured both memory consumption and the computation time required for the mapping procedure itself as well as for subsequent parameter estimation. Computation times were estimated using MATLABTM's stopwatch utility. The execution time measured using this utility can be affected by many unknown variables pertaining to memory, processor, memory caching, MATLABTM's just-in-time compiler, etc. This may influence the execution time measurement each time a

subroutine is executed. Therefore, we report computation times as a mean over 100 runs. Memory requirements were estimated using GNU/Linux’s *pmap* command. The memory requirements reported here are calculated as $mem_{max} - mem_0$, where mem_{max} is the maximum amount of memory consumed during the procedure and mem_0 is the memory occupied by MATLAB™ before starting the procedure (which includes loading of data into memory and other background processes occupying memory). Memory consumption during the procedure was logged every 0.1 seconds using GNU/Linux’s *watch* command. Note that since here we are only interested in computational performance we test the mapping procedure on randomly generated data of the size $304 - by - voxels$. Memory consumption was averaged over 100 repetitions of the procedure. As can be appreciated from figure 2.5 the f-pRF_{ridge} procedure is extremely fast (less than 10 s for more than 3 million voxels) when compared to grid-search (GS-pRF), which may take up to several hours. The computation time only starts to increase as the needed memory exceeds the available memory. As a consequence, virtual memory gets consumed which slows down the mapping procedure. Memory consumption scales linearly with the number of voxels and allows for estimation of ~ 1.75 and ~ 3.5 million voxels on systems with 8GB and 16GB of RAM, respectively.

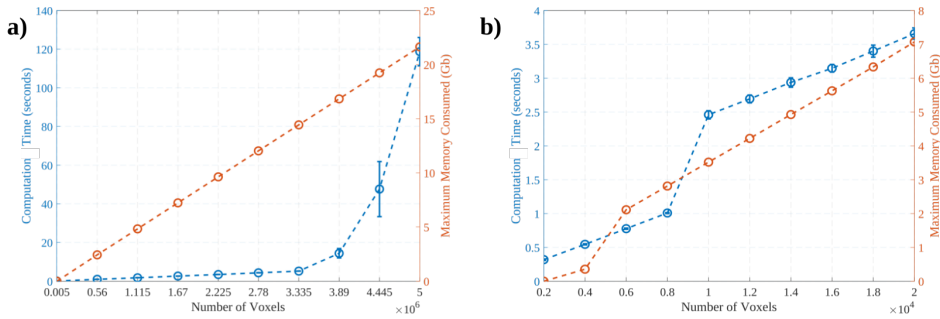


Figure 2.5.: Memory consumption (orange) and computation time (blue), as a function of the number of voxels for **a)** f-pRF_{ridge} and **b)** parameter estimation. Data points corresponding to 0s reflect < 1 Kb.

Empirical Data

Following up on simulation results, we tested the f-pRF_{ridge} procedure on previously acquired empirical data. Similar to the simulated data, we assess our method in terms of its ability to estimate pRF shapes and their parameters as well as computational performance. Since ground truth receptive field shapes and parameters are not known for empirical data, we assess our method on its ability to produce estimates that are consistent with a GS-pRF mapping procedure (as described in section 2.2.4). Sample receptive fields estimated in the 3T and the 7T empirical data are shown in figures 2.7 and 2.6, respectively. Retinotopic surface maps for a representative subject in the 7T and 3T

datasets are shown in Figure 2.9. These results qualitatively indicate a good agreement between receptive field location parameters estimated by our method and the GS-pRF approach. Quantitatively, we observe that the Jaccard similarity between receptive fields estimated using the $f\text{-pRF}_{\text{ridge}}$ and GS-pRF methods consistently exceed those expected based on the Null model. The JS is particularly high (with respect to the baseline) for subjects 3, 5 and 6 for the 7T empirical dataset. This is also apparent from scatter plots showing the correspondence between pRF parameters obtained from our method and GS-pRF in representative subjects (see 2.8a and 2.8b for the 3T and 7T dataset, respectively). In order to compare our approach with the GS-pRF in terms of predictability, we report mean, cross-validated, correlation coefficients (over top 1% voxels obtained using crossvalidation), between the predicted and the acquired BOLD signals, in table 2.3. We also report the mean correlation coefficients over top 1% voxels obtained from GS-pRF (not crossvalidated) in table A.1. It is clear from both the tables 2.3 and A.1 that our method yields better correlation coefficients across subjects and datasets. It is to be noted that there exists a disagreement between the top 1% voxels selected using $f\text{-pRF}_{\text{ridge}}$ and GS-pRF. We report the percentage overlap between the top 1% voxels obtained from $f\text{-pRF}_{\text{ridge}}$ and the ones obtained from GS-pRF in table A.2. The percentage overlap is in general high for the majority of the subjects. The most overlap we observed was 80.49% (subject 3, 7T data) and the least we observed was of 44.12% (subject 1, 7T data).

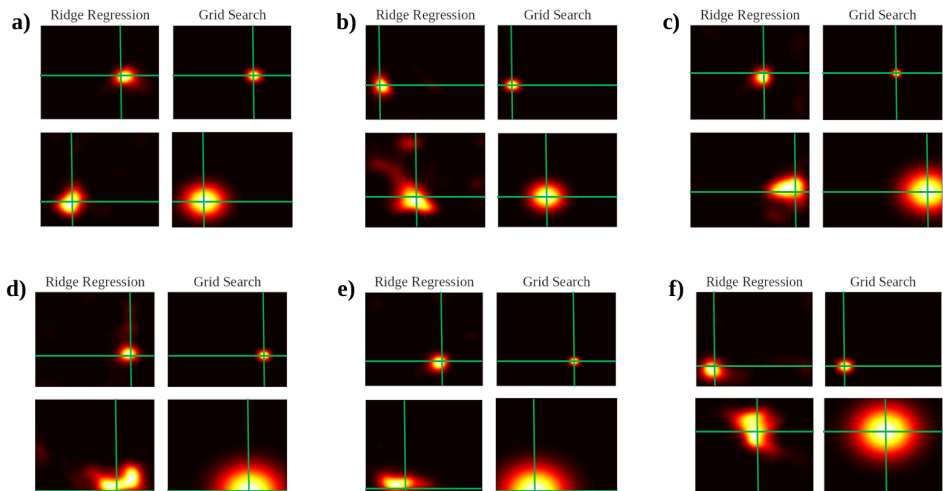


Figure 2.6.: Comparison of $f\text{-pRF}_{\text{ridge}}$ and ground-truth receptive field parameters for 7T data. **a)** Small (top) and large (bottom) estimated and GS-pRF receptive fields for subject 1. **b-f)** Same as panel **a** for subjects 2 to 6, respectively. The axes are centered at pRF location estimated using GS-pRF. The axes are centered at pRF location estimated using GS-pRF

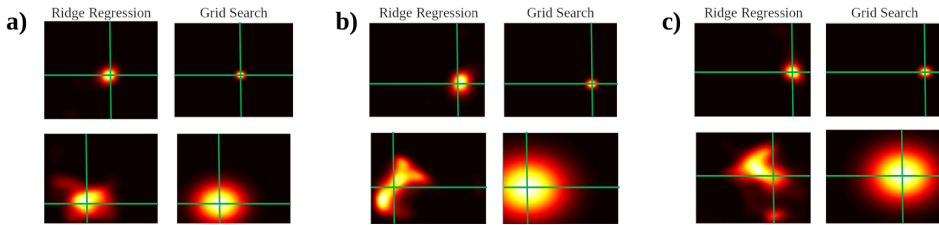


Figure 2.7.: Comparison of f -pRF_{ridge} and GS-pRF receptive field parameters for 3T data. **a)** Small (top) and large (bottom) estimated and ground-truth receptive fields for subject 1. **b,c)** Same as panel **a** for subjects 2 and 3, respectively

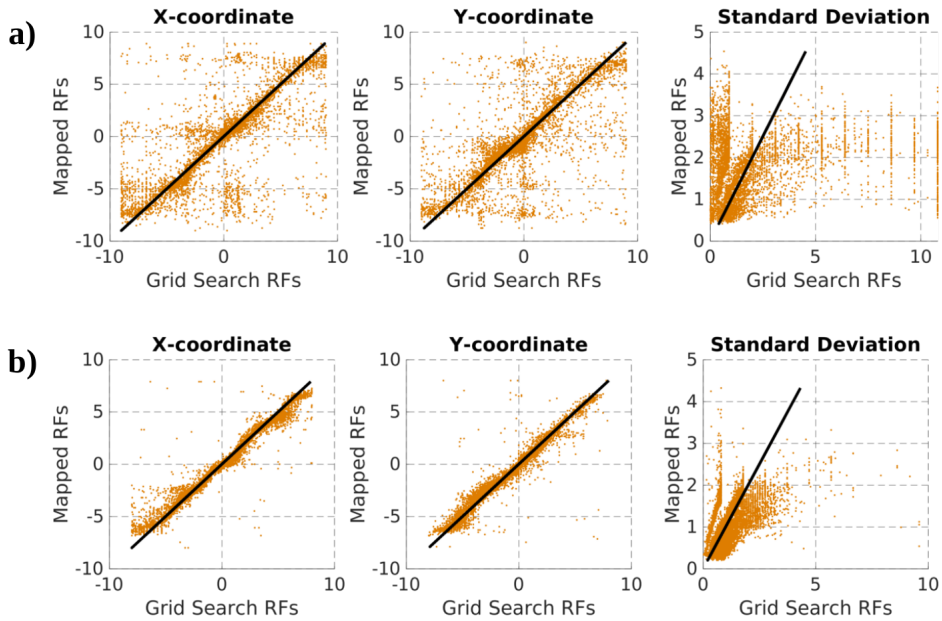


Figure 2.8.: Fast procedure vs GS-pRF estimated pRF parameters for **a)** 3T (subject 1) and **b)** 7T (subject 3) data, respectively. A line with a slope of 1 is included as a reference.

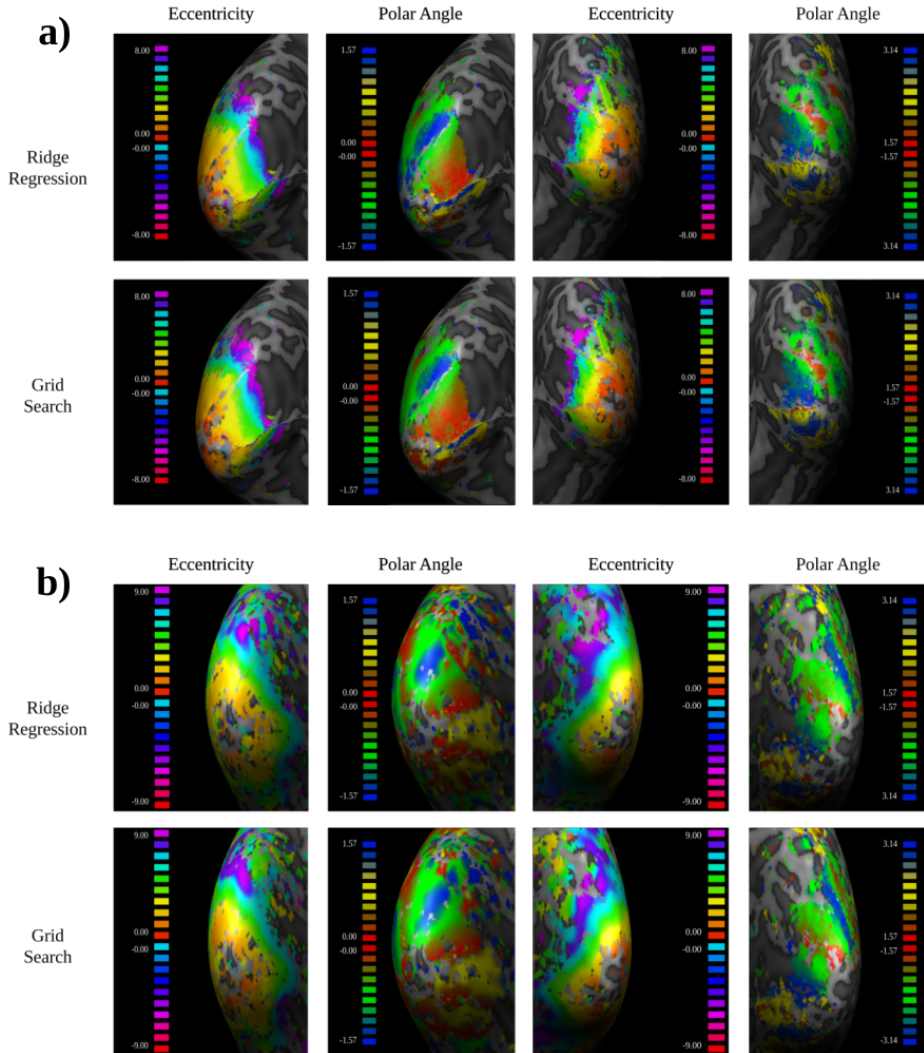


Figure 2.9.: Exemplary eccentricity and polar angle maps in both hemispheres of **a)** S03 from 7T data and **b)** S01 from 3T data. The upper row shows maps obtained using our fast parameter estimation procedure whereas the bottom row shows maps obtained using the GS-pRF procedure. In accordance with the correlation results between maps (see table ??), the two polar angle and eccentricity maps are visually highly similar. Surface maps for S05 from 7T data are shown in A.6

			Jaccard Similarity		baseline
			S01	0.1939 (95 % CI [0.1903,0.1976])	0.0605
			S02	0.3088 (95 % CI [0.3044,0.3132])	0.0673
			S03	0.4998 (95 % CI [0.4961,0.5035])	0.0701
			S04	0.3333 (95 % CI [0.3295,0.3371])	0.0707
			S05	0.4527 (95 % CI [0.4489,0.4565])	0.0786
			S06	0.4564 (95 % CI [0.4532,0.4595])	0.0808

			Jaccard Similarity	baseline
S01	0.2781 (95 % CI [0.2721,0.2840])		0.0781	
S02	0.2607 (95 % CI [0.2554,0.2661])		0.0957	
S03	0.3050 (95 % CI [0.2993,0.3107])		0.0905	

(a)
(b)

Table 2.2.: Mean Jaccard Similarities between receptive fields estimated with the fast procedure and those obtained from GS-pRF for **a)** 3T and **b)** 7T empirical data.

	f-pRF _{ridge}	GS-pRF
S01	0.4424 (95 % CI [0.4396,0.4452])	0.3800 (95 % CI [0.3753,0.3846])
S02	0.4413 (95 % CI [0.4386,0.4441])	0.3750 (95 % CI [0.3706,0.3794])
S03	0.4494 (95 % CI [0.4460,0.4528])	0.3850 (95 % CI [0.3797,0.3903])

(a)

	f-pRF _{ridge}	GS-pRF
S01	0.4237 (95 % CI [0.4227,0.4246])	0.2369 (95 % CI [0.2348,0.2390])
S02	0.3855 (95 % CI [0.3847,0.3864])	0.1772 (95 % CI [0.1745,0.1799])
S03	0.5501 (95 % CI [0.5484,0.5519])	0.5312 (95 % CI [0.5280,0.5345])
S04	0.4115 (95 % CI [0.4103,0.4127])	0.2962 (95 % CI [0.2940,0.2985])
S05	0.4797 (95 % CI [0.4782,0.4812])	0.4277 (95 % CI [0.4246,0.4307])
S06	0.4928 (95 % CI [0.4913,0.4943])	0.4206 (95 % CI [0.4178,0.4234])

(b)

Table 2.3.: Mean correlation coefficients between predicted and acquired BOLD signal obtained from **a)** 3T and **b)** 7T empirical data using top 1% cross-validated voxels.

We again evaluate computational performance in terms of computation times and memory consumption. We estimate both based on 100 runs for each dataset. Since each subject has a different number of voxels, for each run a subject was chosen randomly. The computation time is computed separately for f-pRF_{ridge}, cross-validation and parameter estimation. The mean computation times or execution times for both datasets are reported in tables 2.4a and 2.4b. The computation times suggest that our algorithm is extremely fast in mapping receptive fields. The actual mapping procedure happens within a second for the 3T dataset and in a few seconds for the 7T dataset. Cross-validation, which selects the best voxels, finishes in a couple of seconds for the 3T dataset and takes less than a minute for the 7T dataset. The estimation of pRF pa-

rameters (for all voxels) also takes only a few seconds for both datasets. This means that receptive fields and their pRF parameters are readily available for further analysis.

	Mean	Average data size per subject
f-pRF _{ridge}	0.2055 (95 % CI [0.2010,0.2100])	199,931 Voxels x 304 Volumes
Cross-validation	1.3495 (95 % CI [1.3162,1.3828])	
Parameter estimation	4.2546 (95 % CI [4.2474,4.2618])	
(a)		
	Mean	Average data size per subject
f-pRF _{ridge}	7.0519 (95 % CI [6.1177,7.9861])	4,200,164 Voxels X 304 Volumes
Cross-validation	51.4157 (95 % CI [46.7570 ,56.0744])	
Parameter estimation	7.4357 (95 % CI [7.2950 ,7.5764])	
(b)		

Table 2.4.: Mean computation times in seconds for **a)** 3T and **b)** 7T empirical data. The average data size per subject reflects the amount of data processed by the algorithm at a time.

2.3.2. Online Gradient Descent (f-pRF_{gd})

To demonstrate the capability of f-pRF_{gd} to work in a real-time setting, we mimicked a real-time scenario using TurboBrainVoyagerTM (as described in section 2.2.6). We show in A.1 that f-pRF_{ridge} and f-pRF_{gd} yield similar receptive fields through hyperparameter sharing. Therefore, we do not provide an evaluation of the ability of the method to reliably estimate receptive field shapes and parameters. Instead, we evaluate its performance in terms of whether estimated receptive fields are suitable for projecting cortical activity back into the visual field. For that purpose we utilize data acquired as subjects passively viewed letter shapes previously described in (Senden et al., 2019). The reconstructions obtained from our approach (see figure 2.10) are recognizable and comparable to those obtained from receptive fields resulting from GS-pRF.

In order to assess the convergence of our algorithm, we keep track of how gradients (Figure 2.11a) and Jaccard Similarity (Figure 2.11b) change over time. The analysis was performed using simulated data. It can be seen from Figure 2.11a that the relative change in weights converge very early during stimulus presentation and the Jaccard Similarity converges gradually over the time. There are some occasional peaks in the gradient change which are the result of an occasional overshooting. Our method facilitates tracking of gradients in real-time. Researchers can possibly use this to track changes in gradients or (hashed)weights in real-time and decide when to stop presenting the stimulus. Furthermore, the gradient-descent method can be used in conjunction with simulations to optimize experimental design.

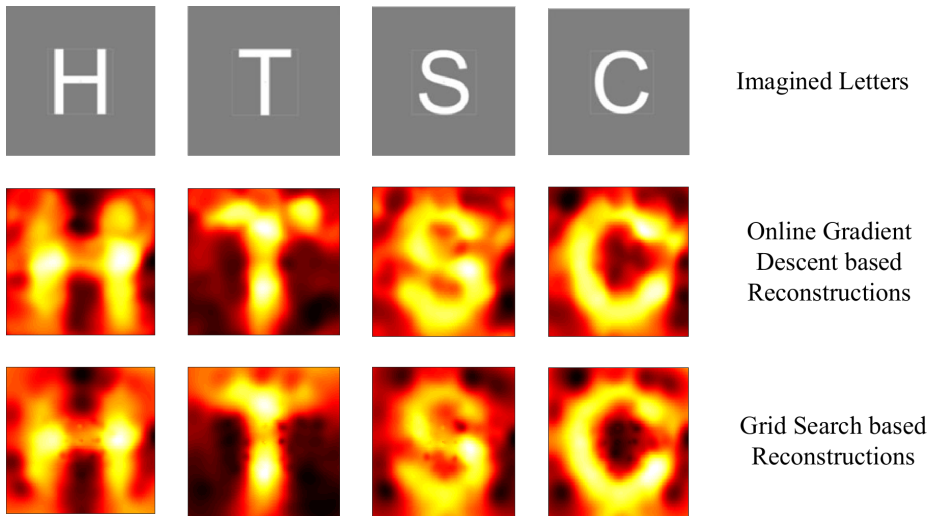


Figure 2.10.: Reconstructions of perceived letter shapes.

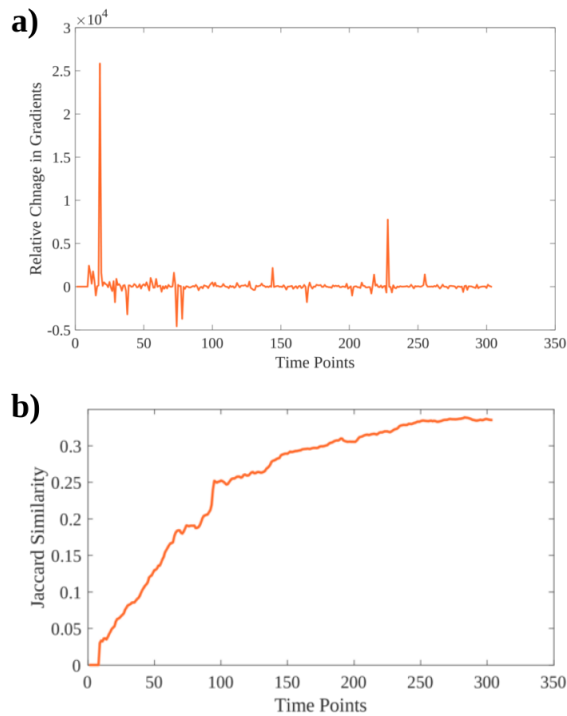


Figure 2.11.: Change in **a)** the gradient (relative to weights) and **b)** Jaccard Similarity over time. The Jaccard Similarity was computed between estimated and ground-truth receptive fields. The plot was generated using simulated 3T data.

The mean computation times per volume acquisition per subject for the 3T and 7T datasets are reported in tables 2.5a and 2.5b, respectively. MATLABTM uses a just-in-time compiler, which has to be executed the first time and has to first load the sub-routine into memory and compile. This often causes the first iteration to be slower. Therefore, we exclude the execution time of the first acquired volume while computing the mean and standard deviation and report it separately. The average computation time per acquired volume is less than the repetition time (2000ms for 3T and 3000ms for 7T), which means that the receptive fields are updated before the next volume is acquired. This is especially useful in a real-time setting where the mapping occurs while the data is being acquired. Figure 2.12 depicts how memory requirements scale with computation time. The computation time only starts to increase when the required memory exceeds the available memory. Generally, up to 1 million voxels can be comfortably estimated within less than 1500ms and requiring less than 2GB of RAM.

	Mean	First Iteration	Number of Voxels
S01	0.1439 (95 % CI [0.1425, 0.1453])	0.2648	229,125
S02	0.1172 (95 % CI [0.1159, 0.1185])	0.2007	177,684
S03	0.1249 (95 % CI [0.1235, 0.1263])	0.2181	192,984

(a)

	Mean	First Iteration	Number of Voxels
S01	2.3974 (95 % CI [2.3651, 2.4297])	5.1320	4,553,058
S02	2.0619 (95 % CI [2.0568, 2.0670])	4.2419	3,957,690
S03	2.4027 (95 % CI [2.3973, 2.4081])	4.9889	4,564,020
S04	2.0082 (95 % CI [1.9809, 2.0355])	3.9555	3,830,696
S05	2.1258 (95 % CI [2.1150, 2.1366])	4.5136	4,023,250
S06	2.2441 (95 % CI [2.2392, 2.2490])	4.7994	4,272,268

(b)

Table 2.5.: Mean computation time (in seconds) per volume per subject for the real-time mapping technique performed on **a)** 3T and **b)** 7T empirical data. For each subject, data for 304 volumes was recorded. Since the first iteration (corresponding to the first volume) is usually abnormally high, it is not included for computing mean and standard deviation.

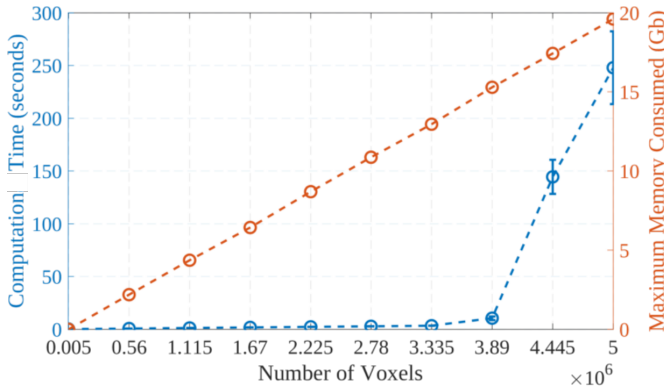


Figure 2.12.: Memory and computation time requirements for the real-time pRF as a function of the number of voxels. Data points corresponding to 0s reflect < 1 Kb of memory consumed and < 0.01 seconds required for execution, respectively.

2.3.3. Poorly estimated receptive field size

At larger eccentricities our approach shows poor correspondence with the GS-pRF algorithm in terms of receptive field size. This is surprising given the good correspondence between estimated and ground-truth receptive field sizes for simulated data. One potential reason for the discrepancy between our (model-free) and the GS-pRF approach is that the latter assumes receptive fields to have a circular shape. If receptive fields are not circular, a GS-pRF method may estimate receptive field sizes inaccurately. Elongation of receptive fields have been observed in several studies (Greene et al., 2014; Silson et al., 2018; Lee et al., 2013; Merkel et al., 2018) rendering this a viable explanation for the discrepancy. An alternative explanation, assuming receptive fields are generally circular, is that the model-based GS-pRF procedure can accurately capture sizes of receptive fields located beyond the visual field of view (the region of the visual field covered by the stimulus) whereas our model-free procedure cannot. Indeed, our model-free procedure would produce a smaller, elongated, receptive field located within the field of view if a large receptive field is located outside the field of view. Below we explore both possibilities.

Anisotropic Model

We investigate the ability of our approach to capture elongated receptive fields by generating simulated data (similar to 2.2.5) using anisotropic Gaussians as ground-truth receptive fields:

$$f(x, y) = \exp\left(-\left(\frac{(x - x_0)^2}{2\sigma_x^2} + \frac{(y - y_0)^2}{2\sigma_y^2}\right)\right) \quad (2.11)$$

We vary σ_y as a ratio of σ_x such that the ratio between σ_x and σ_y increases with eccentricity. We first obtain σ_x as described in section 2.2.5. We then compute $\sigma_y = \rho\sigma_x$; where ρ is σ_x rescaled in the range $[0.5, 3]$. We generate simulated 3T and 7T data with this anisotropic model with the remaining simulation parameters remaining the same as described in section 2.2.5. We define standard deviation σ of such anisotropic receptive fields as the geometric mean of σ_x and σ_y , that is, $\sigma = \sqrt{\sigma_x\sigma_y}$. Using the geometric mean ensures that the area of an ellipse with semi-minor axis σ_x and semi-major axis σ_y is the same as a circle with radius of σ .

To examine whether our approach reliably captures the shape of the receptive fields, we visually inspect them. Figures 2.13 and 2.14 show that our approach is able to generally capture anisotropic receptive field shapes and sizes rather well. The corresponding correlation coefficients are reported in Table 2.6. However, as receptive fields become more elongated, our method tends to slightly underestimate their size. Interestingly, the GS-pRF method assuming isotropic receptive fields tends to somewhat overestimate receptive field sizes at large eccentricities. In conjunction, these effects can account for the discrepancy between the f-pRF_{ridge} and GS-pRF pRF mapping procedure. In order to analyze our approach quantitatively, we compute the JS between estimated receptive fields, ground truth receptive fields and the receptive fields obtained from GS-pRF (see Table ??). Note that the GS-pRF method yields pure Gaussians containing no anomalous activations whereas our method yields anomalous activations surrounding the receptive field. Even slight anomalies get penalized in the JS thus accounting for overall better fit observed for the GS-pRF method.

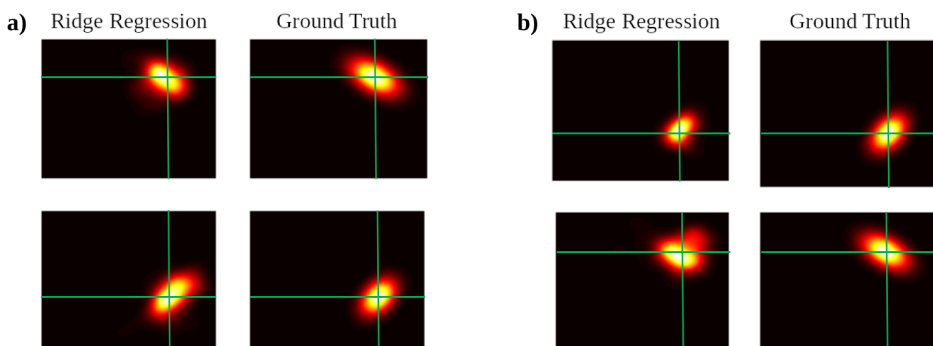


Figure 2.13.: Comparison of f-pRF_{ridge} estimated and anisotropic ground-truth receptive fields. **a)** Small (top) and large (bottom) estimated and ground-truth receptive fields for simulated 3T data. **b)** Small (top) and large (bottom) estimated and ground-truth receptive fields for simulated 7T data. The axes are centered at pRF location estimated using GS-pRF.

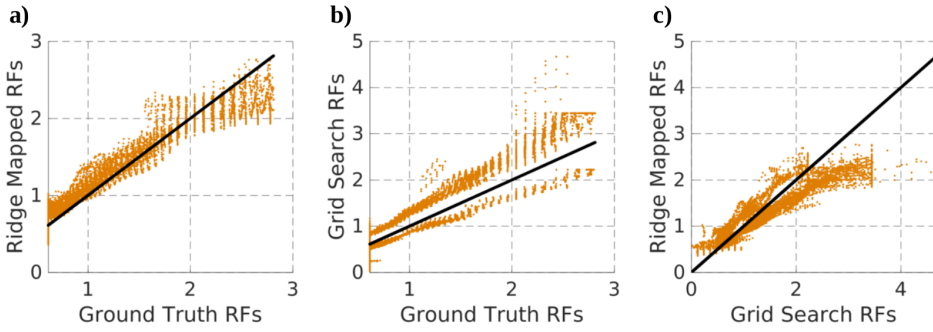


Figure 2.14.: Comparison of receptive field size estimates and ground truth. **a)** Sizes estimated using our fast procedure vs ground truth sizes. **b)** Sizes estimated using GS-pRF vs ground truth sizes. **c)** Sizes estimated using our fast procedure vs GS-pRF estimates. All results are based on simulated anisotropic 3T. Results for simulated 7T data are shown in A.5

	X-coordinate	Y-coordinate	Standard Deviation
f-pRF _{ridge} vs. ground truth	0.9900 (95 % CI [0.9895, 0.9903])	0.9886 (95 % CI [0.9881, 0.9890])	0.9588 (95 % CI [0.9571, 0.9604])
GS-pRF vs. ground truth	0.9950 (95 % CI [0.9948, 0.9952])	0.9962 (95 % CI [0.9960, 0.9963])	0.9163 (95 % CI [0.9130, 0.9195])
f-pRF _{ridge} vs. GS-pRF	0.9909 (95 % CI [0.9905, 0.9913])	0.9891 (95 % CI [0.9887, 0.9896])	0.9122 (95 % CI [0.9088, 0.9156])

(a)

	X-coordinate	Y-coordinate	Standard Deviation
f-pRF _{ridge} vs. ground truth	0.9915 (95 % CI [0.9912, 0.9919])	0.9940 (95 % CI [0.9938, 0.9942])	0.9615 (95 % CI [0.9599, 0.9630])
GS-pRF vs. ground truth	0.9971 (95 % CI [0.9970, 0.9972])	0.9972 (95 % CI [0.9971, 0.9973])	0.9215 (95 % CI [0.9184, 0.9245])
f-pRF _{ridge} vs. GS-pRF	0.9923 (95 % CI [0.9920, 0.9926])	0.9927 (95 % CI [0.9924, 0.9930])	0.9115 (95 % CI [0.9081, 0.9149])

(b)

Table 2.6.: Correlation coefficients between fast and GS-pRF estimated pRF parameters for simulated **a)** 3T and **b)** 7T data based on anisotropic ground-truth receptive fields.

Receptive Fields Beyond the Field of View

Next, we examine to what extent our approach fails to effectively map the receptive fields that (partially) lie beyond the field of view. We generate simulated data with 1000 isotropic receptive fields. All receptive fields are centered at an eccentricity of $5\sqrt{2}$. This would mean, in the case of visual field of maximum radius of 5, the receptive fields are all centered at the top right corner (edge of the stimulus space). Figure 2.15 depicts how the estimated pRF size parameter is affected by an increase in the measured visual field. For comparison, we estimate the receptive field size parameter from receptive field shapes obtained with f-pRF_{ridge} using three different methods **a)** our fast parameter estimation procedure **b)** Levenberg-Marquadt (Levenberg, 1944) with pRF location parameters estimated using our fast procedure and **c)** an exhaustive search for pRF parameters for an initial guess followed by maximum likelihood estimation (Mineault, 2021). Lastly, we use our grid search method without the slope (eccentricity vs size) assumption; i.e., exploring a fixed set of pRF sizes (we term this *vanilla* grid-search). It is clear from

Figure 2.15 that it is a limitation of our approach (f -pRF_{ridge}) that receptive fields whose center is at the border or even exceeds the visual field of view are poorly mapped. It can also be seen from the figure that estimations get better as the field of view becomes larger. Hence, in order to faithfully estimate receptive fields that are centered at high eccentricities, we recommend designing the experiment with a larger field of view.

Subsequently, we also investigated if there exists a trade off between the size of the field of view and the reliability of estimation of the receptive fields. For this purpose, we generate simulated data with 1000 isotropic receptive fields that lie at the center of field of view (eccentricity of 0). We choose eccentricity of 0 to eliminate the possibility of having border effects as described previously. The methods for estimation of pRF size parameter are the same as mentioned previously. It can be seen from Figure 2.16, that initially (left most figures) the size estimations are poor for large receptive fields since they are extremely large for a relatively small field of view. As the field of view increases, the estimations get better. However, after a certain point, relatively small receptive fields get estimated poorly. This is because, in the case of relatively large field of view, the bar aperture needs to be wider to cover the field of view with the same number of steps. As a consequence, the stimulus becomes too coarse to reliably estimate smaller receptive fields. In order to account for smaller receptive fields while also measuring a large field of view, a narrow bar would need to traverse the field of view with a larger number of steps. However, this would require longer runs. Our method thus demands a trade-off between field-of-view, stimulus-size and run-length. In cases where fast estimation of pRF parameters is not essential, we thus recommend to use a grid-search method since it is less affected these effects.

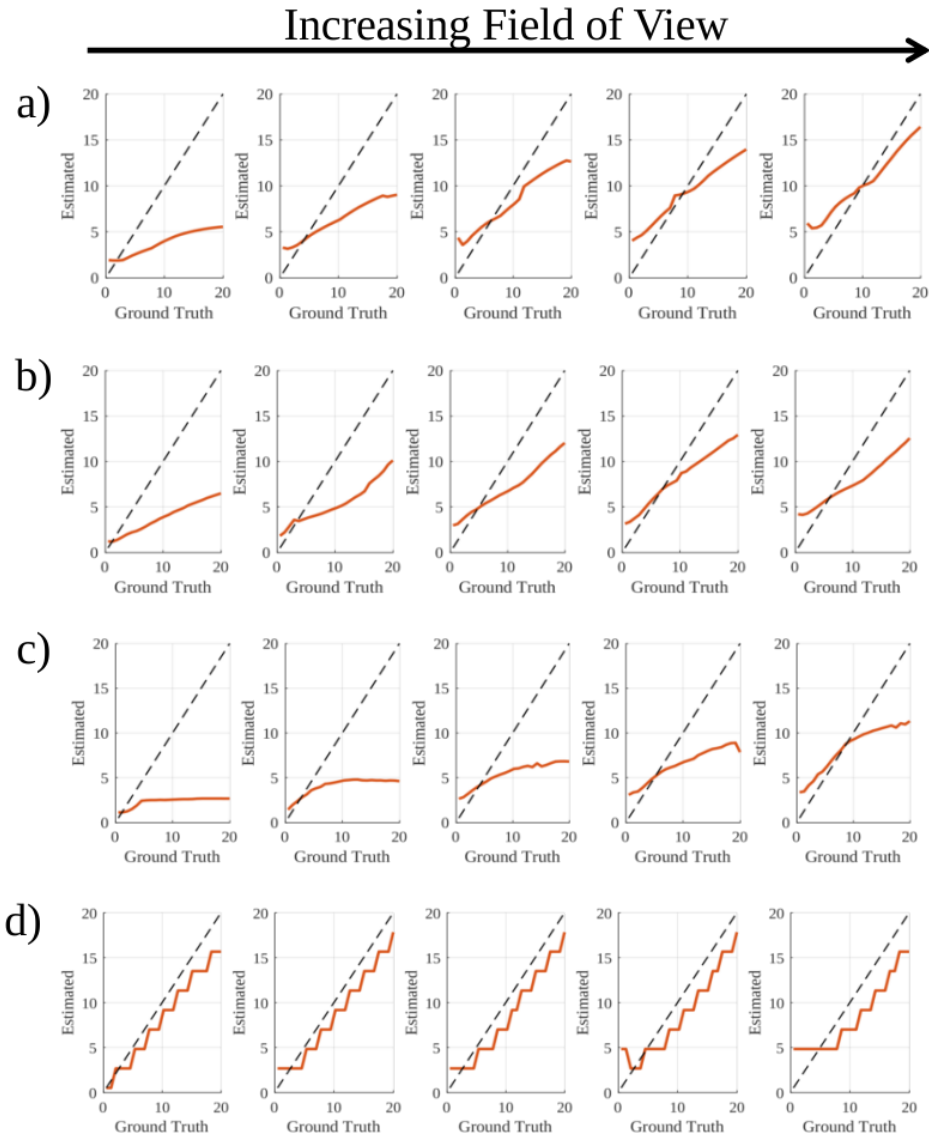


Figure 2.15.: Change in the estimation of the pRF size parameter with respect to change in field of view. All the receptive fields are centered at an eccentricity of $5\sqrt{2}$. The maximum radius increases (left to right) in the range $[5, 8, 12, 15, 19]$. The receptive fields sizes (1 standard deviation) are in the range $[0.5, 20]$. The plots are generated using **a)** f -pRF_{ridge} **b)** Levenberg-Marquadt with pRF location parameters estimated using f -pRF_{ridge} and **c)** an exhaustive search for pRF parameters for initial guess followed by maximum likelihood estimation. **d)** vanilla grid search. Note that the discrete steps in the grid search result from the resolution of the grid. As more parameter values are explored, this curve would become increasingly smooth but estimation would take more time

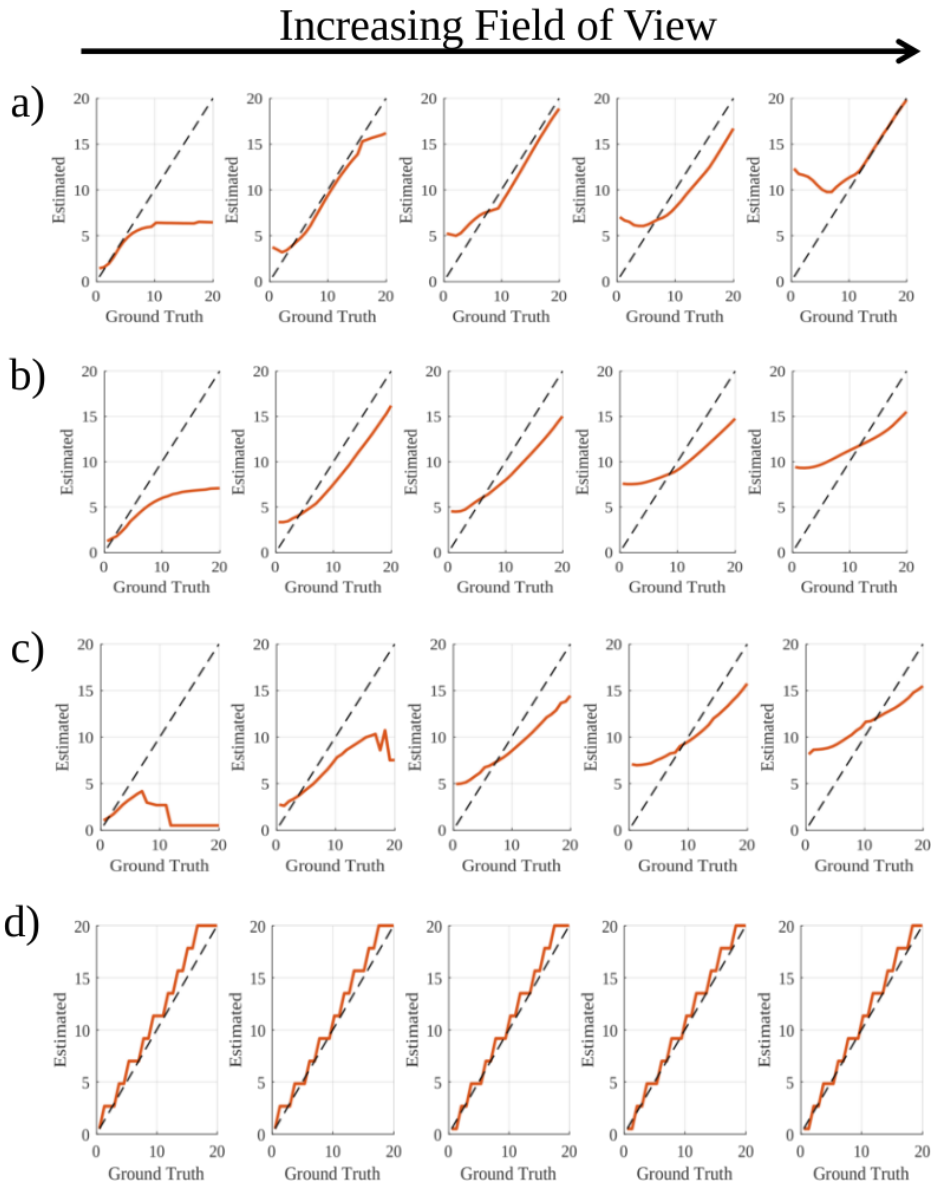


Figure 2.16.: Change in the estimation of the pRF size parameter with respect to change in field of view. All the receptive fields are centered at an eccentricity of 0. The maximum radius increases (left to right) in the range [5, 8, 12, 15, 19]. The receptive fields sizes (1 standard deviation) are in the range [0.5, 20]. The plots are generated using **a)** f-pRF_{ridge} **b)** Levenberg-Marquadt (Levenberg, 1944) with pRF location parameters estimated using f-pRF_{ridge} and **c)** an exhaustive search for pRF parameters for initial guess followed by maximum likelihood estimation (Mineault, 2021) **d)** vanilla grid search.

* 2.4. DISCUSSION

We propose a fast approach for receptive field mapping and pRF parameter estimation that is suitable for real-time applications. A linear voxel-to-pixel map typically is a huge data matrix which requires a large amount of memory in order to be stored and to be operated on; rendering operations slow. To reduce data by more than 90%, we encode the stimulus using tile coding and hashing. This lowers memory requirements and hence strongly reduces computational time. We evaluated our approach on simulated as well as real empirical data in terms of computational times, correlations between predicted and acquired BOLD signals, fidelity of estimated receptive field shapes and parameters and the suitability of estimated pRF shapes for projecting cortical activity back into the visual field.

We find that our approach is extremely fast at mapping receptive field shapes and estimating their parameters with computational times on the order of seconds and ~ 1 minute, respectively. Specifically, because our approach can successfully estimate receptive field shapes for large amounts of voxels in mere seconds, it is straightforward to identify visually responsive voxels by conducting a quick cross-validation procedure. This allows limiting parameter estimation to these voxels and thus to keep computational time low for this process as well. This also eliminates the need of using a pre-defined mask; though such a mask may be used in addition. Furthermore, cross-validation is performed in batches and we provide the option of adjusting the batch size which can further speed up parameter estimation. The only other approach, to date, that facilitates fast mapping of pRFs is based on training deep neural networks to predict pRF parameters (DeepRF; [Thielen et al., 2019](#)). Our method is fundamentally different from DeepRF and does not assume initial shape of the pRFs. In terms of computation time, our approach remains significantly faster. Average computational time required per voxel is less than a second for DeepRF. It has been reported in ([Thielen et al., 2019](#)), that the computation time required per voxel is on the order 10^{-2} seconds (excluding the time required for training). In the case of f -pRF_{ridge}, the computational time required per voxel for parameter estimation is on the order 10^{-5} seconds.

In terms of fidelity, we observe excellent correspondence between estimated pRFs and ground-truth pRFs both in terms of shapes and parameters for simulated data. For empirical data, we observe excellent correspondence between pRF locations estimated from our procedure and from GS-pRF (as described [2.2.4](#)). However, for pRF size, results of the two methods correspond less well. In particular, for larger eccentricities correspondence is poor. We observed that the receptive fields at high eccentricities; i.e., located at or beyond the border of the stimulated region of the visual field, tend to be anisotropic (elongated) and mostly underestimated. It has been reported in ([Greene et al., 2014](#)) that pRFs located in the proximity of this border tend to be underestimated. Studies such as ([Silson et al., 2018](#); [Merkel et al., 2018, 2020](#)) further report

elongation of receptive fields and (Silson et al., 2018) report that the aspect ratio of receptive fields increase with eccentricity. In order to investigate how reliable our mapping procedure is when the underlying receptive fields are elongated and when the receptive fields are located near the stimulus border we conducted additional, unplanned, analyses.

First, we simulated data based on elliptical receptive fields. We observed excellent correspondence between pRF parameters from our approach and ground-truth parameters. Our algorithm estimated the size of such elliptical receptive fields better than the GS-pRF method. This means that our method is more flexible and freer in capturing the shape of the receptive fields than model-based methods. As such, our method is in principle able to capture the true shape of a receptive field. However, an analysis of how receptive field size estimates are effected by their eccentricity and the visual field of view revealed that estimates are only accurate within a certain region of the visual field of view. Our analysis revealed that a major limitation of our approach is the inability to reliably estimate receptive fields that are located at or beyond the stimulus border (lie outside the visual field of view). In order to accommodate such receptive fields, we recommend setting up the experiment with a larger field of view (Figure 2.15). Our analysis also suggests that there exists a trade-off between the size of the field of view and reliable estimation of receptive fields. Having a large field of view may hamper reliable estimation of relatively small receptive fields (Figure 2.16), if the stimulus needs to be enlarged to cover the expanded field of view with the same number of steps. In order to reliably estimate small receptive fields with a large field of view, we recommend increasing the number of steps in which the stimulus sweeps the space (thereby increasing the length of the experiment). Alternatively, if fast estimation of pRF parameters is not an issue, one could consider utilizing a vanilla grid-search method as it is less susceptible to these effects (Figures 2.15d and 2.16d).

The flexibility of our method comes thus at the cost of an inability to deal with large, circular, receptive fields that lie beyond the field of view (i.e. outside the region of stimulation). This is in line with the observation that linear encoding methods (such as ridge regression) fail to reliably estimate large receptive fields (Lage-Castellanos et al., 2020); or rather those receptive fields that partially lie beyond the field of view. In the pRF validation framework established by (Lerma-Usabiaga et al., 2020a), the authors report that pRF size estimates significantly depend on the HRF model, and varies significantly from implementation to implementation. Similar observations have been made by Lage-Castellanos et al.(2020). However, both studies report negligible differences in location estimates. This is in line with our findings.

Nevertheless, for the purpose of projecting cortical activations back into the visual field, the true shape of receptive fields at the edges of the visual field do not matter. Indeed, as can be seen from Figure 2.10, our model-free approach faithfully reconstructs the letter shapes from their associated BOLD activity. Recognizable reconstructions of

these shapes were possible even though data underwent real-time preprocessing which is generally considered being of lower quality than offline preprocessing. This highlights that our method is suitable for real-time applications such as content-based BCI letter-speller systems.

In that context it is also important to highlight that the results reported here were obtained using a single set of hyperparameters (learning rate, FWHM and shrinkage factor) except for reconstruction of mental imagery where we used a higher shrinkage factor. While hyperparameters were obtained using Bayesian Optimization on the simulated dataset (refer to A.2), the set of hyperparameters used here produced robust results for empirical data obtained from different participants, field strengths and pre-processing procedures. We provide an example script for Bayesian Optimization as well as for generating synthetic data to allow potential users of our method to adjust hyperparameters to their specific experimental setups and needs (https://github.com/ccnmaastricht/real_time_pRF). We also encourage users to report their stimulus, setup and the hyperparameters that they found optimal for their dataset/experiment (<https://forms.gle/3hXd4DT6ixvcGJtu6>). This information will be compiled to offer optimized user-recommendations on the wiki of the Computational Neuroimaging Toolbox.

In conclusion, we present an extremely fast and flexible pRF mapping approach which can be either used in parallel with data acquisition (f -pRF_{gd}) or after the data has been fully acquired (f -pRF_{ridge}). This opens the door for real-time applications that rely on pRF estimates such as BCI speller systems. We also propose a fast method to estimate pRF parameters. A limitation of this method, and model-free approaches in general, is that receptive fields partially lying beyond the stimulus space are dealt with poorly. This can be remedied by combining fast estimation of receptive fields for voxel selection with subsequent grid-search to obtain their pRF parameters.

 3

CONNECTIVE FIELD MODELLING
USING (ALGEBRAIC) DYNAMIC
MODE DECOMPOSITION WITH
CONTROL

ABSTRACT

A population receptive field (pRF) is a contiguous region of the visual field that represents stimulus-selectivity of a population of neurons contained within one fMRI voxel. A connective field (CF) is a cortico-cortical extension to the concept of receptive fields and represents the selectivity of voxels within one brain region for the activity exhibited by a spatially contiguous group of voxels in another brain region. One limitation of existing CF models is that they do not incorporate pRFs in the model and hence cannot disentangle to what extent a voxel's activity is driven directly by the stimulus or by other voxels in the network. Another limitation, inherent to CF modelling, is that a CF map is a voxel-to-voxel map which incurs severe computational and memory-related costs. To overcome these limitations, we propose a novel, unified and computationally efficient connective field modelling framework utilizing algebraic dynamic mode decomposition with model predictive control (aDMDc). This data-driven method is model-free (no prior assumptions are made of the shape of CFs) and computes a reduced-order representation of CFs. This renders the extraction of CFs and pRFs to be a simple read-out task for the corresponding regions of interests. Another advantage of this method is that the underlying dynamics of the system can be independently isolated into temporal and spatial components. We validate our framework *in silico*, as well as on empirical fMRI data. We demonstrate that our approach is capable of efficiently and simultaneously estimating CFs and pRFs.

“One geometry cannot be more true than another; it can only be more convenient”

- Henri Poincaré, *La Science et l'Hypothèse*

❖ 3.1. INTRODUCTION

The retinotopic organization of the visual cortex, with respect to its stimulus-selectivity, has been substantially studied over the past decades. The onset of functional Magnetic Resonance Imaging (fMRI) has made population receptive field (pRF) mapping a cornerstone of computational neuroscience. However, the visual cortex is not a simple stimulus-response machine; but the cortical neurons act in concert with other neurons (Van Hemmen and Sejnowski, 2005) which, at times, are driven by the stimulus. In the past couple of decades, a fresh way of studying visual neurons has emerged, which investigates the response of neurons in one cortical area as a function of neuronal activity in a different part of the cortex (as opposed to the stimulus). This approach is often termed as *Connective Fields* (CFs) (Haak et al., 2013). But terms such as *Projective Fields* (Van Hemmen and Sejnowski, 2005) and *Cortico-cortical Receptive Fields* (Heinzle et al., 2011) are also used to address the functional connectivity under consideration.

To this date, very few methods have been developed to model CFs. Heinzle et al. (2011) use support vector regression to predict time courses of voxels in V3 from the voxels in V1. Haak et al. (2013) use a grid-search based approach (similar to pRF approach proposed by Dumoulin and Wandell (2008)) to predict time courses in V2, V3 and hV4 from the voxels in V1. Motivated by the findings of Motter (2009) and Kumano and Uka (2010) from monkey studies, Haak et al. (2013) assume the CFs to be a bivariate and isotropic Gaussian projected over the cortex. Zimmermann (2014) (in Chapter 4) use a ridge regression-based approach to predict laminar connectivity from V1 to V2. More recently, a bayesian approach for modelling CFs has been proposed by Invernizzi et al. (2022). This approach has also been further validated on the data from 3T scanners (which are more commonly available than 7T scanners) for its uncertainty and reliability (Invernizzi et al., 2021).

One of the main issues with these CF modelling methods is that they do not account for the part of the response that is generated through pRFs. If an MRI voxel has both CFs and pRFs, the previously mentioned methods would fail to capture, the voxel's activity as a combined response of CFs and pRFs. Although, the need for such a unified intrinsic and extrinsic (stimulus-driven) model has been expressed in Van Hemmen and Sejnowski (2005), but a methodological implementation of such a model remains largely unaddressed to this day. Another innate issue with CFs is that their modelling results in a *voxel-by-voxel* map. Given the enormous number of voxels, such a CF map can typically consume a great deal of computational resources.

In order to establish a unified CF and pRF framework, we make use of algebraic Dynamic Mode Decomposition with control (aDMDc, Fonzi et al. (2020)). aDMDc is a variant of regular Dynamic Mode Decomposition (Schmid, 2010) that incorporates algebraic terms with model predictive control (Proctor et al., 2016). DMD and its vari-

ants are widely used in fluid dynamics. DMD, uses a truncated Singular Value Decomposition (Hansen, 1987) based approach to approximate reduced order model (ROM) of a state-transition matrix which is low rank in structure. Such a low rank ROM approximation allows for independent estimation of spatial and temporal dynamics of the system without actually estimating the large (full) state-transition matrix.

We propose here a novel and efficient method to simultaneously map CFs and pRFs in one unified model. We model CFs as a state-transition matrix and pRFs as a predictive control. DMD-based approach allows for a reduced order approximation of full CF matrix. In order to compute CFs from source to target regions of interest (ROI), one can simply read them out from the reduced order model, instead of calculating the full matrix. However, the pRF matrix (*pixel-by-voxel*) remains a large quantity that needs to be estimated. In order to tackle this, we encode the stimulus with hashed-Gaussians (Bhat et al., 2021). The ROM from DMD and hash-encoded stimulus significantly reduces the computational time and memory consumption.

We validate our approach on simulated data (similar to the simulated data used in Bhat et al. (2021)) and on 7T empirical data (Allen et al., 2022). We observe excellent correspondence between predicted BOLD signal and ground-truth BOLD signal. We also observe good fidelity between estimated and ground-truth CFs, pRFs and pRF parameters. Finally, to present the contiguity of estimated CFs, we project them on the cortex.

* 3.2. METHODS

3.2.1. Dynamic Mode Decomposition and its variants

Standard DMD

DMD (Schmid, 2010) is a popular technique, primarily used in fluid dynamics, to extract underlying physical mechanisms and dynamics of relative large data sequences (flow fields). In practice, the DMD framework developed by Tu et al. (2014) (also known as *exact* DMD) is considered to be the standard DMD (Brunton and Kutz, 2022). DMD assumes the following linear discrete dynamical system sampled from a continuous (flow) process at time intervals of Δt :

$$x(t + \Delta t) = Ax(t) \tag{3.1}$$

Where x is a snapshot of a system's state at time t and A is a state transition matrix. Assuming $\Delta t = 1$

$$x(t + 1) = Ax(t) \tag{3.2}$$

Above equations can be written in matrix form as:

$$X' = AX \quad (3.3)$$

where X and X' is the collection of snapshots of the system which are separated in time by Δt . DMD tries to find the best low-rank fit solution for the operator A by collecting multiple snapshots of the system over time. Mathematically, the best low-rank approximation of A can be obtained by:

$$A = \underset{A}{\operatorname{argmin}} \|X' - AX\|_F = X'X^\dagger \quad (3.4)$$

where $\|\cdot\|_F$ is the Frobenius norm and \dagger denotes Moore-Penrose pseudo-inverse.

One of the simplest and computationally efficient ways of solving this system is to take pseudo-inverse of the matrix X using truncated SVD (Singular Value Decomposition) (cf. [Hanson, 1971](#); [Varah, 1973](#)). Standard SVD decomposes the matrix $X \in \mathbb{R}^{n \times m}$ (where $n \gg m$) as:

$$X = U\Sigma V^T \quad (3.5)$$

where

$$\begin{bmatrix} | & | & \dots & | \\ X_1 & X_2 & \dots & X_m \\ | & | & & | \end{bmatrix} = \begin{bmatrix} | & | & \dots & | \\ U_1 & U_2 & \dots & U_n \\ | & | & & | \end{bmatrix} \begin{bmatrix} \sigma_1 & 0 & 0 & 0 \\ 0 & \sigma_2 & 0 & 0 \\ 0 & 0 & \ddots & 0 \\ 0 & 0 & 0 & \sigma_m \\ \vdots & \vdots & \vdots & \vdots \\ 0 & 0 & 0 & 0 \end{bmatrix} [V_1 \ V_2 \ \dots \ V_m]^T \quad (3.6)$$

Truncated SVD aims to obtain a best low rank approximation of X by only keeping top r singular values (where $r \ll n$) (Eckart-Young Theorem, [Eckart and Young \(1936\)](#)).

$$X \approx \tilde{U}\tilde{\Sigma}\tilde{V}^T \quad (3.7)$$

And the operator A can be subsequently approximated as:

$$A \approx X'\tilde{V}\tilde{\Sigma}^{-1}\tilde{U}^T \quad (3.8)$$

A general property of SVD is that the matrices U and V are orthogonal; which means that the inverse operation of these matrices is simply a transpose operation. Also, the matrix Σ is a diagonal matrix and its inverse is simply one over the singular values. This makes inverting the matrices, yielded from SVD, more computationally efficient than inverting the matrix itself.

However, in order to extract the underlying dynamics of the system, computation

of the full A is not necessary. Instead, one can obtain reduced order model \tilde{A} . This is done by projecting the A matrix onto an orthogonal basis of \tilde{U} .

$$\tilde{A} = \tilde{U}^T X' \tilde{V} \tilde{\Sigma}^{-1} \quad (3.9)$$

The matrix $\tilde{A} \in \mathbb{R}^{r \times r}$ is much smaller than the matrix $A \in \mathbb{R}^{n \times n}$ (since $r \ll n$). This makes the whole procedure very memory efficient. It has been shown by Schmid (2010) that the eigenvalues of \tilde{A} and A are equivalent and the eigenvectors scale linearly. This would mean \tilde{A} is sufficient to extract spatial (eigenvectors) and temporal (eigenvalues) dynamics of the system.

Dynamic Mode Decomposition with Control (DMDc)

Many real-world complex systems are often actuated by an external force or control. For example, in epidemiology, the spread of infectious diseases can be controlled by vaccinations or other preventive measures. DMDc (Proctor et al., 2016) was developed to extend standard DMD to model predictive control. DMDc can be formulated as:

$$x_{t+1} = Ax_t + Bu_t \quad , \quad X' = AX + BU \quad (3.10)$$

where A is the state-transition matrix and U is the external control or stimulus. In order to solve this system in DMD tone, the system can be manipulated as:

$$X' = [A \quad B] \begin{bmatrix} X \\ U \end{bmatrix} = G\Omega \quad (3.11)$$

The matrix G can be approximate by simply inverting the truncated SVD of Ω (just like DMD).

$$G \approx X' \tilde{V} \tilde{\Sigma}^{-1} \tilde{U}^T \quad (3.12)$$

In order to obtain A and B , G can be disassembled as:

$$G \approx [A \quad B] \approx \left[X' \tilde{V} \tilde{\Sigma}^{-1} \tilde{U}_1^T \quad X' \tilde{V} \tilde{\Sigma}^{-1} \tilde{U}_2^T \right] \quad (3.13)$$

where \tilde{U}_1 and \tilde{U}_2 are obtained by splitting \tilde{U} according to the columns of A and B respectively. Similar to DMD, reduced order \tilde{A} can be directly obtained by projecting A to an orthogonal basis. Unlike DMD, in this case, the orthogonal basis would be \hat{U} , which is obtained by computing SVD of X' (instead of X).

$$\tilde{A} = \hat{U}^T X' \tilde{V} \tilde{\Sigma}^{-1} \hat{U}_1^T \hat{U} = \hat{U}^T A \hat{U} \quad (3.14)$$

Algebraic DMDC (aDMDC)

aDMDC [Fonzi et al. \(2020\)](#) was developed to solve algebraic differential equations in a DMDC way. The algebraic differential system can be formulated as:

$${}^1x_{t+1} = Ax_t + Bu_t \quad (3.15)$$

$${}^2x_{t+1} = Fu_{t+1} \quad (3.16)$$

where Equation 3.15 is the differential term and Equation 3.16 is the algebraic term. This system can be rewritten as a single linear system as:

$$X' = AX + BU + FU' \quad (3.17)$$

This system can be solved in a DMDC way simply by concatenating matrices as:

$$X' = [A \quad B \quad F] \begin{bmatrix} X \\ U \\ U' \end{bmatrix} = \Psi\Omega \quad (3.18)$$

The reduced order models can then be computed as:

$$\tilde{A} = \hat{U}^T X' \tilde{V} \tilde{\Sigma}^{-1} \tilde{U}_1^T \hat{U} \quad (3.19)$$

$$\tilde{B} = \hat{U}^T X' \tilde{V} \tilde{\Sigma}^{-1} \tilde{U}_2^T \quad (3.20)$$

$$\tilde{F} = \hat{U}^T X' \tilde{V} \tilde{\Sigma}^{-1} \tilde{U}_3^T \quad (3.21)$$

where \tilde{U} , $\tilde{\Sigma}$ and \tilde{V} are obtained from truncated SVD of Ω and \hat{U} is obtained from truncated SVD of X' , which are truncated at the thresholds of ρ_1 and ρ_2 respectively.

3.2.2. Connective Field Modelling using aDMDC

We model both CFs and pRFs in an aDMDC framework. We assume that one part of the BOLD response at time $t + \Delta t$ is explained by the the BOLD response at time t through CFs, which may or may not be controlled by a stimulus at time t through pRFs. And the other part of the BOLD response at time $t + \Delta t$ is explained exclusively by the stimulus at time $t + \Delta t$ through classical pRFs. Note that, the Δt here is limited by the one TR of fMRI. This is mathematically equivalent to Equation 3.17. Where X is the BOLD response, A is the CF matrix and F and B are the receptive the field matrices and U is the stimuli presented.

In order to further reduce the computational load, we employ the same strategy as used by [Bhat et al. \(2021\)](#), to hash-encode the stimulus and then convolve it with hemodynamic response function to create time courses. The stimulus U is hashed to Υ . And the matrices B and F are changed to matrices H and K respectively, which denote the linear weights on the hashed stimuli. For hashing, we use the same tiling parameters as reported in [Bhat et al. \(2021\)](#), that is 250 tiling with 5 Gaussian tiles within each tiling. This system with hash-encoded stimuli can be written as:

$$X' = AX + H\Upsilon + K\Upsilon' \quad (3.22)$$

The reduced order CF matrix \tilde{A} can now be estimated in exactly the same way as Equation 3.19. The full order CFs between source and target ROIs can now simply be read-out as:

$$A_{ROI} = \hat{U}_{target} \tilde{A} \hat{U}_{source}^T \quad (3.23)$$

3.2.3. Simulated Data

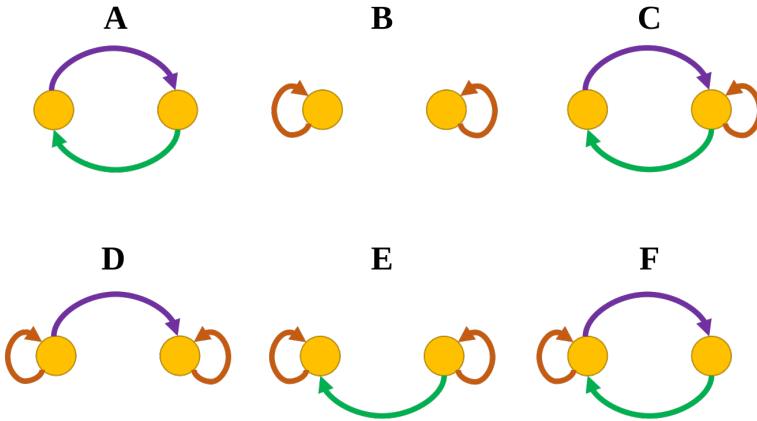


Figure 3.1.: Schematic illustrations of different connectivity scenarios between two brain areas.

In order to validate our framework on ground-truth quantities, we generate biologically plausible data for functionally simulating V1. The method for generating V1 data is described in [Bhat et al. \(2021\)](#). In order to functionally simulate a higher visual area, we simply add another set of voxels whose responses result from a linear combination of activity exhibited by V1 units and not from the stimulus. The neuronal responses are generated by multiplying a connective field model and neuronal responses generated in the lower visual area. We simulate six different scenarios (illustrated in Figure 3.1) which are different combinations of feedforward, feedback and lateral connectivities.

We model the connective field as a 2D isotropic Gaussian over a flattened (simulated) cortical surface. Note that, we do not generate time-shifted time courses. The stimulus presentation and transfer of activity between low and high visual areas, all happens within same TR (Δt). This is done to stay as close as possible to real-time data acquisition which is restricted by fMRI's TR.

3.2.4. Empirical Data

After validating our approach on the simulated dataset, we demonstrate its applicability to a real brain dataset. For that purpose, we use [Natural Scenes Dataset \(NSD\)](#) ([Allen et al., 2022](#)). The NSD dataset contains measurements of fMRI responses from 8 participants obtained using a 7T fMRI machine. For this work we only use the 1st run out of 12, pRF and category functional localizer runs. We use the high-resolution version of the data which was sampled at 1mm (TR = 1000ms). The pRF stimulus used was a sweeping bar stimulus.

* 3.3. RESULTS

3.3.1. Simulated Data

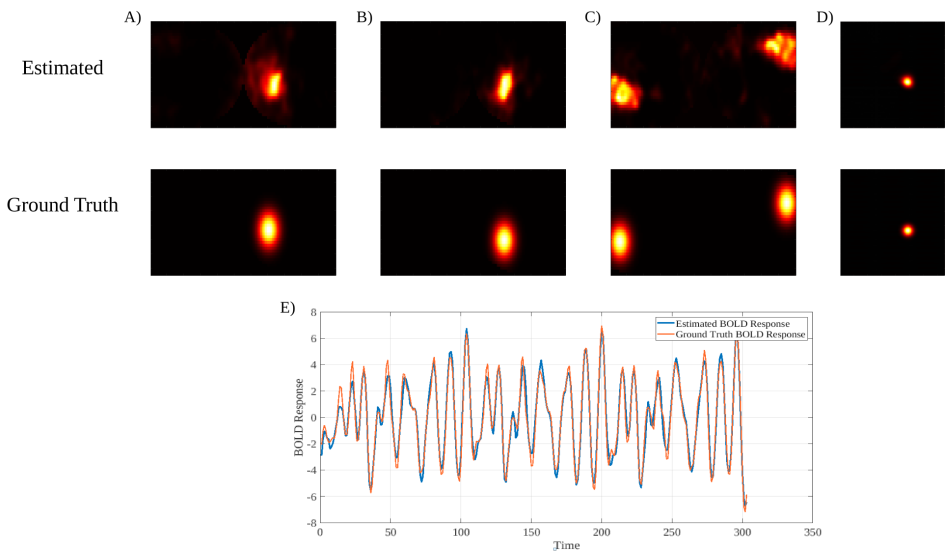


Figure 3.2.: Comparison between estimated and ground-truth quantities on the simulated dataset. A-C) CFs estimated with connectivities corresponding to connections A, B and C in Figure 3.1. D) Population receptive fields. E) BOLD response.

The quantities estimated using our approach (namely CFs, pRFs and BOLD response) are compared with their ground-truth counterparts in Figure 3.2. We also display CFs estimated on different connectivities such as feedforward/feedback, lateral and their combinations (Figure 3.2 A, B and C). It can be seen from Figure 3.2 that there is good visual correspondence between the estimated and the ground-truth quantities. It can also be seen that in case of a combination of feedforward/feedback and lateral connections, a voxel can have two CFs. One CF is lateral (the same visual area) and the other is from another visual area. In this case, the CF estimation is relatively poor when compared to single CFs. Nevertheless, there is some fidelity towards ground-truth CFs. The pRFs and BOLD response show excellent correspondence with ground-truth data. The visualizations of CFs and pRFs are obtained after applying shrinkage (as described in Bhat et al. (2021)) in order to shrink noisy, small-value pixels towards 0. Furthermore, we estimate pRF parameters using the method described in section 2.2.3. The correspondence between estimated pRF parameters and ground-truth parameters is depicted in Figure 3.3. It can be seen that there is an excellent correspondence between the parameters, with correlation coefficients being 0.9721, 0.9674 and 0.9412 for pRF locations (along X and Y coordinate axes) and pRF size, respectively.

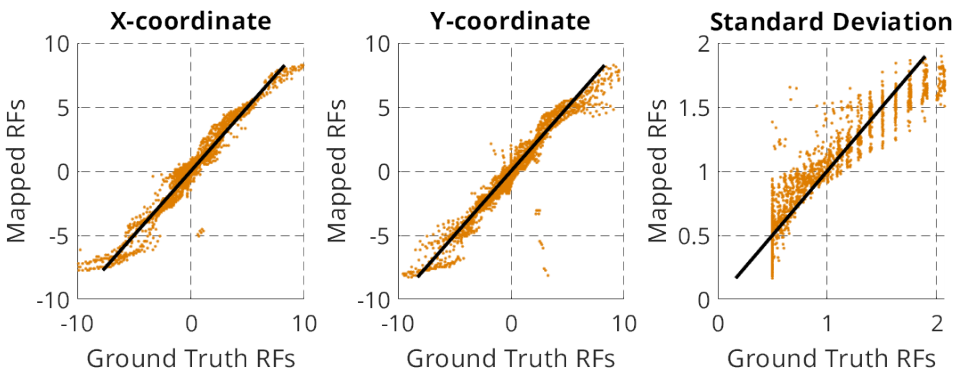


Figure 3.3.: Comparison between estimated pRF parameters and ground-truth pRF parameters

In order to quantify these correspondences, we use the conservative metric of Jaccard Similarity. Metrics such as the correlation coefficient can often be misleading. Figure 3.4 compares cross-validated (Roberts et al., 2017) Jaccard Similarities and Correlation Coefficients per voxel. It can be seen that correlations are always high regardless of the voxel. On the other hand, Jaccard Similarities are dispersed over a wider range, thus justifying our choice of similarity metric. However, the similarity depends largely on the truncation threshold of SVD. For the visualizations, we used the *Gavish-Donoho threshold* (Donoho and Gavish, 2013), which is widely used in DMD literature, including aDMDc Fonzi et al. (2020). However, this threshold does not provide enough insight into to what extent the threshold affects estimation of individual quantities (in our case CFs and pRFs). In order to address this, we scrutinize the effect of truncation threshold

with further analysis.

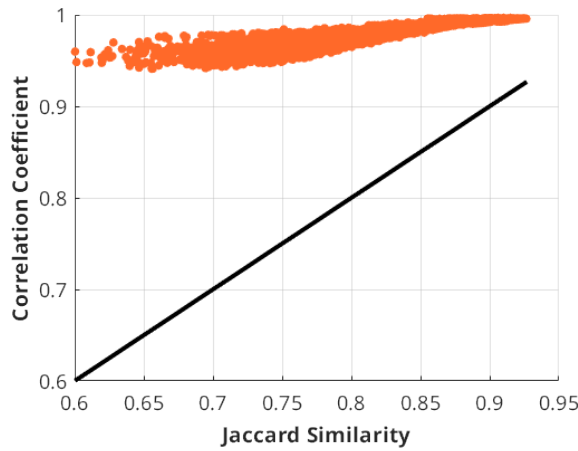


Figure 3.4.: Comparison between estimated pRF parameters and ground-truth pRF parameters

Truncation threshold analysis

Computation of the low-rank approximation of CF or the low-rank state transition matrix \tilde{A} , requires two thresholds, ρ_1 and ρ_2 , for truncated SVD on Ω and X' respectively (refer to section 3.2.1). We evaluate the effect of these thresholds on Jaccard Similarity (JS, also known as Jaccard Index) between estimated and ground-truth quantities for all connectivity scenarios. Figure 3.5 depicts the JSs over all possible values of thresholds over all connectivity scenarios, ground truth quantities (CFs, pRFs and BOLD response). We choose JS because of its conservative nature and correlations can often be misleading. In case of BOLD response, we report cross-validated JSs. In order to deal with autocorrelated BOLD response, we use block cross-validation (Roberts et al., 2017). With rows and columns representing all the possible values of ρ_1 and ρ_2 , respectively. In addition to that, for each connectivity and ground-truth quantity, we normalize the JSs between $[0, 1]$ so that they can be multiplied (symbolized by $\mathbf{\Pi}$ in Figure 3.5) to get aggregated JSs. The final product, or the *product of products*, depicts an aggregated or global JS over all connectivities and ground-truth quantities. Finally, we also show a magnified version of the final product to illustrate the position of *Gavish-Donoho* thresholds versus the thresholds yielding maximum aggregated JS.

It can be seen from Figure 3.5 that JS profiles do not change across connectivities. The JS between estimated and ground-truth BOLD response is excellent for most of the thresholds. This means that aDMDC is, in general, excellent at modelling and predicting the timecourses. The highest JS for BOLD response is observed for very high thresholds. The aggregated JSs of pRFs and CFs, have similar overlapping profiles. The

final products give an idea about the region of thresholds to consider to get overall good JS, without optimizing for individual quantities. It can also be observed that this region demands higher thresholds than *Gavish-Donoho* thresholds.

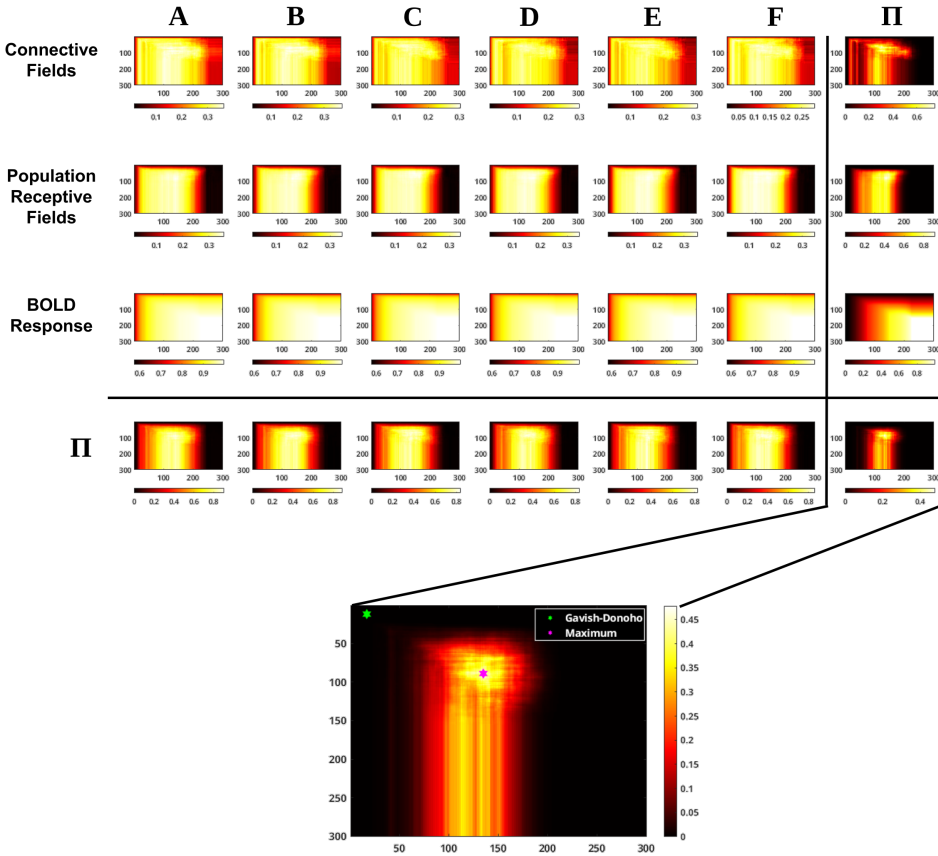


Figure 3.5.: Evaluation of truncation thresholds on Jaccard Indices (similarity) (and their products) for various scenarios. **Top left grid (3-by-7):** Each element depicts the Jaccard Similarity (JS) between estimated end ground-truth quantities. The columns correspond to different connectivities (A-F), as depicted in Figure 3.1. The rows are the quantities on which JSs were calculated. **II:** This symbol represents product of normalized $([0, 1])$ JSs. The bottom-left II represents products of individual columns (connectivities) and the top-right II represents product of individual rows (CFs, pRFs and BOLD response). **Bottom-right corner element:** This element is product of all normalized $([0, 1])$ products (IIs). A magnified version of this element is depicted below the grid, which also depicts the position of *Gavish-Donoho* (Donoho and Gavish, 2013) threshold and maximum JS or product of products.

Balanced Similarity

It is to be noted that, when dealing with real-world empirical data, researchers do not have the luxury of having ground-truth pRFs and CFs. As can be seen from Figure 3.5,

the higher the threshold, the better the model gets at fitting the BOLD response. However the computational efficiency would decrease with high thresholds. The idea of an optimal threshold would be to keep the rank as low as possible without compromising important structures (singular values) in the system. Thus making selection of threshold a *balancing* act between good approximation and good (computational) efficiency. In order to examine thresholds with this point of view, we propose here a data-driven metric which uses JS as similarity metric but penalizes high thresholds. We refer to this metric as *balanced similarity* (denoted by β).

The truncation thresholds are simply discrete (integer) indices which are limited by the number of time points. Thus, their “magnitude” is neither scalable nor interpretable. We instead use the Frobenius norm as a proxy to a threshold’s magnitude. The Frobenius norm of a matrix is equal to the $L2$ norm of singular values ($\|\cdot\|_F = \sqrt{\sum_i \sigma_i^2}$), which increases with the magnitude of the threshold. Since we are dealing with two different thresholds, we use the geometric mean of the two Frobenius norms to calculate the effective magnitude of the two thresholds. Thus, the balanced similarity β for two thresholds ρ_1 and ρ_2 can be defined as:

$$\beta(\rho_1, \rho_2) = \underbrace{\frac{\sum_i \min(\zeta_i, \tilde{\zeta}_i)}{\sum_i \max(\zeta_i, \tilde{\zeta}_i)}}_{\text{Jaccard Similarity}} \left(1 - \sqrt{\sqrt{\sum_{\rho_1} \sigma_{\rho_1}^2} \sqrt{\sum_{\rho_2} \sigma_{\rho_2}^2}} \right) \quad (3.24)$$

Where $\zeta_i \in Z$ and $\tilde{\zeta}_i \in \tilde{Z}$ are true and estimated quantities of interest (pRF, CF and BOLD, respectively). The geometric mean is rescaled to $[0, 1]$.

Figure 3.6 evaluates the effect of thresholds in terms of balanced metric. It can be clearly seen from the global product (product of products), that the thresholds yielding maximum similarity are very close to the Gavish-Donoho thresholds. This suggests that the Gavish-Donoho is indeed good choice of data-driven threshold for optimally extracting low-rank structures. Note that, the similarity matrices were computed over a grid of all possible values of thresholds. This was done for illustrative purposes only. In practice, it is recommended using converging algorithms such as Bayesian Optimization with a custom loss function, in order to optimize thresholds in an efficient way.

The actual values of estimated thresholds and corresponding Jaccard Similarities are reported in Table 3.1a and 3.1b respectively. Since the JS profiles do not change for different connectivities, we report the thresholds estimated only for connectivity **A**. Since JS is a conservative approach, we compare it to a null-model to obtain baseline JSs. The null-model consists of randomly generated quantities to compare with ground-truth quantities. We get JSs higher than baseline regardless of the thresholds. The JSs are especially high for the BOLD response. The difference in JSs estimated from pRFs

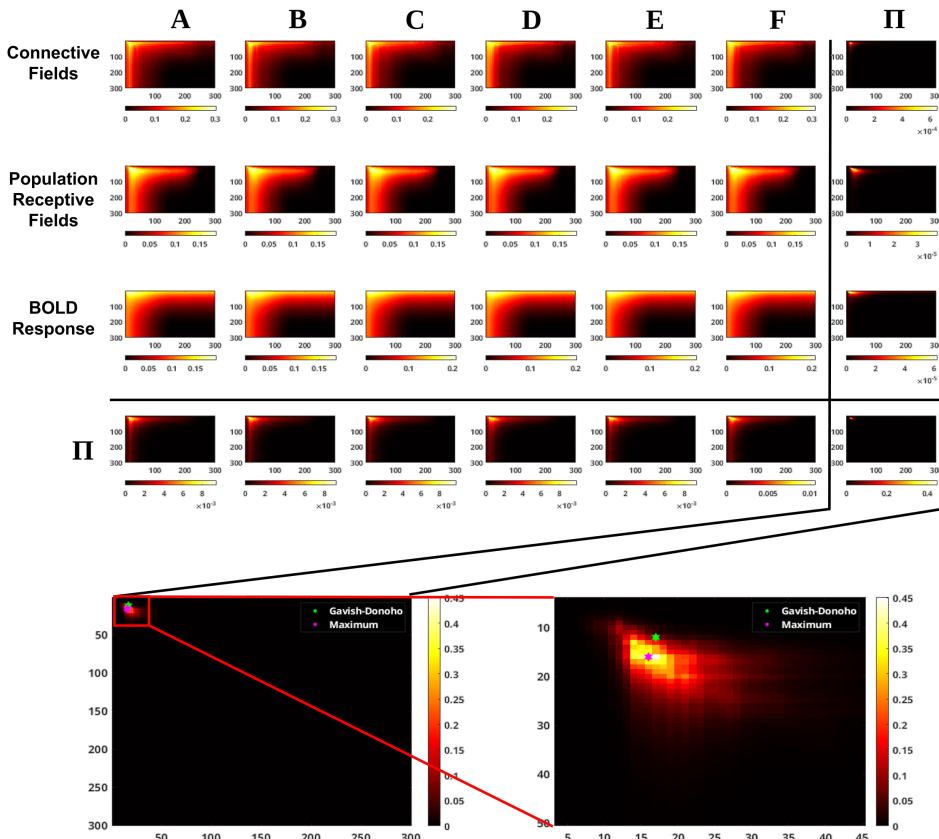


Figure 3.6.: Evaluation of truncation thresholds on *balanced similarities* (and their products) for various scenarios. The figure is organized just like the Figure 3.5 except for the similarity metric. In this figure, *balanced similarities* (and their products) are used.

is higher than the JSs estimated from CFs. This indicates that in order to get better pRFs, one should use a higher thresholds than Gavish-Donoho threshold or the ones estimated from the balanced similarity.

Lastly, in order to measure the computational performance of our approach, we report in Figure 3.7 the time required (in seconds) to compute CFs over a range of voxels. The computation time is the total time required for performing two SVDs and compute \hat{A} . The reported computation time, per number of voxels, is the mean over 10 runs. The hardware used was an HP[®] Z440 workstation with an Intel[®] Xeon[®] Processor (E5-1650 v4, 32GB RAM) and the software was MATLAB[™](version 2022a, The Mathworks .inc, Natick, MA, USA).

	CF	pRF	BOLD	Global	Gavish-Donoho	Balanced
ρ_1	88	88	161	89	12	16
ρ_2	120	140	225	135	17	16

(a)

	Local	Global	Gavish-Donoho	Balanced	Baseline
CF	0.3631	0.3563	0.2574	0.3001	0.0760
pRF	0.3582	0.3489	0.1424	0.1815	0.0481
BOLD Response	0.9993	0.9638	0.7806	0.7940	0.0372

(b)

Table 3.1.: **a)** SVD truncation thresholds (ρ_1 and ρ_2), from left to right, yielding the best JS for estimated quantities (CFs, pRFs and BOLD response), thresholds yielding the best global (aggregated) JS, Gavish-Donoho thresholds and balanced thresholds. **b)** JSs of estimated quantities for different thresholds: (from left to right) best individual thresholds, best global (aggregated) thresholds, Gavish-Donoho thresholds, Balanced thresholds and null-model JSs.

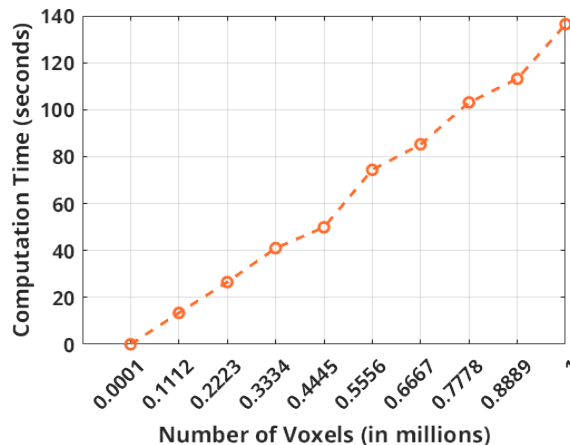


Figure 3.7.: Mean computational time (over 10 runs) over a range of voxels. The total computational time per run includes the time required to compute the two SVDs and \tilde{A}

3.3.2. Empirical Data

We, further, validate our approach on empirical data obtained from [Allen et al. \(2022\)](#). Firstly, in order to test how good our model fits the data, we compute both Jaccard Similarity and Correlation Coefficient between estimated and true BOLD signal. Additionally, we compare our unified model to pRF-only model (as proposed by [Bhat et al. \(2021\)](#)). It can be seen from Table 3.2, that our model significantly outperforms the pRF-only model. Also, the correlation coefficients obtained from the fast pRF ap-

Subject	Correlation Coefficient		Jaccard Similarity	
	Fast pRF Mapping	Unified Model	Fast pRF Mapping	Unified Model
01	0.5851	0.9866	0.2079	0.7421
02	0.5873	0.9905	0.2077	0.7457
03	0.6083	0.9892	0.2473	0.7282
04	0.6089	0.9861	0.2624	0.7150
05	0.6177	0.9860	0.3270	0.7277
06	0.5899	0.9859	0.2118	0.7389
07	0.6094	0.9894	0.2419	0.7518
08	0.5987	0.9849	0.2497	0.7376

Table 3.2.: Comparison between Fast pRF mapping (Bhat et al., 2021) and unified model proposed here, in terms of Jaccard Similarity and Correlation Coefficient. Both metrics are obtained after cross-validation

proach are in a similar range as reported by Bhat et al. (2021) on the empirical data. This suggests that pRF alone is not enough and the CF term is indeed necessary to completely account for BOLD response. Secondly, we also visualize exemplary CFs (for $V1 \succ V3$ and $V2 \succ V3$ respectively) from Subject 01 on a cortical surface in Figure 3.8.

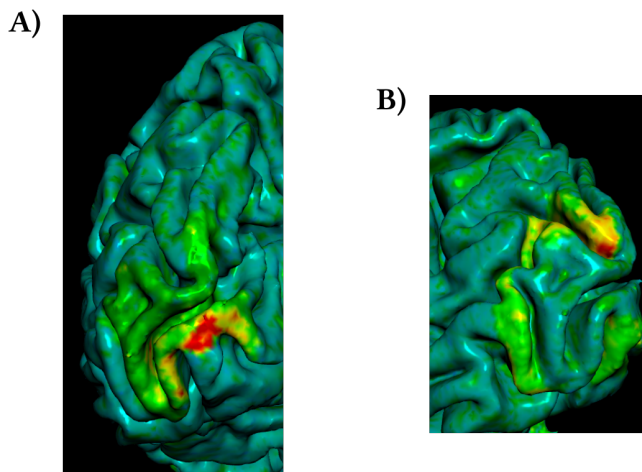


Figure 3.8.: Visualizations of CFs on a cortical surface (for a *Source* \succ *Target*). **A)** $V1 \succ V3$ and **B)** $V2 \succ V3$. The CFs were visualized with beta threshold B2, which uses a library-of-HRFs approach (for more details refer to Allen et al. (2022)). These visualizations were generated using BrainBrowser (Beck et al.).

❖ 3.4. DISCUSSION

In this work, we propose a unifying computationally efficient framework for modelling connective fields, which are modelled with aDMDc (Fonzi et al., 2020). Our approach not only considered stimulus-inferred neuronal activity through population receptive fields (traditional retinotopy) but also considers neuronal activity transferred from another set of neurons through connective fields. aDMDc constructs a reduced order models of both pRFs, thus allowing for a computationally efficient solution. Additionally, we hash-encode the stimulus (Bhat et al., 2021), which further increases the computational efficiency of our framework. Furthermore, our approach is model-agnostic, as in, no prior assumption is made on the shape of both CFs and pRFs.

Over the past years, very few models have been proposed to model connective fields, such as Heinzle et al. (2011); Haak et al. (2013) and Invernizzi et al. (2022). These models are either based on some sort of grid-search or compute CFs voxel-by-voxel. Given the sheer number of voxels there can be, a CF map can tremendously drag down computational performance. Furthermore, these models do not account for both CFs and pRFs simultaneously. Our model is able to tackle both of these issues. We validate our approach on both simulated data (with different connectivity scenarios) and also on the empirical data to observe how good our model is at predicting real BOLD timecourses.

On the simulated data, we observe good correspondence between estimated and ground-truth estimated CFs, pRFs and (especially for) BOLD signals. Overall, good correspondence is observed for all the different connectivity scenarios that we simulate. Additionally, we observe excellent correspondence between estimated and ground-truth pRF parameters (Figure 3.3). One inconvenience with our model is the choice of the truncation ranks. This led us to further explore how truncation ranks affect overall mapping. Although data-driven threshold estimations such as Donoho and Gavish (2013) exist, we decided to investigate this issue in the context of CF and pRF mapping. For this analysis we choose the conservative Jaccard Similarity (JS) as metric, as opposed to a correlation coefficient. We show in Figure 3.4, that correlations can be misleading. We first explored the space that yields overall good JSs over all estimated quantities (over all connectivity scenarios) (Figure 3.5). We observed that the best thresholds we get do not agree with Gavish-Donoho thresholds. On the other hand, the best thresholds we get are quite high and this can adversely affect the computational performance. In order to find an optimal threshold, that would not only produce good estimations but also keep the truncation rank as low as possible, we propose a new similarity metric, referred to as balanced similarity (Equation 3.3.1). With this new metric, we noticed that, the best estimated thresholds move much closer to Gavish-Donoho thresholds. This led us to conclude that that Gasvish-Donoho threshold is indeed a good candidate for an optimal threshold (Figure 3.6). Additionally, we also observe that similarity spaces are similar, if not identical, across connectivities, regardless of the similarity metric. And

the estimated BOLD responses are almost always good (when compared to ground-truth) and are hardly affected by the choice of thresholds.

In terms of computational time, our approach is very fast. For a million voxels, the computation time required to estimate a reduced order CF model is just over 2 minutes (Figure 3.7). However, the total computation time for a fixed number of voxels would certainly depend on the truncation thresholds. If computation time needs to be prioritized, we recommend using the Gavish-Donoho threshold which is optimally low.

We also show that our approach works well on not only on simulated data, but also on empirical data. Visually, we depict some exemplary CFs on the cortical surface, which form a neat contiguous region. We quantify our model in terms of both Jaccard Similarity and correlation coefficient and compare it with a pRF-only model (Bhat et al., 2021). While the pRF-only model performs well on the empirical data, our model significantly outperforms it (Table 3.2). This suggests that a voxel-to-voxel mapping is indeed necessary to account for a full BOLD response.

In conclusion, we provide here an efficient method for modelling the connective fields. Our model unifies CFs and pRFs in one framework without making any assumptions about the true shape of CFs and pRFs. The threshold analysis included in this work provides directions for choosing appropriate thresholds. If computation time is the priority and/or if the data is assumed to have a low-rank structure, we recommend using the Gavsih-Donoho cutoff. Otherwise, we recommend using optimization algorithms such as Bayesian Optimization to search for thresholds that would minimize a certain customized loss function. Finally, we report that our model is better at fitting the data than the pRF-only model, which suggests that voxel-to-voxel mapping is necessary for accounting for the full BOLD response, and pRFs alone are not enough.



AN INVESTIGATION INTO
PERCEPTION AND MENTAL
IMAGERY THROUGH DMD LENSES

ABSTRACT

To what extent the underlying neural mechanisms and representations overlap during perception and mental imagery, has been an actively debated subject in neuroscience. In order to compare the governing dynamics of perception and mental imagery, we inspect previously acquired fMRI data using Dynamic Mode Decomposition (DMD). Specifically, we compare the connective fields and spatio-temporal dynamics. Since fMRI data is typically huge, DMD allows for a convenient and efficient decomposition of the data into its respective spatial and temporal components. We find consistently similar distribution of connective fields during both the tasks and across subjects. We also find that there is, in general, an absence of representations of connective fields in the primary visual cortex (V1). However, we do not find any significant overlap in temporal and spatial dynamics, except for the static component (zero frequency). These findings suggest that although mental imagery and perception share information pathways (connective fields), their spatio-temporal dynamics are arbitrary regardless of the task and the subject.

“The real purpose of the scientific method is to make sure Nature hasn’t misled you into thinking you know something you don’t actually know.”

- Robert M. Pirsig, *Zen and the Art of Motorcycle Maintenance*

❖ 4.1. INTRODUCTION

Visual experience, the largest part of our sensory experience, can be driven externally and/or internally (Dijkstra et al., 2019). The externally driven visual experience, known as *perception*, is triggered when light is incident upon the retina. And the internal experience, triggered by high level processes (such as working memory (Baddeley and Andrade, 2000; Keogh and Pearson, 2011; Tong, 2013)), is known as *mental imagery*. Despite being differently driven experiences, there has been a mounting evidence, that they both share similar neural representations in early visual areas (Albers et al., 2013; Dijkstra et al., 2017a) and late visual areas (Stokes et al., 2009; Reddy et al., 2010; Lee et al., 2012; Pearson, 2019). Despite of the agreement between the neural representations, the question of to what extent the underlying neural mechanisms and dynamics overlap, remains ambiguous.

In order to address this question, we use exact Dynamic Mode Decomposition (DMD; Tu et al., 2014; Brunton and Kutz, 2022) on the mental imagery and perception fMRI data used by Senden et al. (2019). DMD is a powerful data-driven tool, popularly used in fluid dynamics, and is incredibly useful for analyzing large real-world dynamical systems. DMD yields a reduced-order model of the system whose eigenvalues (temporal dynamics) are same as the full-order model and eigenvectors (spatial dynamics) scale linearly with the eigenvectors of the full-model. These eigenvalues and eigenvectors can be conveniently used to deconstruct the system into its dominant temporal and spatial (also known as DMD modes) components.

We use DMD to obtain the connective field matrix and spatio-temporal dynamics of mental imagery and perception to investigate the overlapping features. Due to the absence of retinotopic stimuli, we use DMD without any control. This way, the neuronal activity in the visual cortex is solely explained by intrinsic dynamics. Before we analyze such a dynamical system, we first ensure that our model faithfully explains the data. We observe a consistent connective field distribution across perception and mental imagery and across subjects. We also observe that most connective fields originate in V2 and V3, with negligible presence in V1. Furthermore, we observe no meaningful overlap within and across perception and mental imagery. These findings suggest that connective fields are inherent structures in the visual cortex which are shared by both perception and mental imagery. However, their spatio-temporal dynamics can be arbitrary.

* 4.2. METHODS

4.2.1. Dynamic Mode Decomposition

Consider the following discrete linear dynamical system:

$$X' = AX \quad (4.1)$$

where $X \in \mathbb{R}^{voxels \times time-1}$ and $X' \in \mathbb{R}^{voxels \times time-1}$ are collection of snapshots of the system which are separated in time by Δt and $A \in \mathbb{R}^{voxels \times voxels}$ is the state transition matrix. In our case, these snapshots would simply be BOLD responses of fMRI voxels over time, A would be a connective field matrix and Δt would be the temporal resolution of the fMRI.

DMD tries to find a reduced order model \tilde{A} of the full transition matrix A that best approximates the data.

$$\tilde{A} = \tilde{U}^T A \tilde{U} = \tilde{U}^T X' \tilde{V} \tilde{\Sigma}^{-1} \quad (4.2)$$

where \tilde{U} , $\tilde{\Sigma}$ and \tilde{V}^T are obtained from truncated singular value decomposition of X . The size of reduced order model $\tilde{A} \in \mathbb{R}^{r \times r}$ depends on the truncation rank r which is determined by using *Gavish-Donoho* threshold ([Donoho and Gavish, 2013](#)). In any case it would be much smaller than the full A matrix since $r < time \ll voxels$. For more detailed explanation of DMD, please refer to section 3.2.1, Chapter 3.

4.2.2. Spatio-Temporal Dynamics

Spatio-temporal characteristics of a system are governed by its eigenvectors and eigenvalues. Since \tilde{A} is obtained from A through a similarity transform (\tilde{U} being a unitary matrix), its eigenvalues are preserved and can be obtained simply through an eigen decomposition ([Brunton and Kutz, 2022](#)):

$$\tilde{A}W = W\Lambda \quad (4.3)$$

where $\Lambda \in \mathbb{C}^{rank \times rank}$ is diagonal matrix containing the eigenvalues λ_r of A (same as eigenvalues of \tilde{A}). However the eigenvectors W of \tilde{A} are not exactly the same as that of A . It has been proven in [Tu et al. \(2014\)](#), that the exact eigenvectors of A can be computed as:

$$\Phi = X'V\Sigma^{-1}W \quad (4.4)$$

The eigenvectors $\Phi \in \mathbb{C}^{voxels \times rank}$ are known as DMD modes. Given a truncation

rank r , Λ contains top r complex frequencies of the system and Φ contains top r spatial modes of the system.

4.2.3. Data

The data used in this work has been previously acquired by [Senden et al. \(2019\)](#) for reconstructing mental imagery. We use 2 of the 6 subjects (S03 and S05) for our analysis. The data was collected using a 7-Tesla Siemens Magnetron scanner (Siemens; Erlangen, Germany). The actual task involved either perceiving or imagining four letters ‘H’, ‘T’, ‘S’ and ‘C’. Prior to the task, each participant practiced training sessions to control their imagery of visual letters. The task involved four imagery runs and one perceptual run as a control.

* 4.3. RESULTS

In order to validate the fidelity of our model in approximating the data, we report in [Table 4.1](#), the cross-validated Jaccard Similarities (JSs) and correlation coefficients between true and predicted BOLD responses. The similarity metrics are compared to a baseline null-model, where we compute cross-validated similarity metrics over randomly generated data with the same number of voxels as the BOLD data and time points equal to the mean of perception and imagery time points. It can be clearly seen that; indeed, our model is able to faithfully fit the data.

Similarity Metric	Subject	Mental Imagery				Perception	Baseline
Jaccard Similarity	S03	0.8138	0.8153	0.8070	0.8204	0.8176	0.3568
	S05	0.8311	0.8437	0.8298	0.8402	0.8306	0.4118
Correlation Coefficient	S03	0.9812	0.9872	0.98711	0.9921	0.9851	$\sim 10^{-4}$
	S05	0.9929	0.9924	0.9845	0.9986	0.9867	$\sim 10^{-4}$

Table 4.1.: Jaccard Similarities and correlation coefficients between true and predicted BOLD responses for subjects 03 and 05 over four mental imagery runs and one perception run compared to a baseline. The baseline was computed over randomly generated data

4.3.1. Connective Fields

Aggregated connective fields over two visual areas are depicted in [Figure 4.1](#), where each column is a *source region* and each row is a *target region*. It can be seen that across runs and subjects, the connective fields dominate higher visual areas. The presence of connective fields in V1 (as a source) is very weak.

In order to quantify the aggregated connective fields, we first compute correlation coefficients between them. It can be seen from Table 4.2, that the aggregated connective fields are highly correlated to each other for S03. Also, for S05, most runs are highly correlated to each other, except for the first run which is weakly correlated with perception and the third imagery run. Next, we investigate if there are any differences or similarities between total feedback and feedforward connectivities. Total feedback and feedforward connectivities are computed by taking the sum of upper and lower triangular parts of the aggregated connective field matrices. To that extent, referring to Table 4.3 we observe that these total feedback/feedforward connectivities are largely arbitrary.

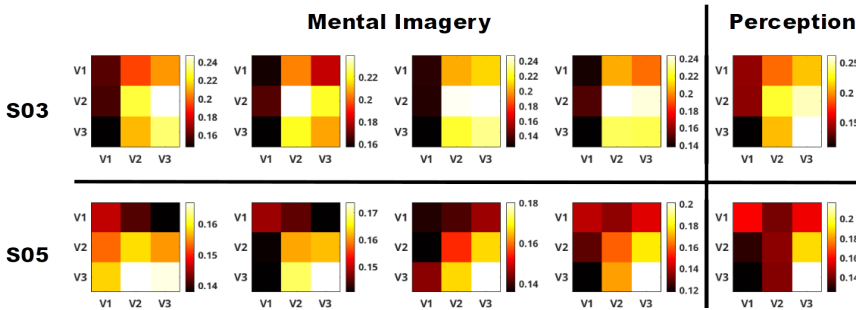


Figure 4.1.: Aggregated connective fields between three visual areas. The columns represent the *source* regions and the rows are the *target* regions.

4.3.2. Spatio-Temporal Dynamics

In order to depict temporal dynamics of the systems, we use the (complex) eigenvalues of reduced order connective field matrix \tilde{A} . In order to visualize these eigenvalues we take inspiration from Krake et al. (2021). For real-valued data, if a DMD eigenvalue is complex, then its complex conjugate is also a DMD eigenvalue (proved in Krake et al. (2021)). Therefore, we remove eigenvalues with a negative imaginary part to get rid of redundant temporal dynamics. Furthermore, in order to quantify the dominance of a mode, we scale it with its amplitude. The amplitude of a , as suggested, can be calculated as:

$$a = \Phi^\dagger x_2 \quad (4.5)$$

where $\Phi = [\nu_1, \nu_2, \dots, \nu_r]$ are the DMD modes, x_2 is the second time-point in the time series and \dagger denotes Moore-Penrose pseudoinverse. Note that, conventionally, in DMD literature, this amplitude is referred by the letter \mathbf{b} and is computed with the first timepoint in the time-series. But we refer to the amplitude as \mathbf{a} and following the recommendations made by Krake et al. (2021), we use the second time-point (instead

	I1	I2	I3	I4	P
I1	1	0.8812	0.9834	0.9806	0.9618
I2	0.8812	1	0.8355	0.9275	0.9702
I3	0.9835	0.8355	1	0.9585	0.9328
I4	0.9806	0.9275	0.9585	1	0.9884
P	0.9618	0.9702	0.9328	0.9884	1

(a)

	I1	I2	I3	I4	P
I1	1	0.7529	0.2485	0.7158	0.5469
I2	0.7529	1	0.6622	0.9232	0.9273
I3	0.2485	0.6622	1	0.7484	0.8628
I4	0.7158	0.9232	0.7484	1	0.9310
P	0.5469	0.9273	0.8628	0.9310	1

(b)

Table 4.2.: Correlation coefficients between aggregated connective fields between the runs for **a)** S03 and **b)** S05

		I1	I2	I3	I4	P
S03	Feedback	3.8541	3.2821	4.1296	4.2479	3.9839
	Feedforward	2.5367	2.5420	2.8631	2.7811	2.8130
S05	Feedback	2.6709	2.6413	2.7994	2.5128	3.0505
	Feedforward	4.1676	2.7038	1.8303	2.3761	2.5320

Table 4.3.: Total feedforward (lower triangle) and feedback (upper triangle) connectivity for each subject and run. Prior to computing the sum, the aggregated connective fields were normalized between $[0, 1]$

of the first). Also, in [Krake et al. \(2021\)](#), the second timepoint is denoted by x_1 because their indexing starts with 0.

Additionally, we compute the frequency corresponding a DMD eigenvalue λ_i as ([Brunton et al., 2016](#)):

$$f_i = \left| \frac{\Im(\log(\lambda_i)/\Delta t)}{2\pi} \right| \quad (4.6)$$

where $\Im()$ is the imaginary part of a complex number and Δt in our case is 3 seconds. This frequency (as compared to the one used in [Krake et al. \(2021\)](#)) is more interpretable, since it has the unit of *cycles/second* or *hertz*. In [Figure 4.2](#), as recommended by [Krake et al. \(2021\)](#), we depict the absolute values of complex eigenvalues ($|\lambda|$) over their corresponding frequencies. Furthermore, we modify the visualization recommen-

dation made in Krake et al. (2021), by scaling not only the opacity of an eigenvalue but also its particle size with its scaled mode amplitude $|a_i \nu_i|$. This means that larger and opaquer eigenvalues are more dominant than small and faded ones. The green particles correspond to all 4 mental imagery runs, while the magenta ones represent a single perception run.

As seen from the Figure 4.2, the eigenvalues for all the runs are arbitrary without any overlap, regardless of the subject or the visual task, except for the first eigenvalue. It should be noted that we do not plot the first eigenvalue corresponding to $1 + 0i$, which is a *zero frequency* component or the *static component*. Zero frequency corresponds to static spatio-temporal behaviour which shows a constant behaviour. All the runs have first eigenvalue corresponding to zero frequency. The scaled amplitudes of these eigenvalues are identically large and would completely overshadow the scaling of the size and opacity of the other particles, rendering them very hard to visualize.

	I1	I2	I3	I4	P
I1	1	0.1833	0.1934	0.2450	0.2110
I2	0.1833	1	0.1775	0.1998	0.1767
I3	0.1934	0.1775	1	0.2003	0.2154
I4	0.2450	0.1998	0.2003	1	0.1702
P	0.2110	0.1767	0.2154	0.1702	1

(a)

	I1	I2	I3	I4	P
I1	1	0.1733	0.1845	0.1829	0.2238
I2	0.1733	1	0.2229	0.1976	0.1986
I3	0.1845	0.2229	1	0.1792	0.2075
I4	0.1829	0.1976	0.1792	1	0.1718
P	0.2238	0.1986	0.2075	0.1718	1

(b)

Table 4.4.: Correlation coefficients between top DMD modes between the runs for a) S03 and b) S05

In order to investigate the extent to which DMD spatial modes overlap between mental imagery and perception, we compute the correlation coefficient between most scaled dominant DMD modes between the runs. Table 4.4 shows the correlation coefficients for a) S03 and b) S05. It can be seen from the table that these dominant spatial structures are arbitrary and do not correlate with the visual task. It is to be noted again that, we do not include the DMD mode corresponding to the zero frequency. These static DMD modes are identical across across runs, for individual subjects.

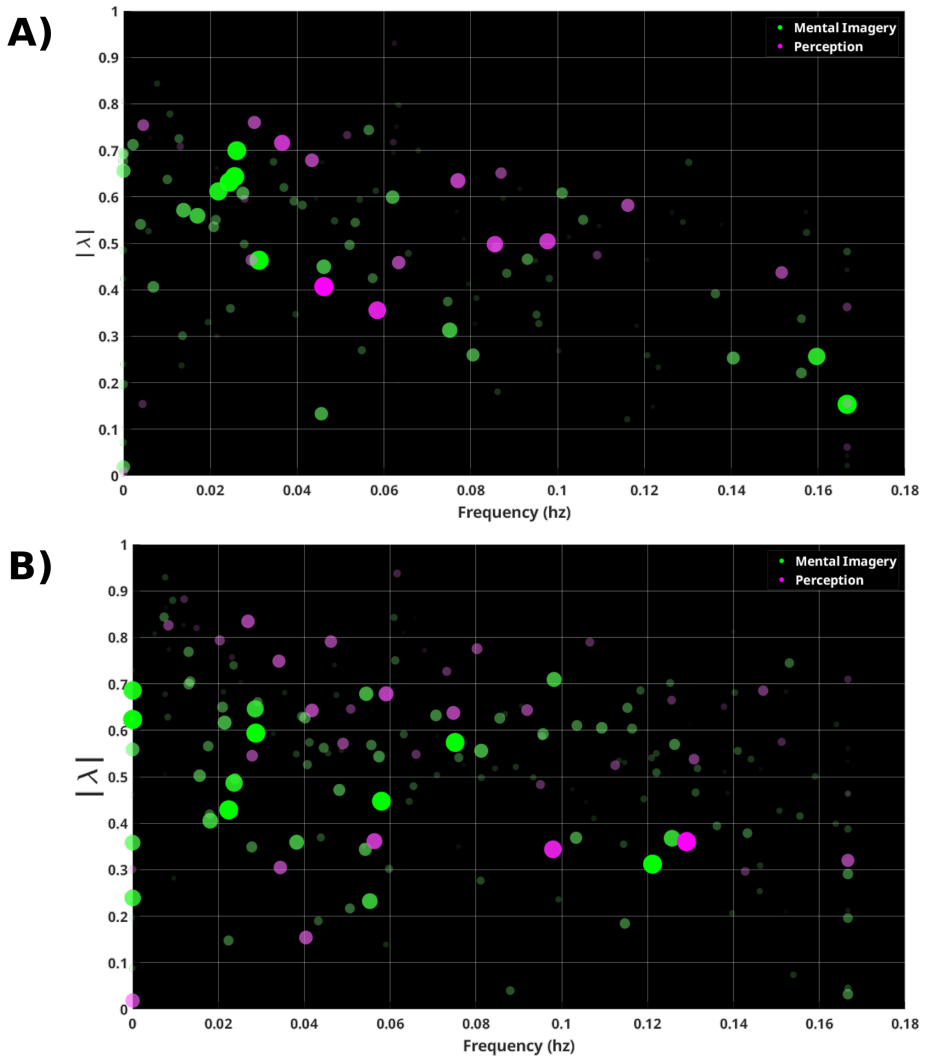


Figure 4.2.: The absolute value of eigenvalues $|\lambda|$ plotted against their corresponding frequencies for **A)** S03 and **B)** S05. The size and the opacity of the particles are scaled with the scaled mode amplitude $|a\nu|$. The mental imagery eigenvalues are in green and perceptual eigenvalues are in magenta.

✧ 4.4. DISCUSSION

In this preliminary work we investigate the extent to which neural mechanisms overlap between perception and mental imagery. We assess this overlap using Dynamic Mode Decomposition, in terms of connective fields and spatio-temporal dynamics. We perform our analysis on the data previously acquired by [Senden et al. \(2019\)](#). DMD is an

efficient tool that allows for estimation of quantities of interest with reasonable computational sources. Before our investigation, we ensure that the model approximates the data very well in terms of Jaccard Similarity and correlation coefficients.

In terms of connective fields, we observed that they are largely sourced at higher visual areas (V3/V2), which indicates a stronger top-down activity from higher visual areas to either primary visual cortex or laterally to other higher visual areas. It has been largely believed that perception can be explained by bottom-up activity, and mental imagery by top-down activity. However, a lot of research also shows that top-down activity is also important for perception (Buschman and Miller, 2007; Muckli, 2010; Muckli and Petro, 2013). More recently, it has been shown in Dijkstra et al. (2017b), that there is a strong increase in top-down coupling during both perception and mental imagery, which goes well with what we observed here via connective fields. However, a lack of bottom-up connective fields from V1, even in perception, needs to be addressed with further research.

Regarding the spatio-temporal characteristics, we did not observe any meaningful overlap between mental imagery and perception. With the help of the visualization technique suggested in Krake et al. (2021), we obtain and visualize scaled DMD eigenvalues against their corresponding frequencies. We observe that these temporal eigenvalues, both dominant and non-dominant, are arbitrary. Similarly, for spatial DMD modes, we did not observe any significant difference or similarity between runs, regardless of the visual task. The only spatio-temporal overlap that we observed was with DMD mode and eigenvalue associated with zero frequency.

Although these findings were the result of a preliminary investigation, further research is needed to validate our results. The data used in this study was used for reconstructing mental imagery (Senden et al., 2019) and not for comparing the neural mechanisms. Therefore, we recommend using a different task, which can be tailored more towards this analysis. In terms of temporal dynamics, fMRI suffers from temporal resolution. Therefore, to get a clearer picture of the temporal dynamics, one could use different recording techniques such as ElectroCochleoGraphy (ECoG), electroencephalogram (EEG), etc. In order to get a better understanding of the spatial dynamics, the analysis should also include segmented data from higher visual, and even non-visual brain regions.

5

GENERAL DISCUSSION

* 5.1. SYNOPSIS

This work primarily focuses on providing efficient methods that can save researchers their valuable time. In **Chapter 2**, we propose an extremely fast method for population receptive field (pRF) mapping. The vital catalyst to this method, is the hash-encoding of the stimulus (inspired from [Sutton and Barto \(2018\)](#)), which dramatically reduces the computational requirements. This facilitates mapping of millions of voxels within seconds. Researchers can conveniently use this method in two ways **a)** In an offline way: Where the pRFs and their subsequent parameters are readily available once the data is collected. Based on ridge regression, this method is ideal for post hoc analysis or for pRF related computation between two experiments. **b)** In an online way: This method, based on gradient-descent, can be used for real-time applications, where pRFs need to be mapped or extracted as the data is being collected. In **Chapter 3**, we attempt to address the unification problem ([Sejnowski, 2006](#)) (pRFs and Connective Fields) in an efficient way. Connective fields (CFs) are a natural extension to traditional pRFs. Inspired from fluid dynamics, we use (algebraic) Dynamic Mode Decomposition with control (aDMDc [Fonzi et al., 2020](#)), to simultaneously map pRFs and CFs. Continuing with the theme of this work, aDMDc, which is based on estimating reduced order models, combined with hash-encoding of the stimuli, is very efficient. Finally, in **Chapter 4**, we use DMD, to shed some light on the processes of mental imagery and perception. We observe very similar representation of connective fields, regardless of the task or the subject. However, we observe no overlap between the spatio-temporal mechanisms of mental imagery and perception, and also within mental imagery runs.

* 5.2. THE MOTIVE

In the fMRI era, population receptive field mapping has been dominating the field of visual neuroscience. pRFs give a topographical insight into how our vision is mapped onto the cortex. This mapping can be incredibly useful, not only in understanding our vision, but also for understanding the (full or partial) lack of vision. This knowledge can be then used in pathology and treatment of diseases and conditions that affect healthy vision. Given the size of fMRI based data, methods developed prior to this work ([Bhar et al., 2021](#)), are very slow and computationally exhaustive. Furthermore, pRF mapping lies at the heart of developing fMRI based Brain-Computer Interfaces (BCIs) for helping locked-in patients. Given the long computational time, standard methods are impractical for real-time BCIs. This straightforward motive of real-time pRF mapping led us to develop an extremely fast pRF mapping technique which can be used both offline (post hoc) and online (in real-time).

However, in visual neuroscience it is well known that stimulus alone may not be

enough to explain neuronal activity. One brain region can also elicit activity through a different brain region. A Connective Field extends the concept of a pRF to an intrinsic voxel-to-voxel mapping. Although, the methods for both pRF and CF mapping exist, they fail to account for their counterpart and are mapped separately. Unifying the idea of pRFs and CFs, has been a lingering problem in neuroscience (Sejnowski, 2006). This motivated us to use aDMDc (Fonzi et al., 2020) framework, to simultaneously map pRFs and CFs. The model we propose is a linear algebraic differential system, with CFs mapped through the differential term and pRFs through the algebraic term. Furthermore, we again hash-encode the stimuli using randomly generated Gaussians (Bhat et al., 2021). aDMDc in combination with hash-encoded stimuli, preserving the theme of this work, makes the whole mapping procedure computationally efficient. Additionally, DMD (and its flavours), are also able to obtain decoupled spatio-temporal characteristics of the system. These characteristics can be used to understand the underlying mechanism of a dynamical system. This motivated us to use DMD to compare the dynamics of mental imagery and perception.

* 5.3. METHODS AND THEIR VALIDATIONS

Extremely Fast pRF Mapping

The computational load of an algorithm is directly proportional to the amount of data that is being computed on. A pRF map is a huge matrix (pixels-by-voxels). The ultra-high spatial resolution comes at the cost of having to deal with large number of voxels in the first place. Researchers, normally, work around large number of voxels by masking out non-interesting voxels. However, even with masks, the number of voxels can contribute to a significant computational load. Instead of reducing the number of voxels, we reduce the number of pixels. This is done by encoding the overlap between the stimulus and randomly generated Gaussians, which then collapse into features (tile-coding and hashing; Sutton and Barto, 2018). The sparsity of the stimulus allows for encoding with a small number of features (much fewer than pixels). This significantly reduces the consumption of computational resources. Additionally, we also propose a fast parameter estimation method, that makes use of the location of the pRF (the pixel with highest value) and its mean pixel intensity, to predict its size. The pRF mapping and subsequent extraction of their parameters can be done in an online fashion as the data is being collected, using gradient-descent. For post-hoc estimation of pRFs and their parameters, we use ridge regression.

In terms of speed, our approach, without a doubt, is remarkably fast. We show that, on a regular workstation, it is possible to map millions of voxels within seconds. In a proof-of-concept study (Goebel et al., 2022), our approach was used to map pRFs in real-time, followed by their inversion for reconstructing imagined stimuli. In terms

of estimating the pRFs and their parameters, we validate our approach on both simulated data (with ground-truth) and empirical data. We get excellent correspondence between the estimated and the ground-truth quantities. On empirical data, we observe our model approximates the true BOLD data very well. Since we do not have ground truth pRFs, we compare our estimations with a standard grid-search approach (Dumoulin and Wandell, 2008; Senden et al., 2014). We again find excellent correspondence between the locations of the pRFs, but considerable discrepancy between their sizes. We also report that our approach poorly estimates the pRF sizes for the pRFs located at the edge of the visual field. This has been suggested to be a general drawback of linear models (Lage-Castellanos et al., 2020), which grid-search based methods do not suffer from.

Connective Field Modelling

A connective field map is a monstrous voxel-by-voxel map, when compared to pRF's voxel-by-pixel. On top of that, unifying pRFs and CFs makes it a much harder task. We use aDMDc framework, which estimates a reduced order model of CFs, which reduces the computational load. We, again, hash-encode the stimulus, which further reduces the computational load. The extent to which the CF model can be reduced depends on the truncation rank of the Singular Value Decomposition (SVD). Although data-driven methods like the Gavish-Donoho threshold (Donoho and Gavish, 2013) exist, we investigate the effect truncation rank in context of CFs, pRFs and different connectivity scenarios. We observed that the best estimating truncation rank is much higher than Gavish-Donoho threshold. However, if we impose the constraint of rank (to improve computational efficiency), we observed that the Gavish-Donoho threshold is indeed an optimal candidate.

We first validate our approach on simulated the where we observe excellent correspondence between predicted BOLD timecourse and ground-truth BOLD timecourse. We also observe good correspondence (compared to a baseline) between estimated and ground-truth CFs, pRFs and pRF parameters. On empirical data, we not only outperform the pRF-only model, but also observe an excellent approximation of BOLD timecourses (compared to a baseline).

We further, use DMD's ability to disentangle spatio-temporal properties of a dynamical system to compare the processes of mental imagery and perception. To that extent, we did find very similar CF representations between mental imagery and perception. However, the spatio-temporal dynamics were largely found to be arbitrary.

* 5.4. FUTURE CONSIDERATIONS AND RECOMMENDATIONS

No scientific method can be perfect. In principle, one method cannot be better than the other, it can only be advantageous in its context. Given the plethora of methods proposed, discussed and compared, the question arises: When to use which method ?

When it comes to pRF mapping, the fast method proposed here is a good general-purpose method. If online estimation of pRFs and their parameters is required, the gradient-descent based method should be used. Otherwise, the ridge regression method should be used, since it is a bit faster than gradient-descent. However, if the priority is reliably estimating the size of pRFs (especially towards the edge of the visual field), a grid-search based method is recommended. If the research design demands excellent approximation or prediction of the BOLD timecourses, aDMDC based method is better for estimation of pRFs. Finally, in case the pRFs need to be strictly Gaussians, grid-search methods should be used.

For connective field modelling, it is difficult to directly compare aDMDC based model and other proposed models (such as: [Heinze et al., 2011](#); [Haak et al., 2013](#); [Invernizzi et al., 2022](#)) for two reasons. 1) aDMDC based model forms a system of (algebraic) differential equations and other models assume a linear algebraic model, missing the time-delay component. 2) These non-differential models do not consider stimulus-driven pRFs in the mapping. If a computationally efficient and/or unified model is preferred, aDMDC based model is indeed better. In terms of approximating the BOLD signal, we recommend comparing different models on the same dataset and then making an informed decision about which model to use. For a fair comparison and to discard stimulus-driven activity, it is recommended that the data should be generated from a task that does not involve a stimulus. In case DMD or aDMDC based method is chosen, for general-purpose, we recommend using the Gavish-Donoho threshold ([Donoho and Gavish, 2013](#)), since it is optimal candidate. However, for specific cases, we recommend using Bayesian Optimization to determine the best threshold, for a specific function.

aDMDC is not limited to the visual cortex or fMRI. It can be conveniently used for other brain regions, different stimuli and different acquisition techniques such as Electroencephalogram (EEG), Magnetoencephalography (MEG), Electrocochography (ECoG) etc. It is also important to consider the spatial and temporal resolution of the data acquisition technique for extracting spatio-temporal dynamics using DMD based methods.

Lastly, it is important to consider the causalities with any mapping techniques. Fitting the data faithfully does not always ensure meaningful mapping. A model can fit the data excellently but might still have misleading mappings. Linear mapping methods, are often prone to spurious causalities. In the context of this work, there is always a possibility of having *ghost* pRFs and CFs. These spurious connections often occur

due to indirect causalities. Techniques for detecting indirect causality such as Partial Cross Mapping (Leng et al., 2020) do exist. However, these techniques are suitable for very small number of variables and scale very poorly with large number of variables (in our case, number of voxels and pixels). Scaling these causality-detecting methods remains an open research question that should be considered to improve the faithfulness of mapping.

§ BIBLIOGRAPHY

- Ahmadi, K., Herbig, A., Wagner, M., Kanowski, M., Thieme, H., Hoffmann, M.B., 2019. Population receptive field and connectivity properties of the early visual cortex in human albinism. *Neuroimage* 202, 116105.
- Albers, A.M., Kok, P., Toni, I., Dijkerman, H.C., De Lange, F.P., 2013. Shared representations for working memory and mental imagery in early visual cortex. *Current Biology* 23, 1427–1431.
- Albus, J.S., 1975. A new approach to manipulator control: The cerebellar model articulation controller (cmac).
- Albus, J.S., 1981. *Brains, behavior, and robotics*. Byte books Peterborough, NH.
- Allen, E.J., St-Yves, G., Wu, Y., Breedlove, J.L., Prince, J.S., Dowdle, L.T., Nau, M., Caron, B., Pestilli, F., Charest, I., et al., 2022. A massive 7t fmri dataset to bridge cognitive neuroscience and artificial intelligence. *Nature neuroscience* 25, 116–126.
- Altman, Y., 2020. *export_fig*. GitHub. URL: https://github.com/altmany/export_fig/releases/tag/v3.14. retrieved on December 18, 2020.
- Amano, K., Wandell, B.A., Dumoulin, S.O., 2009. Visual field maps, population receptive field sizes, and visual field coverage in the human mt+ complex. *Journal of neurophysiology* 102, 2704–2718.
- Anderson, E.J., Tibber, M.S., Schwarzkopf, D.S., Shergill, S.S., Fernandez-Egea, E., Rees, G., Dakin, S.C., 2017. Visual population receptive fields in people with schizophrenia have reduced inhibitory surrounds. *Journal of Neuroscience* 37, 1546–1556.
- Andersson, J.L.R., Skare, S., Ashburner, J., 2003. How to correct susceptibility distortions in spin-echo echo-planar images: application to diffusion tensor imaging. *Neuroimage* 20, 870–888. doi:10.1016/S1053-8119(03)00336-7.
- Baddeley, A.D., Andrade, J., 2000. Working memory and the vividness of imagery. *Journal of experimental psychology: general* 129, 126.

Bibliography

- Balasubramanian, M., Polimeni, J., Schwartz, E.L., 2002. The v1–v2–v3 complex: quasiconformal dipole maps in primate striate and extra-striate cortex. *Neural Networks* 15, 1157–1163.
- Bandettini, P.A., 2015. The birth of functional mri at the medical college of wisconsin, in: *fMRI: From Nuclear Spins to Brain Functions*. Springer, pp. 11–18.
- Barton, B., Brewer, A.A., 2015. fmri of the rod scotoma elucidates cortical rod pathways and implications for lesion measurements. *Proceedings of the National Academy of Sciences* 112, 5201–5206.
- Baseler, H.A., Gouws, A., Haak, K.V., Racey, C., Crossland, M.D., Tufail, A., Rubin, G.S., Cornelissen, F.W., Morland, A.B., 2011. Large-scale remapping of visual cortex is absent in adult humans with macular degeneration. *Nature neuroscience* 14, 649–655.
- Beck, N., Vincent, R.D., Lurie, J., Lewis, L.B., Rousseau, M.É., Evans, A.C., . Brain-browser .
- Bhat, S., Lührs, M., Goebel, R., Senden, M., 2021. Extremely fast prf mapping for real-time applications. *NeuroImage* 245, 118671.
- Binda, P., Thomas, J.M., Boynton, G.M., Fine, I., 2013. Minimizing biases in estimating the reorganization of human visual areas with bold retinotopic mapping. *Journal of vision* 13, 13–13.
- Brewer, A.A., Barton, B., 2014. Visual cortex in aging and alzheimer’s disease: changes in visual field maps and population receptive fields. *Frontiers in psychology* 5, 74.
- Brunton, B.W., Johnson, L.A., Ojemann, J.G., Kutz, J.N., 2016. Extracting spatial-temporal coherent patterns in large-scale neural recordings using dynamic mode decomposition. *Journal of neuroscience methods* 258, 1–15.
- Brunton, S.L., Kutz, J.N., 2022. *Data-driven science and engineering: Machine learning, dynamical systems, and control*. Cambridge University Press.
- Buschman, T.J., Miller, E.K., 2007. Top-down versus bottom-up control of attention in the prefrontal and posterior parietal cortices. *science* 315, 1860–1862.
- Dekker, T.M., Schwarzkopf, D.S., de Haas, B., Nardini, M., Sereno, M.I., 2019. Population receptive field tuning properties of visual cortex during childhood. *Developmental cognitive neuroscience* 37, 100614.
- DeYoe, E.A., Carman, G.J., Bandettini, P., Glickman, S., Wieser, J., Cox, R., Miller, D., Neitz, J., 1996. Mapping striate and extrastriate visual areas in human cerebral cortex. *Proceedings of the National Academy of Sciences* 93, 2382–2386.

Bibliography

- Dijkstra, N., Bosch, S.E., van Gerven, M.A., 2017a. Vividness of visual imagery depends on the neural overlap with perception in visual areas. *Journal of Neuroscience* 37, 1367–1373.
- Dijkstra, N., Bosch, S.E., van Gerven, M.A., 2019. Shared neural mechanisms of visual perception and imagery. *Trends in cognitive sciences* 23, 423–434.
- Dijkstra, N., Zeidman, P., Ondobaka, S., van Gerven, M.A., Friston, K., 2017b. Distinct top-down and bottom-up brain connectivity during visual perception and imagery. *Scientific reports* 7, 1–9.
- Donoho, D.L., Gavish, M., 2013. The optimal hard threshold for singular values is $4/\sqrt{3}$.
- Dougherty, R.F., Koch, V.M., Brewer, A.A., Fischer, B., Modersitzki, J., Wandell, B.A., 2003. Visual field representations and locations of visual areas v1/2/3 in human visual cortex. *Journal of vision* 3, 1–1.
- Dumoulin, S.O., Wandell, B.A., 2008. Population receptive field estimates in human visual cortex. *NeuroImage* 39, 647–60.
- Eckart, C., Young, G., 1936. The approximation of one matrix by another of lower rank. *Psychometrika* 1, 211–218.
- Engel, S.A., Glover, G.H., Wandell, B.A., 1997. Retinotopic organization in human visual cortex and the spatial precision of functional mri. *Cerebral cortex* (New York, NY: 1991) 7, 181–192.
- van Es, D.M., Theeuwes, J., Knapen, T., 2018. Spatial sampling in human visual cortex is modulated by both spatial and feature-based attention. *Elife* 7, e36928.
- Falcon, A., 2006. Aristotle on causality .
- Fishman, R.S., 1995a. Brain wars: Passion and conflict in the localization of vision in the brain, in: *History of Ophthalmology*. Springer, pp. 173–184.
- Fishman, R.S., 1995b. Ferrier’s mistake revisited, or when it comes to the brain, nothing is simple. *Archives of neurology* 52, 725–730.
- Flourens, P., 1846. Phrenology examined. Hogan & thompson.
- Folzenlogen, Z., Ormond, D.R., 2019. A brief history of cortical functional localization and its relevance to neurosurgery. *Neurosurgical focus* 47, E2.
- Fonzi, N., Brunton, S.L., Fasel, U., 2020. Data-driven nonlinear aeroelastic models of morphing wings for control. *Proceedings of the Royal Society A* 476, 20200079.

Bibliography

- Freeman, J., Simoncelli, E.P., 2011. Metamers of the ventral stream. *Nature neuroscience* 14, 1195.
- Georgy, L., Jans, B., Tamietto, M., Ptito, A., 2019. Functional reorganization of population receptive fields in a hemispherectomy patient with blindsight. *Neuropsychologia* 128, 198–203.
- Glickstein, M., 1985. Ferrier's mistake. *Trends in Neurosciences* 8, 341–344.
- Glickstein, M., 1988. The discovery of the visual cortex. *Scientific American* 259, 118–127.
- Glickstein, M., 2014. *Neuroscience: a historical introduction*. MIT Press.
- Glickstein, M., Rizzolatti, G., 1984. Francesco gennari and the structure of the cerebral cortex. *Trends in Neurosciences* 7, 464–467.
- Goebel, R., 2007. Localization of brain activity using functional magnetic resonance imaging, in: *Clinical functional MRI*. Springer, pp. 9–51.
- Goebel, R., Esposito, F., Formisano, E., 2006. Analysis of functional image analysis contest (fiac) data with brainvoyager qx: From single-subject to cortically aligned group general linear model analysis and self-organizing group independent component analysis. *Human brain mapping* 27, 392–401.
- Goebel, R., van Hoof, R., Bhat, S., Lühns, M., Senden, M., 2022. Reading imagined letter shapes from the mind's eye using real-time 7 tesla fmri, in: *2022 10th International Winter Conference on Brain-Computer Interface (BCI)*, IEEE. pp. 1–3.
- Gomez, J., Natu, V., Jeska, B., Barnett, M., Grill-Spector, K., 2018. Development differentially sculpts receptive fields across early and high-level human visual cortex. *Nature communications* 9, 1–12.
- Greene, C.A., Dumoulin, S.O., Harvey, B.M., Ress, D., 2014. Measurement of population receptive fields in human early visual cortex using back-projection tomography. *Journal of vision* 14, 17–17.
- Gross, C.G., 1999. *Brain, vision, memory: Tales in the history of neuroscience*. MIT Press.
- Haak, K.V., Cornelissen, F.W., Morland, A.B., 2012. Population receptive field dynamics in human visual cortex. *PLoS One* 7, e37686.
- Haak, K.V., Winawer, J., Harvey, B.M., Renken, R., Dumoulin, S.O., Wandell, B.A., Cornelissen, F.W., 2013. Connective field modeling. *Neuroimage* 66, 376–384.

Bibliography

- Hansen, P.C., 1987. The truncatedsvd as a method for regularization. *BIT Numerical Mathematics* 27, 534–553.
- Hanson, R.J., 1971. A numerical method for solving fredholm integral equations of the first kind using singular values. *SIAM Journal on Numerical Analysis* 8, 616–622.
- Hartline, H.K., 1938. The response of single optic nerve fibers of the vertebrate eye to illumination of the retina. *American Journal of Physiology-Legacy Content* 121, 400–415.
- Harvey, B.M., Dumoulin, S.O., 2011. The relationship between cortical magnification factor and population receptive field size in human visual cortex: constancies in cortical architecture. *Journal of Neuroscience* 31, 13604–13612.
- Heinzle, J., Kahnt, T., Haynes, J.D., 2011. Topographically specific functional connectivity between visual field maps in the human brain. *Neuroimage* 56, 1426–1436.
- Holmes, G., 1918. Disturbances of vision by cerebral lesions. *The British journal of ophthalmology* 2, 353.
- Hummer, A., Ritter, M., Woletz, M., Ledolter, A., Tik, M., Dumoulin, S.O., Holder, G., Schmidt-Erfurth, U., Windischberger, C., 2018. Artificial scotoma estimation based on population receptive field mapping. *Neuroimage* 169, 342–351.
- Inouye, T., 1909. Die Sehstörungen bei Schussverletzungen der kortikalen Sehsphäre: nach Beobachtungen an Verwundeten der letzten japanischen Kriege. Engelmann.
- Invernizzi, A., Gravel, N., Haak, K.V., Renken, R.J., Cornelissen, F.W., 2021. Assessing uncertainty and reliability of connective field estimations from resting state fmri activity at 3t. *Frontiers in neuroscience* 15, 625309.
- Invernizzi, A., Haak, K.V., Carvalho, J.C., Renken, R.J., Cornelissen, F.W., 2022. Bayesian connective field modeling using a markov chain monte carlo approach. *NeuroImage*, 119688.
- James, W., Burkhardt, F., Bowers, F., Skrupskelis, I.K., 1890. *The principles of psychology*. volume 1. Macmillan London.
- Jerison, H.J., 1977. Should phrenology be rediscovered? *Current Anthropology* 18, 744–746.
- Jokl, D.H.K., Hiyama, F., 2007. Tatsuji inouye-topographer of the visual cortex. exemplar of the germany-japan ophthalmic legacy of the meiji era. *Neuro-Ophthalmology* 31, 33–43.

Bibliography

- Jones, O.P., Alfaro-Almagro, F., Jbabdi, S., 2018. An empirical, 21st century evaluation of phrenology. *cortex* 106, 26–35.
- Kay, K.N., Weiner, K.S., Grill-Spector, K., 2015. Attention reduces spatial uncertainty in human ventral temporal cortex. *Current Biology* 25, 595–600.
- Kean, S., 2014. *The Tale of the Duelling neurosurgeons: The history of the human brain as revealed by true stories of trauma, madness, and recovery.* Random House.
- Keogh, R., Pearson, J., 2011. Mental imagery and visual working memory. *PloS one* 6, e29221.
- Klein, B.P., Harvey, B.M., Dumoulin, S.O., 2014. Attraction of position preference by spatial attention throughout human visual cortex. *Neuron* 84, 227–237.
- Krake, T., Reinhardt, S., Hlawatsch, M., Eberhardt, B., Weiskopf, D., 2021. Visualization and selection of dynamic mode decomposition components for unsteady flow. *Visual Informatics* 5, 15–27.
- Kriegeskorte, N., Goebel, R., 2001. An efficient algorithm for topologically correct segmentation of the cortical sheet in anatomical mr volumes. *NeuroImage* 14, 329–346.
- Kumano, H., Uka, T., 2010. The spatial profile of macaque mt neurons is consistent with gaussian sampling of logarithmically coordinated visual representation. *Journal of neurophysiology* 104, 61–75.
- Kwong, K.K., Belliveau, J.W., Chesler, D.A., Goldberg, I.E., Weisskoff, R.M., Poncelet, B.P., Kennedy, D.N., Hoppel, B.E., Cohen, M.S., Turner, R., 1992. Dynamic magnetic resonance imaging of human brain activity during primary sensory stimulation. *Proceedings of the National Academy of Sciences* 89, 5675–5679.
- Lage-Castellanos, A., Valente, G., Senden, M., De Martino, F., 2020. Investigating the reliability of population receptive field size estimates using fmri. *Frontiers in neuroscience* 14, 825.
- Lee, K., 1999. *The natural and the artefactual: The implications of deep science and deep technology for environmental philosophy.* Lexington Books.
- Lee, S., Papanikolaou, A., Logothetis, N.K., Smirnakis, S.M., Keliris, G.A., 2013. A new method for estimating population receptive field topography in visual cortex. *Neuroimage* 81, 144–157.
- Lee, S.H., Kravitz, D.J., Baker, C.I., 2012. Disentangling visual imagery and perception of real-world objects. *Neuroimage* 59, 4064–4073.

Bibliography

- Leng, S., Ma, H., Kurths, J., Lai, Y.C., Lin, W., Aihara, K., Chen, L., 2020. Partial cross mapping eliminates indirect causal influences. *Nature communications* 11, 1–9.
- Lerma-Usabiaga, G., Benson, N., Winawer, J., Wandell, B.A., 2020a. A validation framework for neuroimaging software: The case of population receptive fields. *PLoS computational biology* 16, e1007924.
- Lerma-Usabiaga, G., Winawer, J., Wandell, B.A., 2020b. Population receptive field shapes in early visual cortex are nearly circular. *bioRxiv* .
- Levenberg, K., 1944. A method for the solution of certain non-linear problems in least squares. *Quarterly of applied mathematics* 2, 164–168.
- Linhardt, D., Pawloff, M., Woletz, M., Hummer, A., Tik, M., Vasileiadi, M., Ritter, M., Lerma-Usabiaga, G., Schmidt-Erfurth, U., Windischberger, C., 2022. Intra- and intersession reproducibility of artificial scotoma prf mapping results at ultra-high fields. *Eneuro* .
- Marques, J.P., Kober, T., Krueger, G., van der Zwaag, W., Van de Moortele, P.F., Grueter, R., 2010. Mp2rage, a self bias-field corrected sequence for improved segmentation and t1-mapping at high field. *Neuroimage* 49, 1271–1281.
- Merkel, C., Hopf, J.M., Schoenfeld, M.A., 2018. Spatial elongation of population receptive field profiles revealed by model-free fmri back-projection. *Human brain mapping* 39, 2472–2481.
- Merkel, C., Hopf, J.M., Schoenfeld, M.A., 2020. Modulating the global orientation bias of the visual system changes population receptive field elongations. *Human brain mapping* 41, 1765–1774.
- Mineault, P., 2021. Auto gaussian and gabor fits. <https://nl.mathworks.com/matlabcentral/fileexchange/31485-auto-gaussian-gabor-fits>. Retrieved on September 8, 2021.
- Motter, B.C., 2009. Central v4 receptive fields are scaled by the v1 cortical magnification and correspond to a constant-sized sampling of the v1 surface. *Journal of Neuroscience* 29, 5749–5757.
- Muckli, L., 2010. What are we missing here? brain imaging evidence for higher cognitive functions in primary visual cortex v1. *International Journal of Imaging Systems and Technology* 20, 131–139.
- Muckli, L., Petro, L.S., 2013. Network interactions: Non-geniculate input to v1. *Current opinion in neurobiology* 23, 195–201.

Bibliography

- Munk, H., 1890. Of the visual area of the cerebral cortex, and its relation to eye movements. *Brain* 13, 45–70.
- Ogawa, S., Tank, D.W., Menon, R., Ellermann, J.M., Kim, S.G., Merkle, H., Ugurbil, K., 1992. Intrinsic signal changes accompanying sensory stimulation: functional brain mapping with magnetic resonance imaging. *Proceedings of the National Academy of Sciences* 89, 5951–5955.
- Papanikolaou, A., Keliris, G.A., Lee, S., Logothetis, N.K., Smirnakis, S.M., 2015. Non-linear population receptive field changes in human area v5/mt+ of healthy subjects with simulated visual field scotomas. *NeuroImage* 120, 176–190.
- Pearson, J., 2019. The human imagination: the cognitive neuroscience of visual mental imagery. *Nature reviews neuroscience* 20, 624–634.
- Peters, J.C., Reithler, J., Goebel, R., 2012. Modeling invariant object processing based on tight integration of simulated and empirical data in a common brain space. *Frontiers in computational neuroscience* 6, 12.
- Polimeni, J.R., Hinds, O.P., Balasubramanian, M., van der Kouwe, A., Wald, L.L., Dale, A.M., Fischl, B., Schwartz, E.L., et al., 2005. The human v1–v2–v3 visuotopic map complex measured via fmri at 3 and 7 tesla, in: *Society for Neuroscience Abstracts*.
- Proctor, J.L., Brunton, S.L., Kutz, J.N., 2016. Dynamic mode decomposition with control. *SIAM Journal on Applied Dynamical Systems* 15, 142–161.
- Reddy, L., Tsuchiya, N., Serre, T., 2010. Reading the mind’s eye: decoding category information during mental imagery. *Neuroimage* 50, 818–825.
- Roberts, D.R., Bahn, V., Ciuti, S., Boyce, M.S., Elith, J., Guillerá-Arroita, G., Hauenstein, S., Lahoz-Monfort, J.J., Schröder, B., Thuiller, W., Warton, D.I., Wintle, B.A., Hartig, F., Dormann, C.F., 2017. Cross-validation strategies for data with temporal, spatial, hierarchical, or phylogenetic structure. *Ecography* 40, 913–929. doi:[10.1111/ecog.02881](https://doi.org/10.1111/ecog.02881).
- Sack, A.T., Cohen Kadosh, R., Schuhmann, T., Moerel, M., Walsh, V., Goebel, R., 2009. Optimizing functional accuracy of tms in cognitive studies: a comparison of methods. *Journal of cognitive neuroscience* 21, 207–221.
- Schmid, P.J., 2010. Dynamic mode decomposition of numerical and experimental data. *Journal of fluid mechanics* 656, 5–28.
- Schwartz, E.L., 1980. Computational anatomy and functional architecture of striate cortex: a spatial mapping approach to perceptual coding. *Vision research* 20, 645–669.

Bibliography

- Sejnowski, T.J., 2006. What are the projective fields of cortical neurons? van Hemmen, JL, Sejnowski, TJ (Eds.) 23, 394–405.
- Senden, M., Emmerling, T.C., Van Hoof, R., Frost, M.A., Goebel, R., 2019. Reconstructing imagined letters from early visual cortex reveals tight topographic correspondence between visual mental imagery and perception. *Brain Structure and Function*, 1–17.
- Senden, M., Reithler, J., Gijsen, S., Goebel, R., 2014. Evaluating population receptive field estimation frameworks in terms of robustness and reproducibility. *PLoS ONE* 9, e114054. doi:[10.1371/journal.pone.0114054](https://doi.org/10.1371/journal.pone.0114054).
- Sereno, M.I., Dale, A., Reppas, J., Kwong, K., Belliveau, J., Brady, T., Rosen, B., Tootell, R., 1995. Borders of multiple visual areas in humans revealed by functional magnetic resonance imaging. *Science* 268, 889–893.
- Sherrington, C.S., 1910. Flexion-reflex of the limb, crossed extension-reflex, and reflex stepping and standing. *The Journal of physiology* 40, 28.
- Shmuel, A., Yacoub, E., Chaimow, D., Logothetis, N.K., Ugurbil, K., 2007. Spatio-temporal point-spread function of fmri signal in human gray matter at 7 tesla. *Neuroimage* 35, 539–552.
- Silson, E.H., Reynolds, R.C., Kravitz, D.J., Baker, C.I., 2018. Differential sampling of visual space in ventral and dorsal early visual cortex. *Journal of Neuroscience* 38, 2294–2303.
- Silva, M.F., Brascamp, J.W., Ferreira, S., Castelo-Branco, M., Dumoulin, S.O., Harvey, B.M., 2018. Radial asymmetries in population receptive field size and cortical magnification factor in early visual cortex. *NeuroImage* 167, 41–52.
- Simpson, D., 2005. Phrenology and the neurosciences: contributions of fj gall and jg spurzheim. *ANZ journal of surgery* 75, 475–482.
- Stokes, M., Thompson, R., Cusack, R., Duncan, J., 2009. Top-down activation of shape-specific population codes in visual cortex during mental imagery. *Journal of Neuroscience* 29, 1565–1572.
- Sutton, R.S., Barto, A.G., 2018. Reinforcement learning: An introduction. MIT press.
- Thielen, J., Guclu, U., Gucluturk, Y., Ambrogioni, L., Bosch, S.E., van Gerven, M., 2019. Deepprf: Ultrafast population receptive field mapping with deep learning. *bioRxiv*, 732990.

Bibliography

- Thirion, B., Duchesnay, E., Hubbard, E., Dubois, J., Poline, J.B., LeBihan, D., Dehaene, S., 2006. Inverse retinotopy: inferring the visual content of images from brain activation patterns. *Neuroimage* 33, 1104–1116.
- Tong, F., 2013. Imagery and visual working memory: one and the same? *Trends in cognitive sciences* 17, 489–490.
- Tu, J.H., Rowley, C.W., Luchtenburg, D.M., Brunton, S.L., Kutz, J.N., 2014. On dynamic mode decomposition: Theory and applications. *Journal of Computational Dynamics* 1, 391–421.
- Tubbs, R.S., Kakati, D., Chern, J.J., Loukas, M., Shoja, M., Mortazavi, M.M., Cohen-Gadol, A.A., 2012. Tatsuji inouye: the mind’s eye. *Child’s Nervous System* 28, 147–150.
- Uludag, K., Ugurbil, K., Berliner, L., 2015. *fMRI: from nuclear spins to brain functions*. volume 30. Springer.
- Van Hemmen, J.L., Sejnowski, T.J., 2005. *23 problems in systems neuroscience*. Oxford University Press.
- Varah, James, M., 1973. On the numerical solution of ill-conditioned linear systems with applications to ill-posed problems. *SIAM Journal on Numerical Analysis* 10, 257–267.
- Victor, J.D., Purpura, K., Katz, E., Mao, B., 1994. Population encoding of spatial frequency, orientation, and color in macaque v1. *Journal of neurophysiology* 72, 2151–2166.
- Vo, V.A., Sprague, T.C., Serences, J.T., 2017. Spatial tuning shifts increase the discriminability and fidelity of population codes in visual cortex. *Journal of Neuroscience* 37, 3386–3401.
- Wandell, B.A., Winawer, J., 2011. Imaging retinotopic maps in the human brain. *Vision research* 51, 718–737.
- Webb, E.K., Etter, J.A., Kwasa, J.A., 2022. Addressing racial and phenotypic bias in human neuroscience methods. *Nature Neuroscience* 25, 410–414.
- Welford, B., 1962. Note on a method for calculating corrected sums of squares and products. *Technometrics* 4, 419–420.
- Wickens, A.P., 2014. *A history of the brain: from stone age surgery to modern neuroscience*. Psychology Press.

Bibliography

- Zimmermann, J., 2014. The how, not where in functional magnetic resonance imaging. Ph.D. thesis. Maastricht University.
- Zola-Morgan, S., 1995. Localization of brain function: The legacy of franz joseph gall (1758-1828). *Annual review of neuroscience* 18, 359–383.

§ APPENDIX TO CHAPTER 2

* A.1. Hyperparameter sharing between gradient descent and ridge regression

Here we show that, under reasonable assumptions, the learning rate for gradient descent and the regularization parameter in ridge regression are inversely related. In a real-time setting, each iteration of online gradient descent corresponds to observing a single data point (time volume). Alternatively, one might consider performing an offline gradient descent with a single iteration where a single batch contains the entire dataset. That is, referring to equation 2.8, $n = 1$ and $n - 1 = 0$. If we assume that we initialize $\theta_0 \leftarrow 0$, where θ_0 is the optimal solution, then we get:

$$\theta = \eta \phi^T B \tag{A.1}$$

And from equation 2.5, we have:

$$\theta = (\phi^T \phi + \lambda I)^{-1} \phi^T B \tag{A.2}$$

For the case that $\lambda = \frac{1}{\eta}$ and that λ is sufficiently large such that $\Phi^T \Phi + \lambda I \approx \lambda I$,

$$\eta \Phi^T B \approx (\Phi^T \Phi + \lambda I)^{-1} \Phi^T B \tag{A.3}$$

Thus, if we use $\lambda = \frac{1}{\eta}$ with a sufficiently large λ , ridge regression and online gradient descent yield similar results.

* A.2. Effect of hyperparameters on mapping procedure

The set of hyperparameters involved in the mapping procedure are learning rate (or regularization parameter), FWHM of hashed Gaussians and shrinkage. Note that we do not address learning rate and regularization parameter separately since we assume them to be the inverse of each other (refer to A.1). For all the experiments reported in this paper, we use the same set of hyperparameters (except for projecting cortical activity back into the visual field, which benefits from slightly higher shrinkage).

In order to understand how the choice of hyperparameters can affect receptive field mapping, we fine-tune them by minimizing an objective function using Bayesian Optimization. Bayesian Optimization enables us to visualize the model mean (estimated objective function surface). For the objective (or loss) function we use Jaccard Distance which can be defined as:

$$f_{JD}(X, Y) = 1 - \frac{\sum_i \min(x_i, y_i)}{\sum_i \max(x_i, y_i)} \quad (\text{A.4})$$

In figure A.1, we present objective function models of two cases: A.1a where we keep shrinkage constant and A.1b where keep learning rate constant. It can be seen from figure A.1a that the mapping procedure is not very sensitive to learning rate. However, for the relation proved in A.3 to hold true, we recommend using a small value of learning rate (< 1). Shrinkage does not have any effect on mapping itself, since it is used after the mapping procedure to remove abnormal pixels surrounding the receptive fields. Using a large value of shrinkage will reduce the size of the receptive field. FWHM, however, has a direct effect on the mapping procedure. Figure A.2 shows how a combination of FWHM and shrinkage affect the shape of the mapped receptive fields. Using a large FWHM would result in a large overlap between the stimulus and hashed Gaussians, thereby over-encoding the presence of the stimulus. As a result, the mapping procedure would overestimate the size of the receptive fields. This effect is clear from figure A.2, where we visually compare the receptive fields (for the same voxel) obtained using different values of FWHM. The shrinkage and FWHM have an opposite effect on the receptive fields. Hence it is important to use a balanced choice of FWHM and shrinkage in order to obtain optimal receptive fields.

* A.3. Supplementary Figures and Tables

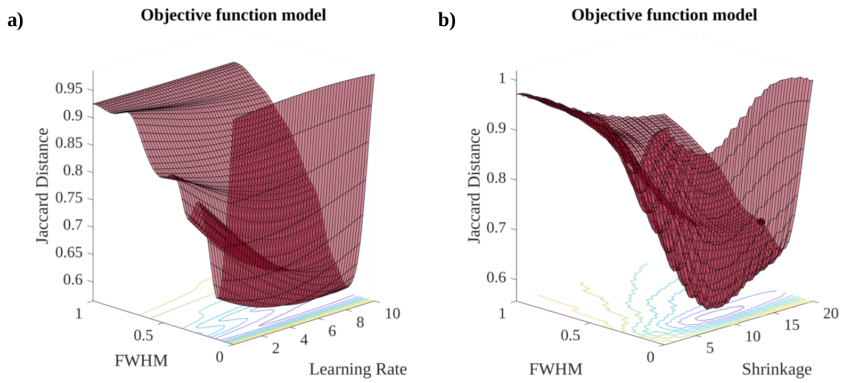


Figure A.1.: Estimated objective function model for **a)** the learning rate and the FWHM (the shrinkage was set to 6 **b)** the shrinkage and FWHM (the learning rate was set to $\eta = 0.1$). The hyperparameters were optimized for Jaccard Distance between mapped receptive fields and ground-truth receptive fields based on 3T-like simulated data. The optimization was performed using Bayesian Optimization. The optimization was stopped after 40 evaluations.

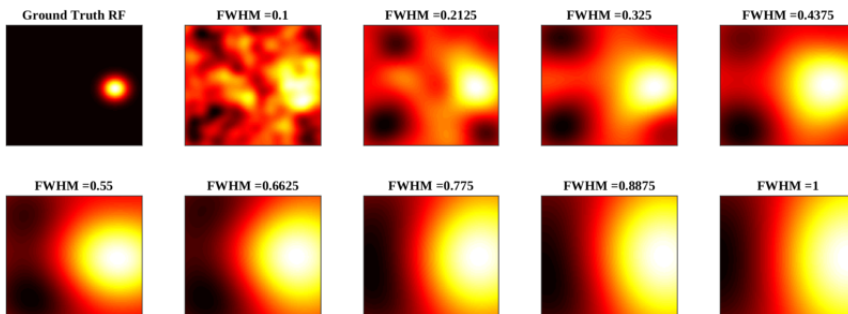


Figure A.2.: The effect of FWHM of hashed Gaussians on mapped receptive fields. The receptive field on the top left is the ground-truth receptive field based on 3T-like simulated data. The rest of the receptive fields were mapped using different FWHMs in the range $[0, 1]$. The learning rate was kept constant to 0.1 and shrinkage was not used. Note that, we use FWHM relative to resolution of stimulus space and hence it is restricted to the range $[0, 1]$.

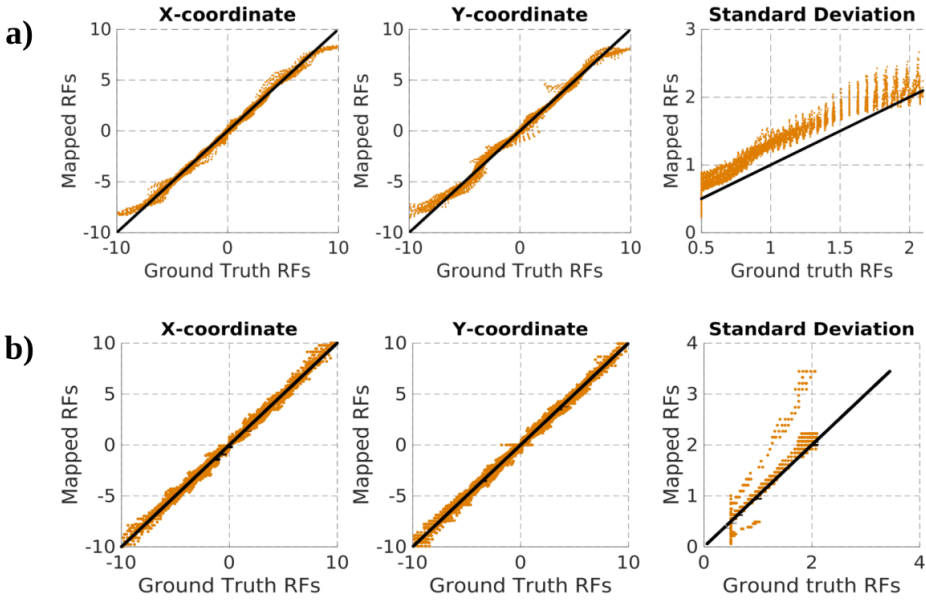


Figure A.3.: Estimated vs ground-truth pRF parameters for **a)** f -pRF_{ridge} and **b)** GS-pRF. A line with a slope of 1 is included as a reference. The voxels lying beyond the radius of measured visual field (maximum eccentricity) were ignored for estimating pRF parameters.

	f -pRF _{ridge}	GS-pRF
S01	0.4515 (95 % CI [0.4489,0.4540])	0.4313 (95 % CI [0.4283,0.4343])
S02	0.4551 (95 % CI [0.4526,0.4576])	0.4282 (95 % CI [0.4254,0.4310])
S03	0.4557 (95 % CI [0.4524,0.4589])	0.4299 (95 % CI [0.4261,0.4337])

(a)

	f -pRF _{ridge}	GS-pRF
S01	0.4540 (95 % CI [0.4531,0.4548])	0.3828 (95 % CI [0.3818,0.3837])
S02	0.4410 (95 % CI [0.4401,0.4420])	0.3546 (95 % CI [0.3535,0.3557])
S03	0.6282 (95 % CI [0.6269,0.6295])	0.6023 (95 % CI [0.6008,0.6038])
S04	0.4458 (95 % CI [0.4446,0.4470])	0.3716 (95 % CI [0.3702,0.3729])
S05	0.5421 (95 % CI [0.5405,0.5437])	0.4913 (95 % CI [0.4895,0.4932])
S06	0.5404 (95 % CI [0.5390,0.5418])	0.4746 (95 % CI [0.4731,0.4761])

(b)

Table A.1.: Mean correlation coefficients between predicted and acquired BOLD signal obtained from **a)** 3T and **b)** 7T empirical data using top 1% voxels obtained from GS-pRF.

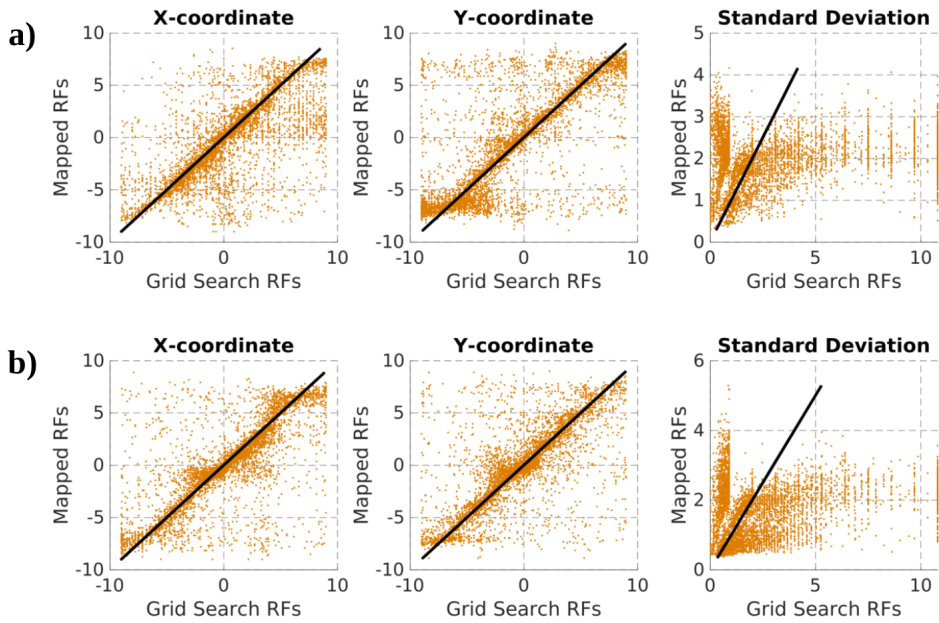


Figure A.4.: Scatter plots between the pRF parameters (location and size) estimated using f -pRF_{ridge} and the grid search method on 3 Tesla empirical data. The subfigures **a** and **b** correspond to subjects 02 and subject 03 respectively.

		Subject	Overlap
		S01	44.12 %
		S02	52.19 %
		S03	80.49 %
		S04	57.23 %
		S05	80.45 %
		S06	81.06 %
		(a)	(b)

Table A.2.: Percentage overlap between top 1% voxels obtained from GS-pRF and f -pRF_{ridge} from **a**) 3T and **b**) 7T empirical data

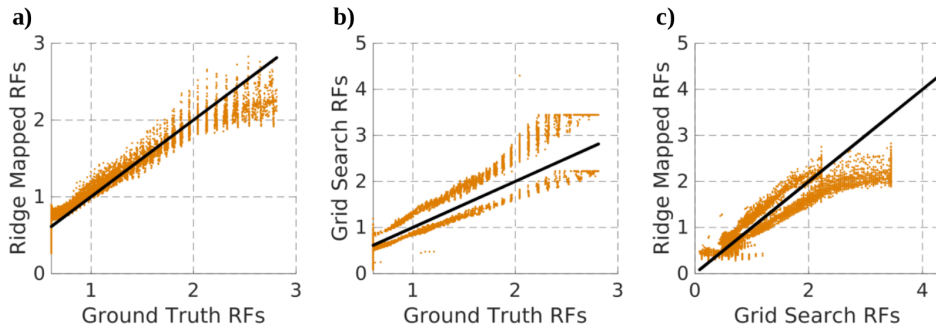


Figure A.5.: Comparison of receptive field size estimates and ground truth for 7T empirical data. **a)** Sizes estimated using our fast procedure vs ground truth sizes. **b)** Sizes estimated using grid-search vs ground truth sizes. **c)** Sizes estimated using our fast procedure vs grid-search estimates.

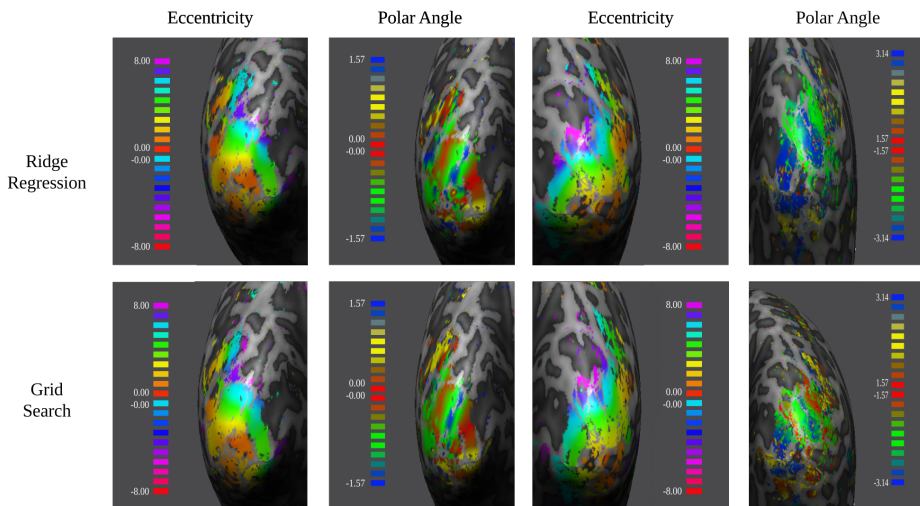


Figure A.6.: Eccentricity and polar angle maps in both hemispheres of S05 in the 7T dataset. The upper row shows maps obtained using our fast parameter estimation procedure whereas the bottom row shows maps obtained using the GS-pRF procedure.

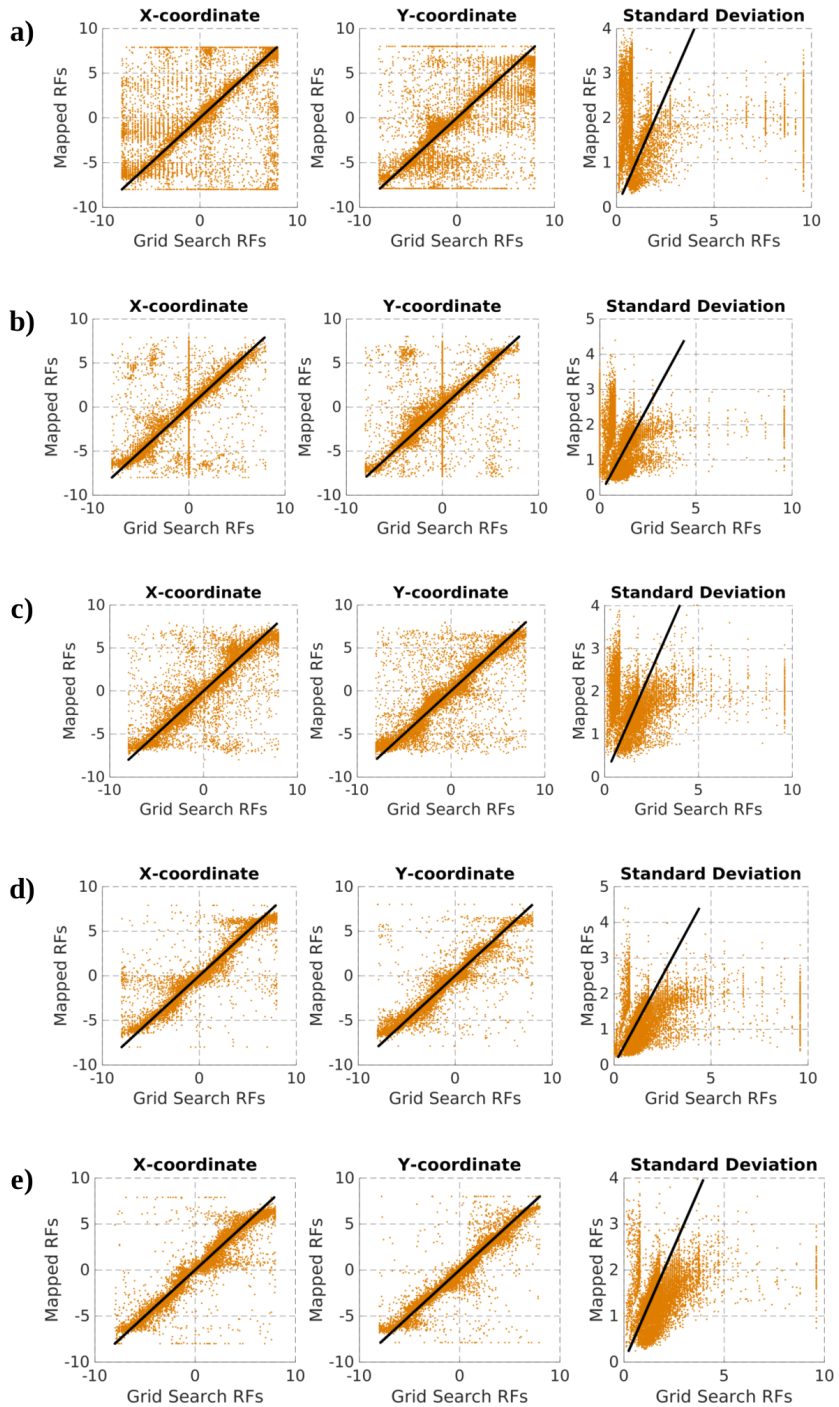


Figure A.7.: Scatter plots between the pRF parameters (location and size) estimated using f -pRF_{ridge} and the grid search method on 3 Tesla empirical data. The subfigures **a**, **b**, **c**, **d**, **e** correspond to subjects 01, 02, 04, 05 and 06 respectively.

✿ IMPACT

functional Magnetic Resonance Imaging (fMRI) has revolutionized the way researchers examine the brain. However, the high (or ultra high) resolution of fMRI comes at a cost of a colossal amount of data. Even though computers are getting more powerful and accessible, analyzing fMRI data can still be computationally heavy and time consuming. The main objective of this work was to provide an arsenal of computational methods, which individually or together can reduce the computational burden. Although these methods were specifically developed to model population receptive fields (pRFs) and connective fields (CFs); they can be conveniently extended to other domains.

In **Chapter 2**, we demonstrate that it is now possible to faithfully map pRFs of millions of voxels in the order of seconds. This can indeed save researchers a lot of their precious time. Such a fast mapping was made possible by hash-encoding (Sutton and Barto, 2018) the stimulus space, which tremendously reduces memory requirements. Linear models are widely used for their simplicity and interpretability. The linear models with a large and relatively sparse predictor space, can benefit from hash-encoding to accelerate the linear mapping. A drastic reduction in memory requirements has an added benefit of mapping the pRFs in an online fashion (real-time pRF mapping). This can largely impact development of brain-computer interfaces (BCIs) for helping *locked-in* patients. In a recent proof-of-concept work by Goebel et al. (2022), it was demonstrated that such an online pRF mapping can be used to reconstruct imaged letters in real-time. This can pave a way for developing a letter speller BCI which can, in real-time, reconstruct imagined letters and display them back to the participants, in MRI scanners, as feedback.

In **Chapter 3**, we propose a novel method for modelling CFs, which are a natural extension to the pRFs. In this chapter, we not only tackle the computational inefficiency of CF modelling, but also propose a unified CF and pRF model. To achieve this, we combine algebraic Dynamic Mode Decomposition (aDMDc; Fonzi et al., 2020), which stems from the field of fluid dynamics, with the hash-encoding of the stimulus space (Bhat et al., 2021). This goes to show that these methods are very generalized and can be used to tackle a variety of different problems ranging from fluid mechanics to computational neuroimaging. We further, in **Chapter 4**, use DMD to investigate

the similarities and differences between mental imagery and perception tasks. In this preliminary work we observed spatio-temporal characteristics of mental imagery and perception, to be largely arbitrary. However, we observed very similar aggregated CFs between the two tasks and subjects. The DMD-based methods can indeed enrich how we study not just vision, but also the brain as a dynamical system.

* ACKNOWLEDGEMENTS

Writing is my least favourite form of communication, especially when it is non-scientific. I find it incredibly challenging to express my gratitude by writing words that make sense. I partially attribute this to my frustration with myself for not being able to effectively express my appreciation. But I shall not back down when an opportunity like this presents itself.

Rainer and **Mario** ... you two are true gentlemen. You held open the door to neuroscience for me and made my journey so smooth and amazing. **Rainer**, it was an absolute pleasure and a privilege having you as my supervisor. Your optimistic attitude is contagious. Remarkably, you always found a way to make things work out in the end. And I truly hope that, one way or the other, we will continue to work together in the future. **Mario**, doing science with you, I always felt like a kid on the playground who just doesn't wanna go home. You have always been my safety net. And I wish that one day (no idea how), we will find like six months or so where we don't do any research but simply read, watch, learn and have close encounters with the fourth paradigm.

Christl, Eva, Riny, José and Andra... you are the backbone of CN department. I have no idea how you are able to manage everything so well. You have been extremely helpful, not just to me but to the entire department. Thank you.

All the **CCN members**, I cherish our meetings and recreations. Thank you for contributing to and creating such a productive, creative and a lovely working environment.

Manas and **Raphael**, thank you for being my paranymphs. **Raphael**, I really appreciate how supportive and cheerful you are. May you keep your enthusiasm forever. **Manas**, it is incredible how long we know each other with you being my first friend. Cheers to so many good times, and many more to come. And , yes we should be meeting more often.

Shout out to my hydro-homie **Olek** for taking time and designing the beautiful cover page.

Duță family , you always made me feel so welcomed and made me one of your own. I have always enjoyed our time together and I am always excited to meet you whenever it is possible. I am thankful for all the wonderful memories we've shared together, and I look forward to creating many more in the future.

ACKNOWLEDGEMENTS

To my parents and grandparents ... without your support it would have been impossible for me to be where I am today. I am forever grateful to you.

Cătălina, my life without you is unimaginable. I cannot express in words how wonderful you have made my life. But, I don't need words for that, because you already know how much you mean to me.

✿ CURRICULUM VITAE

Salil was born in Nagpur, India on December 8th, 1993. In 2015, he obtained his Bachelor's degree in Electrical Engineering. During this time, he worked with artificial neural networks, which led him to pursue a Master of Science in Artificial Intelligence from Maastricht University. Under the supervision of Dr. Kurt Driessens and Prof. Dr. Rainer Goebel, he analyzed deep convolutional neural networks in the frequency domain, which resulted in his Master's thesis. In 2017, he began his PhD trajectory under the supervision of Prof. Dr. Rainer Goebel and Dr. Mario Senden in the Department of Cognitive Neuroscience. During his PhD, he worked on developing and applying efficient computational methods for mapping population receptive fields and connective fields. He currently works at the same department as a post-doctoral researcher.

